

Motion Control of High-Speed Hydrofoil Vessels Using State-Space Methods

By

Iason Chatzakis

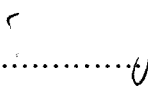
Diploma in Naval Architecture and Marine Engineering
National Technical University of Athens

Submitted to the Department of Ocean Engineering
in Partial Fulfillment of the Requirements for the Degree of

Master of Science in Ocean Engineering
at the
Massachusetts Institute of Technology
June 2004

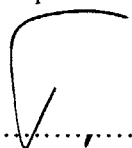
© 2004 Massachusetts Institute of Technology
All rights reserved

The author hereby grants MIT permission to reproduce and to distribute publicly paper or electronic copies of this thesis document in whole or in part.


Author:.....

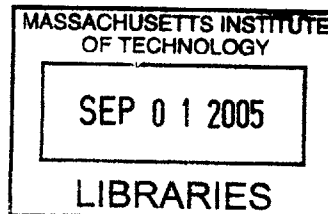
Department of Ocean Engineering
May 7, 2004

Certified
by:.....


Paul D. Slavounos
Professor of Naval Architecture
Thesis Advisor

Accepted
by:.....


Michael Triantafyllou
Professor of Ocean Engineering
Chairman, Departmental Committee on Graduate Studies



ARCHIVES

To the memory of my father

Motion Control of High-Speed Hydrofoil Vessels Using State-Space Methods

By

Iason Chatzakis

Submitted to the Department of Ocean Engineering on May 7, 2004
in partial fulfillment of the requirements for the degree of
Master of Science in Ocean Engineering

Abstract

Hydrofoil ships cruise at large speeds and are often expected to operate in rough weather conditions. The motion of these ships due to their encounter with ambient waves can become uncomfortable or even dangerous without the use of some form of motion control. The objective of this thesis is to study the active motion control of high-speed hydrofoil vessels.

This work is composed of two parts, reflecting the two disciplines applied: hydrodynamics and optimal control theory. In the first part, a two-dimensional computer code is developed for the calculation of forces and the integration of the equations of motion for fully submerged lifting bodies operating near a free surface. A Rankine source boundary element (panel) method is used assuming potential flow around the body. As a result, the motions of a hydrofoil vessel operating at high speed in ambient waves can be estimated in the time domain.

In the second part, the application of optimal control theory to motion control of hydrofoil ships is investigated. The code developed in the first part of this work is used as a simulation tool for the assessment of control laws designed using state-space linear-quadratic methods. It is found that a linear-quadratic optimal controller can attenuate the motion response of the vessel advancing in monochromatic or ocean waves, with proper adjustment of the cost matrices that enter the quadratic performance criterion used.

Accurate dynamic modeling is crucial in the design of control laws for any system. Vessels that operate on or near the free surface experience hydrodynamic memory effects due to their own motion. Casting the seakeeping equations of motion into a linear, time-invariant state-space model suitable for the design of optimal control laws is challenging since there is no straightforward way of including these memory effects in the model. In this work, the seakeeping equations of motion are cast in a linear state-space form which does not include memory effects, and the motion control simulation results show that this model is satisfactory for the design of hydrofoil vessel control laws.

Thesis Supervisor: Paul D. Sclavounos
Title: Professor of Naval Architecture

Acknowledgements

I owe many thanks to my advisor, Professor Paul Sclavounos, who provided constant guidance, inspiration and support during the course of this work. Working next to him for the past two years has been an invaluable learning experience.

My parents have been with me constantly, albeit from a great distance. I would not have been able to accomplish much without their support.

I am grateful for the creative interaction with my fellow students from the Laboratory of Ship and Platform Flows: Onur Gecer, Kwang Lee, Yile Li, Greg Tozzi and Talha Ulusoy. They have helped me solve problems and move on countless of times.

Many thanks to Professor Eric Feron and Dr Vlad Gavrilets from the department of Aeronautics and Astronautics for initiating me in the fascinating subject of controls, and to Dr Sungeun Kim for his help in the area of hydrodynamics.

Financial support for this research effort has been provided by the Office of Naval Research.

Iason Chatzakis
Cambridge, 2004

Contents

1. Hydrodynamic forces on lifting bodies operating near the free surface.....	15
1.0 Introduction	16
1.1. The physical problem.....	17
1.1.a.Calm water.....	17
1.1.b. Ambient Waves.....	17
1.1.c.Computational Tool.....	18
1.2. Numerical calculation of hydrodynamic forces and moments.....	19
1.2.a.The Boundary Value Problem	19
Exact Boundary Value Problem	19
Linearization.....	20
Solution	21
1.2.b. Geometry Discretization.....	21
Free Surface.....	21
Foil	22
1.3. Code validation and convergence in infinite fluid flow.....	25
1.3.a. Steady Flow	25
Added mass and Pressure Distribution of simple forms	25
Pressure Distribution and Lift Force on Karman-Trefftz Airfoil	27
1.3.b. Unsteady Flow	31
Time-Harmonic heave and pitch motion	31
1.4. Code validation and convergence in free-surface flow.....	34
1.4.a. Basic Non-Dimensional Parameters.....	34
1.4.b. Domain Length and Grid Size Convergence.....	35
1.4.c. Fixed motion in calm water	37
Moving pressure distribution on the free surface	37
Submerged vortex.....	40
Two-dimensional circular cylinder under a free surface	41
Effect of draft on lift.....	44
Lift on a symmetrical hydrofoil at zero angle of attack.....	44
1.4.d. Incident Waves	45
1.4.e. Free Motions	46
1.5. Motion-induced force coefficients and excitation forces on submerged hydrofoils	51

1.5.a. Motion-induced force coefficients of a submerged hydrofoil	51
Theoretical lift force on heaving hydrofoil in infinite flow	51
Variation of heaving hydrofoil motion-induced force coefficients with draft Froude number	53
Variation of heaving hydrofoil motion-induced force coefficients with frequency at a fixed draft	55
15.b. A simple model for the ambient wave excitation force on a submerged hydrofoil.....	57
Effective angle of attack and wave-induced lift coefficient.....	57
Heave excitation force	60
Phase Shift.....	60
Model Tests	61
2. Motion Control.....	64
2.0 Introduction	65
2.1. Control Theory	66
2.1.a. Classical Control System Design.....	67
2.1.b. Modern Control Systems Design - State Space Approach and Optimal Control	70
Relation between frequency domain and state-space descriptions of a system.....	72
Optimal Control.....	73
Variational calculus approach	74
The Dynamic Programming approach.....	80
Significance of the Q and R weight matrices.....	83
Notes on stochastic disturbances	84
2.1.c. Contemporary Research on the Control of Marine Vehicles.....	86
2.2. Motion control of hydrofoil craft.....	88
2.2.a Vessel heave and pitch equations of motion – derivation of a state- space model.....	89
Hydrofoil craft restoring coefficients.....	90
State-Space Model.....	91
2.2.b LQR control law in two degrees of freedom	94
2.2.c Control System Architecture	95
2.2.d Physical Significance of the Q and R Cost Matrices	95

2.2.e General Vessel Model	96
2.2.f Motion Control of a Hydrofoil Vessel with Hydrostatic Restoring	98
Sinusoidal Incident Wave	99
Random Incident Wave.....	100
2.2.g Motion Control of a Hydrofoil Vessel without Hydrostatic Restoring	
.....	101
Steady-state Error and Integral Feedback	101
Sinusoidal Incident wave	103
Random Incident Wave.....	105
Conclusions and future work	108
Bibliography	109

Table Of Figures

Figure 1: Hydrofoil ship unstable coupled heave and pitch mode	18
Figure 2: Coordinate system for Boundary Value Problem	20
Figure 3: Uniform, Cosine and Half-Cosine panel spacing	23
Figure 4: Discretization for square-section cylinder.....	26
Figure 5: Discretization for circular-section cylinder	26
Figure 6: Pressure distribution on 2-D cylinder	27
Figure 7: Karman-Trefftz section	28
Figure 8: Panel Density Convergence.....	28
Figure 9: Wake length convergence.....	29
Figure 10: Pressure distribution near pressure peak	30
Figure 11: Pressure Distribution on foil – numerical and analytical comparison	30
Figure 12: Lift coefficient for increasing angle of incidence	31
Figure 13: Panel size convergence for unsteady flow.....	32
Figure 14: Lift coefficient and heave displacement in unsteady, infinite flow	32
Figure 15: Lift coefficient with varying frequency.....	33
Figure 16: Aft Domain length convergence	36
Figure 17: Forward Domain length convergence	36
Figure 18: Free-surface grid size convergence.....	37
Figure 19: Free surface elevation with increasing aft domain length.....	37
Figure 20: Pressure distribution moving on the free surface.....	38
Figure 21: Panel length convergence	39
Figure 22: Domain length convergence	39
Figure 23: Submerged vortex lift coefficient (computational and analytic comparison)	41
Figure 24: Submerged vortex drag coefficient (computational and analytic comparison).....	41
Figure 25: 2D cylinder domain length convergence.....	42
Figure 26: 2D cylinder free surface panel length convergence	42
Figure 27: 2D cylinder drag coefficient (computational and analytic comparison)....	43
Figure 28: Free surface elevation at draft Froude No 1.634.....	44
Figure 29: Lift coefficient for varying draft Froude number	45
Figure 30: Diffraction component of free surface elevation by a 2D circular cylinder (Incident plane progressive wave of unit amplitude from the left – cylinder position and diameter not to scale).....	46
Figure 31: Panel Density convergence for heave mode free motion	47
Figure 32: Temporal convergence for heave mode free motion.....	48
Figure 33: Heave response for varying frequency	49
Figure 34: Lift coefficient and heave displacement time histories at T=3.66 sec	50
Figure 35: Lift coefficient and heave displacement time histories at T=12.00 sec	50
Figure 36: Real and Imaginary Parts of Theodorsen function $C(k)$	52
Figure 37: Theodorsen force coefficients.....	53
Figure 38: A_{33} coefficient variation with draft Froude number at $k=0.04$ reduced frequency	54
Figure 39: B_{33} coefficient variation with draft Froude number at $k=0.04$ reduced frequency	55
Figure 40: Free surface elevation with varying draft Froude number	55
Figure 41: A_{33} coefficient variation with frequency for F_n draft=3.50	56
Figure 42: B_{33} coefficient variation with frequency for F_n draft=3.50.....	56
Figure 43: Effective angle of attack.....	58

Figure 44: Lift coefficient at small angles of attack	59
Figure 45: Heave excitation force in absolute wave period $T=12.56$ sec ($\omega=0.5$ rad/sec).....	62
Figure 46: Heave excitation force in absolute wave period $T=7.85$ sec ($\omega=0.8$ rad/sec).....	62
Figure 47: Heave excitation force in absolute wave period $T=6.28$ sec ($\omega=1.0$ rad/sec).....	63
Figure 48: Airplane sketch – negative dihedral angle.....	66
Figure 49: Hydrofoil ship unstable coupled heave and pitch mode	67
Figure 50: Feedback system (1).....	68
Figure 51: Feedback system (2).....	69
Figure 52: F16 aircraft root locus	70
Figure 53: Perturbation around nominal trajectory.....	85
Figure 54: Hydrofoil motion around nominal trajectory.....	86
Figure 55: Flap angles determined by state feedback control law.....	95
Figure 56: Control system architecture	95
Figure 57: USS Taurus.....	97
Figure 58: Model geometry based on USS Taurus.....	98
Figure 59: Heave RMS for controlled and uncontrolled ride in plane progressive wave	99
Figure 60: Heave acceleration RMS for controlled and uncontrolled ride in plane progressive wave	99
Figure 61: Heave displacement time history comparison for $H_{1/3} = 3.00$ m ocean wave	100
Figure 62: Heave displacement time history comparison for $H_{1/3} = 5.00$ m ocean wave	101
Figure 63: Elimination of heave steady-state error by integral feedback	103
Figure 64: Heave displacement with varying q_3 heave state cost (plane progressive wave)	105
Figure 65: Flap angle RMS with varying q_3 heave state cost (plane progressive wave)	106
Figure 66: Heave acceleration RMS with varying q_3 heave state cost (plane progressive wave).....	106
Figure 67: Heave RMS with varying q_3 heave state cost (ocean wave).....	106
Figure 68: Heave acceleration RMS with varying q_3 heave state cost (ocean wave).....	107
Figure 69: Heave displacement time history for $q_3 = 1.00$ (ocean wave).....	107
Figure 70: Heave displacement time history for $q_3 = 50.00$ (ocean wave).....	107

1. Hydrodynamic forces on lifting bodies operating near the free surface

1.0 Introduction

The numerical solution of the flow around a fully submerged hydrofoil under a free surface is treated in the first part of this work. The main objective is the estimation of hydrodynamic forces and the integration of the equations of motion of a lifting body operating at a relatively small draft under the surface of the ocean. These capabilities will be used for the study of motion control of hydrofoil ships in the second part of this work.

A time domain, two-dimensional formulation is used since the vessel motions studied in the second part will be in the heave and pitch modes. A computer code which applies a Boundary Element (Panel) method assuming potential flow around the body is developed and validated. This part begins with the necessary theoretical foundation and analysis. Subsequently convergence tests and validation experiments are presented starting from simple infinite-fluid, fixed-motion experiments and continuing with forced and free motion experiments for free surface flows in calm water and in waves .

1.1. The physical problem

1.1.a. Calm water

In a two-dimensional problem, a hydrofoil moving with a constant horizontal velocity under a free surface is subject to a horizontal drag force and a vertical lift force. These forces have different values than the ones that would occur if the hydrofoil was in an infinite fluid. The horizontal force, apart from the friction, form and three-dimensional vortex induced drag components also includes an additional component due to the creation of a wave flow on the free surface, called wave drag. The lift force is affected by the free surface flow as well, in most cases adversely.

In an ideal fluid flow, both forces have generally non-zero values. A major difference from a fully viscous flow is that the ideal-fluid drag force is composed only of the wave drag and, in the case of three-dimensional flow, the vortex induced drag, the two other components being of a clearly viscous nature.

The lift and drag forces depend on parameters such as foil geometry and angle of attack, foil velocity and submergence draft. In general there exists no analytic solution for the ideal flow around a submerged hydrofoil of arbitrary geometry. Additionally, the large amount of experimental and computational data available for foils operating infinite flow cannot be used in this case since as stated before the presence of the free surface largely affects the flow. However, knowledge of these forces is crucial for hydrofoil ship design and operation, and hence a tool that allows an initial evaluation of the resulting flow could be valuable in the preliminary design phase.

1.1.b. Ambient Waves

A hydrofoil ship operating in ambient waves is subject to unsteady excitation forces due to the incident waves, in addition to the calm water lift and drag. These excitation forces are usually quite large since the vessel is moving at a high mean velocity and hence the encounter frequency with the incident wave system is also large, especially in the head sea condition. The resulting motions of the vessel is characterized by high accelerations and deviations from its mean position. This is quite troublesome for the operation of such craft, military or commercial.

Moreover, hydrofoil craft with fully submerged foils (non surface-piercing) are either marginally stable or even unstable in some modes of motion. As an example we can

1.1. THE PHYSICAL PROBLEM

look at the unstable coupling between the heave and pitch modes as shown in the sketch of a two-foil vessel in figure 1. When the vessel pitches by a small angle ξ_s , a negative angle of attack is induced upon the foils causing a negative heave force. In seakeeping terms (see Newman [1]) this means that a negative restoring coefficient c_{35} between pitch and heave exists. This is an unstable mode of motion for the vessel.

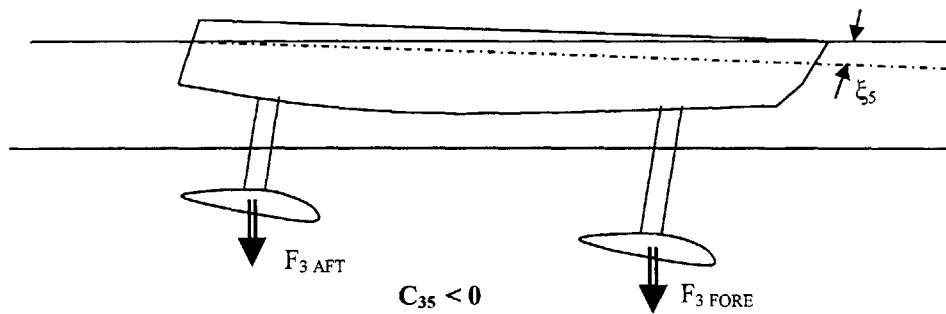


Figure 1: Hydrofoil ship unstable coupled heave and pitch mode

Hence it is quite apparent that an active feedback control system is required to make the vessel dynamically stable.

1.1.c. Computational Tool

In order to study the physical problem of force and motion prediction for hydrofoil ships, a two-dimensional, time domain, boundary element method computer code has been developed and tested. The code as a computational tool predicts the force and moment on a fully submerged hydrofoil operating in calm water and in incident monochromatic or stochastic waves, while in fixed, forced or free motion. It also calculates the hydrofoil's motion in the time domain, in the free motion case. Finally it can be used to test and evaluate various feedback control systems activating trailing edge flaps using optimal control laws.

1.2. Numerical calculation of hydrodynamic forces and moments

The calculation of the hydrodynamic force and moment on the hydrofoil requires knowledge of the flow field around the body. An assumption on the nature of the flow is made here: the flow is considered to be inviscid, irrotational and incompressible. In general hydrofoil ships operate at high velocities with Reynolds numbers in the order of 10^9 and at small angles of attack with little or no flow separation. This justifies a flow calculation under the above assumptions since inertial and gravity forces will dominate the free surface and lifting flow.

In this section, the boundary value problem for the fully submerged lifting or non-lifting body is presented and the numerical method used for its solution described.

1.2.a. The Boundary Value Problem

Exact Boundary Value Problem

Given the previous assumptions on the nature of the flow, a total velocity potential Ψ can be defined representing the flow about the body. Ψ is measured at the reference frame moving with the mean body velocity \mathbf{U} , and the total flow velocity at a point \mathbf{x} on the reference frame is $\mathbf{u}(\mathbf{x},t) = \nabla \Psi$. The exact boundary value problem for Ψ is then

$$(1.1) \quad \left\{ \begin{array}{ll} \text{conservation of mass :} & \nabla^2 \Psi = 0, \text{ in the fluid volume} \\ \text{kinematic free surface condition :} & \left(\frac{d}{dt} + \nabla \Psi \cdot \nabla \right) [z - \zeta(x,t)] = 0, \\ & \text{on } S_F \text{ } z = \zeta(x,t) \text{ free surface} \\ \text{dynamic free surface condition :} & \frac{d\Psi}{dt} = -g\zeta - \frac{1}{2} \nabla \Psi \cdot \nabla \Psi, \\ & \text{on } S_F \text{ } z = \zeta(x,t) \text{ free surface} \\ \text{body boundary condition :} & \frac{\partial \Psi}{\partial n} = 0, \text{ on } S_B \text{ body surface} \\ \text{far - field condition :} & \Psi \rightarrow Ux, \text{ for } S_{\text{FAR}} \text{ } |\mathbf{x}| \rightarrow \infty \end{array} \right.$$

The coordinate system used in defining the BVP (1.1) can be seen in Figure 2.

In the dynamic free surface condition we assumed the atmospheric pressure to be constant and equal to zero since the air's density is three orders of magnitude smaller than the water's [2].

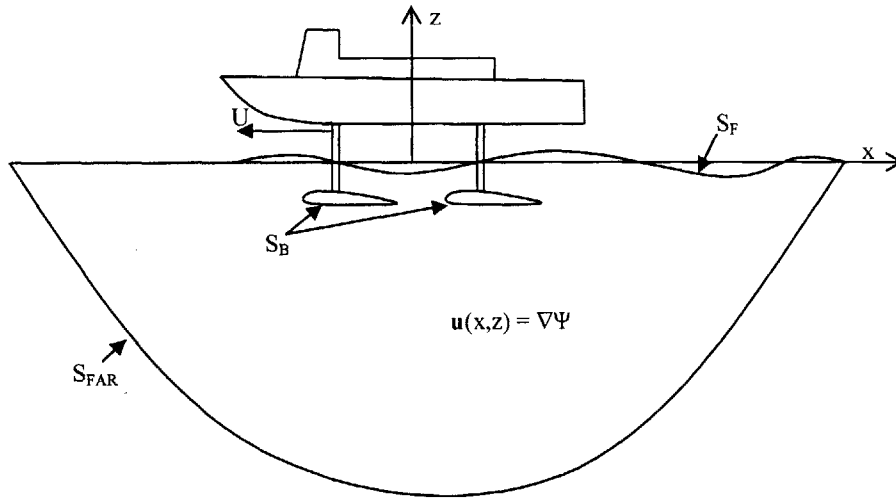


Figure 2: Coordinate system for Boundary Value Problem

Linearization

The total potential Ψ is decomposed as follows:

$$(1.2) \quad \Psi = \Phi_0 + \phi_m$$

Φ_0 represents the basis flow around which the problem is linearized [2]. In this work the free stream flow $-Ux$ is chosen as the basis flow. The memory potential ϕ_m represents the flow perturbation due to the body presence. Linearizing around the basis flow and the mean free surface position $z = 0$, the boundary value problem for the memory potential is

$$(1.3) \quad \begin{cases} \nabla^2 \phi_m = 0, & \text{in the fluid volume} \\ \left(\frac{\partial}{\partial t} - U \frac{\partial}{\partial x} \right) \zeta(x,t) = \frac{\partial \phi_m}{\partial z}, & \text{on } z=0 \\ \left(\frac{\partial}{\partial t} - U \frac{\partial}{\partial x} \right) \phi_m = -g\zeta, & \text{on } z=0 \\ \frac{\partial \phi_m}{\partial n} = -\vec{U}\hat{n}, & \text{on the body surface} \\ \phi_m \rightarrow 0, & \text{for } |x| \rightarrow \infty \end{cases}$$

where ζ is the free surface elevation, and \hat{n} is the unit normal vector on the body surface pointing inside the body.

Solution

Green's second identity is used to transform the previous boundary value problem for the memory potential into boundary integral equations. In two dimensions, Green's identity produces

$$(1.4) \quad \pi\phi_m(\bar{x}) - \iint_{S_B \cup S_F} \frac{\partial\phi_m(\bar{\xi})}{\partial n_\xi} G(\bar{x}; \bar{\xi}) ds_\xi + \iint_{S_B \cup S_F} \phi_m(\bar{\xi}) \frac{\partial G(\bar{x}; \bar{\xi})}{\partial n_\xi} ds_\xi = 0$$

where S_B is the body boundary and S_F the free surface. In this work, the two-dimensional Rankine source

$$(1.5) \quad G(\bar{x}; \bar{\xi}) = \ln r, \quad r = |\bar{\xi} - \bar{x}|$$

is used as a Green function. This Green function satisfies the Laplace equation in the fluid domain.

The body boundary condition is satisfied through the forcing of the memory potential on the body, in the boundary integral formulation.

The free surface conditions are satisfied through the time evolution equations. If $t=t_n$ is the current timestep, the kinematic free surface condition is satisfied using an explicit Euler time discretization with the solution for the memory flux on the free surface from the previous timestep $t=t_{n-1}$. The free surface elevation is thus calculated explicitly for the current timestep. The dynamic free surface condition is then satisfied using an implicit Euler time discretization. The solution for the free surface elevation in the current timestep is thus used for the implicit calculation of the memory potential on the free surface. This method is known as an *Implicit Euler* scheme and a detailed description can be found in [2].

1.2.b. Geometry Discretization

In this section the geometry discretization methods which are used for the creation of the free surface and body panels are described.

Free Surface

The free surface discretized simply with constant-length panels which span the free surface domain. The length of the free surface panels proved to be an important parameter

that affected solution convergence and numerical stability. The non-dimensional panel Froude number:

$$Fr_h = \frac{U}{\sqrt{gh}}, \text{ where } U \text{ is the foil speed and } h \text{ the free surface panel length}$$

is a measure of free surface panel size and roughly speaking expresses the number of panels per wave. In later sections, free surface panel length convergence tests are carried out before the execution of numerical experiments.

Foil

The foil geometry is input through a set of points (offsets). While a bigger number of offsets generally guarantees a greater accuracy in the geometrical representation, the number of panels that are used to describe the body is independent of the number of input offsets. The user can create a foil-shaped body with as few as 4-5 offsets on each side.

For the purposes of the code's validation, a Karman-Trefftz foil geometry is used in many of the numerical experiments that follow in later sections, since an analytical solution for the flow around it exists through conformal mapping methods.

The panel creation method for the foil body follows.

Cubic Spline Interpolation

Initially cubic spline curves are interpolated through the input offsets. In particular, two spline curves are used, one for each side of the foil (upper and lower). An end condition of a normal tangent is enforced at the fore end of the foil in order to provide a rounded leading edge. The spline curves provide an analytic approximation of the foil surface and are available for the creation of the body panels.

Consequently, a number of panels is created on the body. Each panel's endpoints (vertices) lie on the spline curve. In areas of high curvature, the panel center's distance from the spline curve is greater and hence it makes sense to use higher panel densities in order to describe areas of high curvature.

The number of panels used is user-specified. In general a larger number of panels offers a more accurate description of the foil geometry and contributes positively to the simulation accuracy as will be demonstrated in later sections. However, the computational effort is burdened with the square of the total number of panels and hence the minimum required number of panels should be used.

Panel Spacing (even, cosine, half-cosine)

The way panels are distributed on the body also has an effect on solution accuracy, since as mentioned before, areas of high curvature require a higher panel density. This area is in most cases the foil leading edge.

Using an even panel spacing is not efficient computationally since one has to use a very fine overall panel density in order to get the required density at the leading edge. Cosine spacing and half-cosine spacing proved to be much more efficient, making for fine distributions on the leading edge while allowing lower densities in the middle of the foil where curvature is very small. Half-cosine spacing specifically proved to be the most efficient spacing, since apart from providing very high leading-edge panel density it also keeps the panels large near the trailing edge. A comparatively large trailing edge panel size is beneficial for the numerical implementation of the Kutta condition.

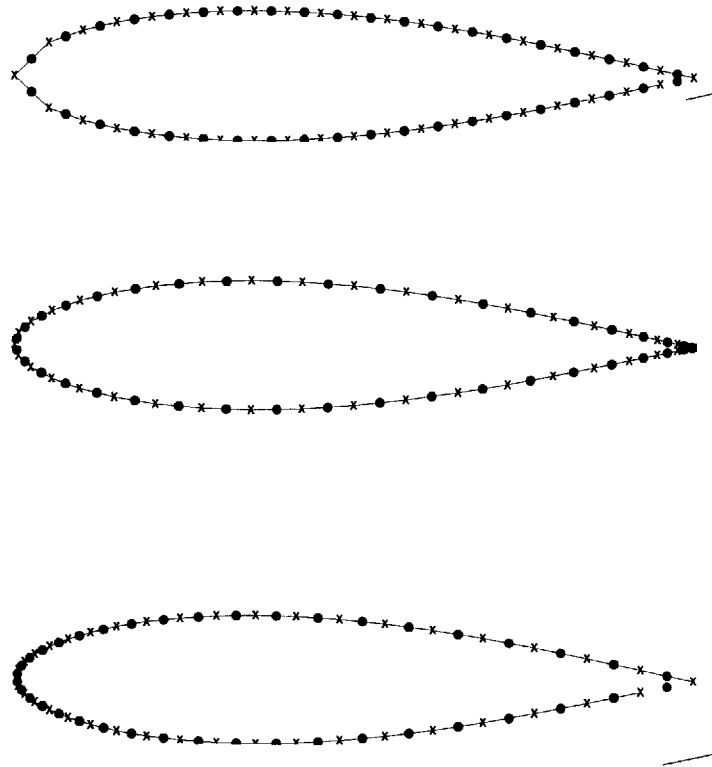


Figure 3: Uniform, Cosine and Half-Cosine panel spacing

In Figure 3 a Karman-Trefftz foil discretization is shown, with the panel centers symbolized with circles and the vertices with x's. 10 panels were used on each side of the body for clarity of presentation. The top plot is an even-spaced discretization where the loss of accuracy in the

1.2. NUMERICAL CALCULATION OF HYDRODYNAMIC FORCES AND MOMENTS

leading edge is apparent. The second and third plots are cosine and half-cosine spacing discretizations respectively.

1.3. Code validation and convergence in infinite fluid flow

A set of numerical experiments was carried out in order to investigate the numerical robustness and physical accuracy of the computational tool. This section includes the experiments for steady and unsteady infinite flow, in the absence of a free surface. First, the added mass of the 2D circular and square cylinders is calculated and compared with the analytical result for potential flow. The pressure distribution on a circular cylinder is calculated and compared to the analytic result, and the pressure distribution on a lifting Karman-Trefftz airfoil is subsequently calculated and compared to the conformal mapping solution. Finally, the same airfoil geometry is set to a time-harmonic forced motion and the resulting force calculation is confirmed qualitatively. Numerical convergence tests are shown for the third and fourth experiments. This allows the investigation of the effect that various discretization parameters (such as panel density and wake length) have on the solution.

1.3.a. Steady Flow

Added mass and Pressure Distribution of simple forms

As a first validation for the code, the computational added mass estimation of two simple forms was compared to their analytical values. The forms tested were a 2-D square cylinder and a 2-D circular cylinder. The analytic calculation of the infinite-fluid added mass of those forms has been carried out by conformal mapping methods and can be found in [1]. The computational results showed good agreement in the order of 0.3% with the theoretical predictions. The results can be seen in Table 1. The panel geometry for square and cylinder can be seen in Figure 4 and Figure 5 respectively.

Form	A_{11} (theoretical) kg	A_{11} (comp.) kg	Accuracy	No. of Panels
2D square	$4.754 \rho \alpha^2 =$ 1218.2125	1222.4170	0.3%	160
2D circular	$\pi \rho \alpha^2 =$ 805.30311 where $\rho=1025 \text{ kg/m}^3$	805.03750	0.03%	100

Table 1

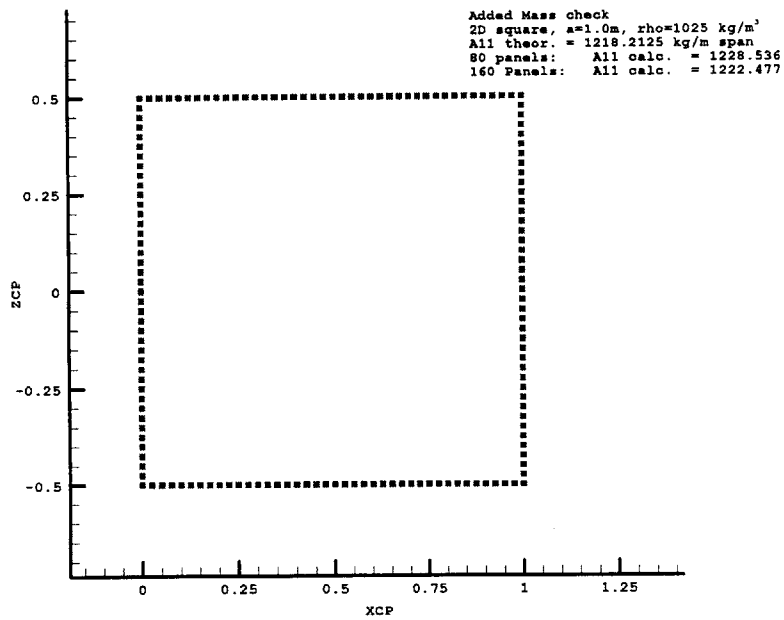


Figure 4: Discretization for square-section cylinder

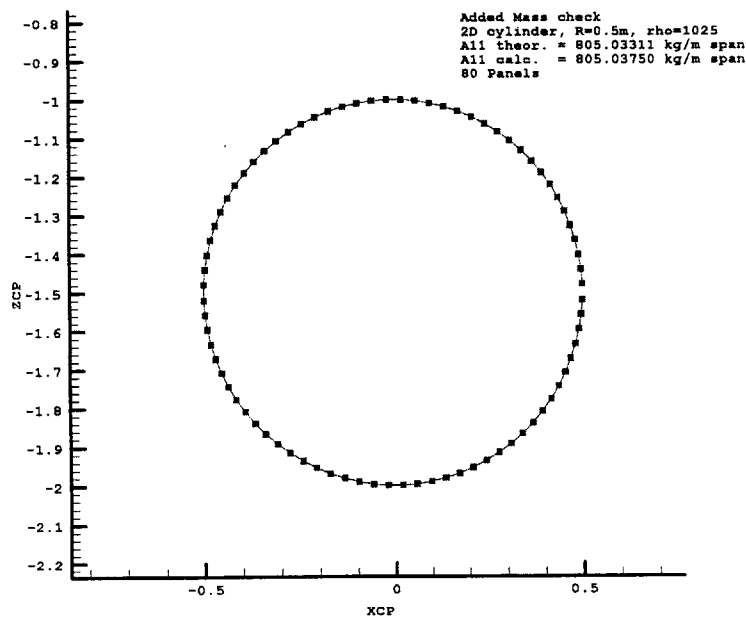


Figure 5: Discretization for circular-section cylinder

The next step was to check the computational estimation of the pressure distribution on a 2D cylinder without circulation with the theoretical solution which can be found in [1]. The comparison was satisfactory, after a numerical solution using 100 panels. A graphic comparison can be seen in Figure 6.

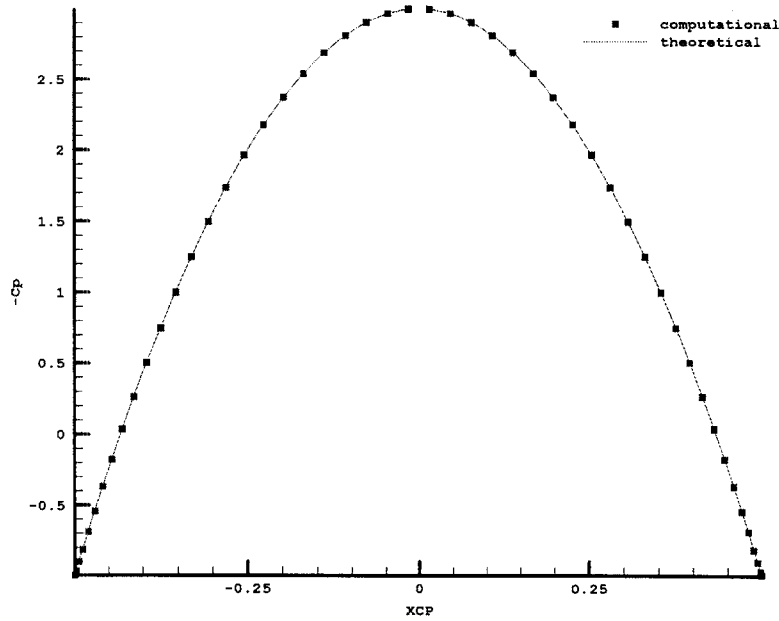


Figure 6: Pressure distribution on 2-D cylinder

Pressure Distribution and Lift Force on Karman-Trefftz Airfoil

Since an analytical solution (through conformal mapping methods) exists for the 2-D Karman-Trefftz foil, the next validation step was to compare the code’s predictions with the conformal mapping solution. A symmetrical foil with the following characteristics was used:

Karman-Trefftz foil geometry		
xc	yc	tail angle
-0.1	0.0	20°

Table 2

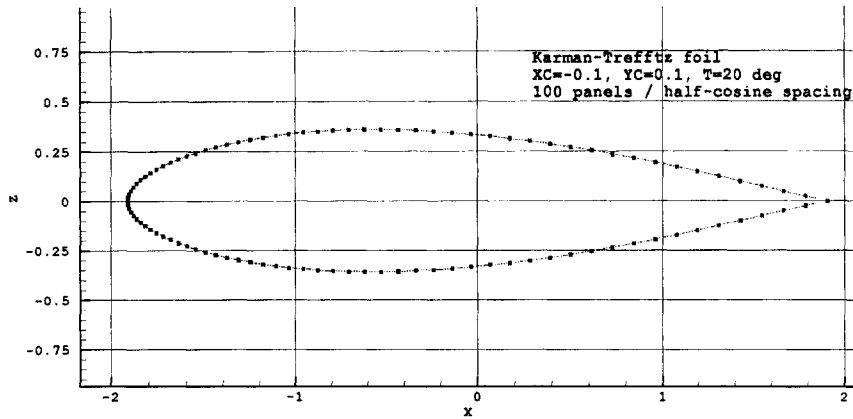


Figure 7: Karman-Trefftz section

In Figure 7 we can see the foil geometry used.

Panel density convergence

The first numerical test was to examine the solution convergence with increasing panel density. We ran the code with the foil at an angle of attack of 8.0° increasing the number of panels on the foil from 10 to 200. The resulting calculation for the lift coefficient can be seen in Figure 8. It is evident that there is convergence using more than 60 panels on the foil. Most of the following runs in this study were conducted using 80 to 100 panels on the foil, as an acceptable trade-off between accuracy and computational speed.

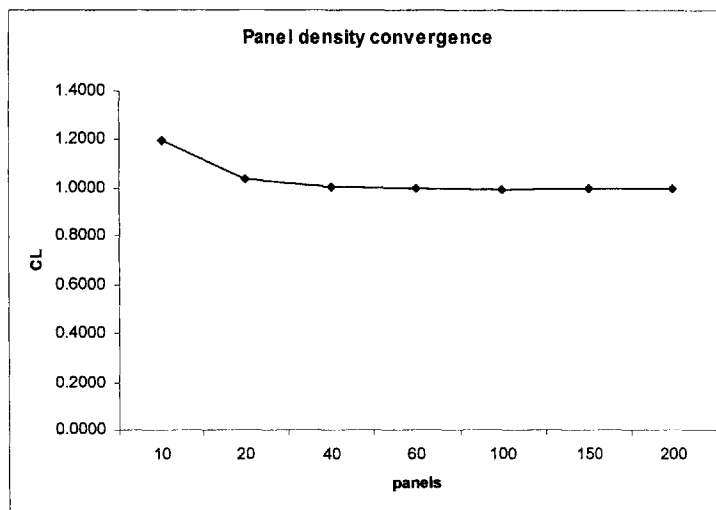


Figure 8: Panel Density Convergence

Wake length convergence

Theoretically the wake sheet streaming from the foil's trailing edge extends to an infinite distance aft. This is not possible in the computational case where the wake sheet has to be truncated at some finite distance downstream. In the steady flow case, one single huge wake panel can be modeled, extending to a very large distance downstream without additional computational burden. In the unsteady case however, where at each timestep the change in circulation around the foil is shed into the wake, the wake has to be modeled using a large number of small wake panels, whose length defines the timestep length. Using a large wake sheet length increases the required number of panels and hence adds to the computational burden.

Since the total wake length (at which the wake sheet is truncated downstream) was found to have an important effect on the solution, a convergence test is presented below using the total wake length as a parameter.

Using the same foil and angle of attack as in the previous test ($\alpha = 8.0^\circ$) we ran the code using a truncated wake length starting from 1 chord aft of the trailing edge and gradually increasing it to 200 chords. The result can be seen in Figure 9, together with the analytical result calculated using conformal mapping. It is evident that there is satisfactory convergence above 30 chords wake length, where the difference with the theoretical result is less than 2%. In most of the following runs in this work a wake length of 30 to 50 chords was used.

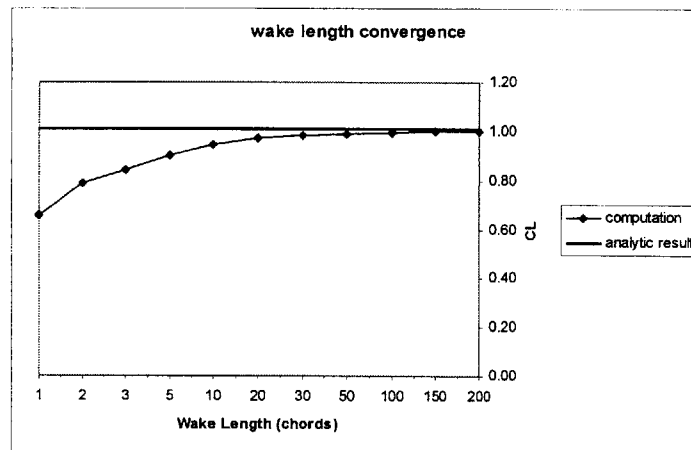


Figure 9: Wake length convergence

Another good display of wake length effect and convergence is the pressure distribution. In Figure 10 we can see the pressure distribution in the region of the suction peak in the forward part of the foil for 8.0° angle of attack. As in the lift coefficient results, the

solution converges in a satisfactory manner above the 30 chords wake length. As we will see in the next section, solution accuracy compared with theoretical results is quite high.

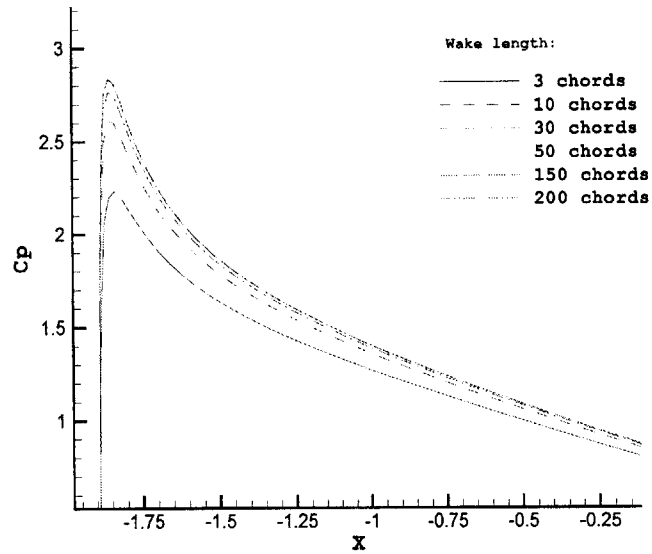


Figure 10: Pressure distribution near pressure peak

Solution accuracy

In Figure 11 we can see the comparison between the pressure distribution on the foil as predicted by the code and as calculated using conformal mapping methods at 8.0 degrees angle of incidence. The computation was done using 100 panels on the foil and half-cosine spacing.

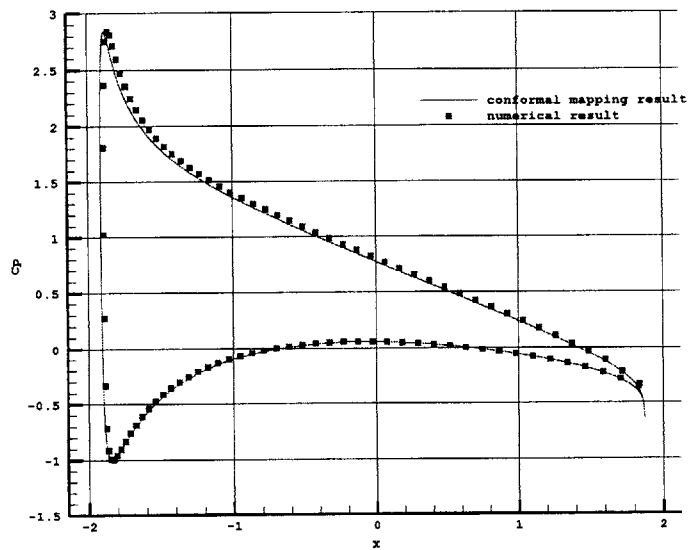


Figure 11: Pressure Distribution on foil – numerical and analytical comparison

In Figure 12 we can see the lift coefficient versus angle of attack as predicted by the code in comparison with the conformal mapping result, for angles of incidence up to 16.0°. The computation was done using 100 panels on the foil and a total wake length of 50 chords.

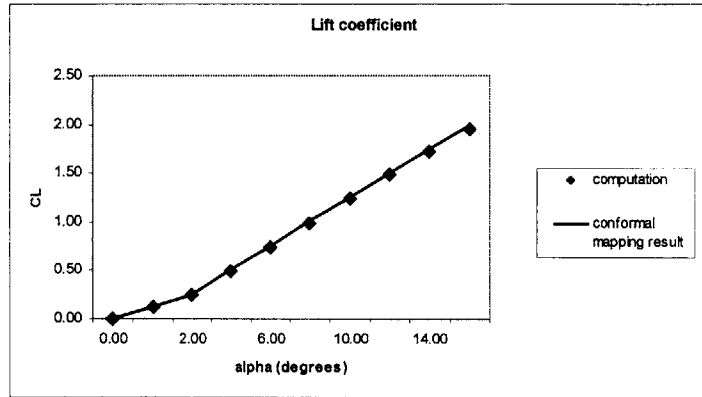


Figure 12: Lift coefficient for increasing angle of incidence

The previous indicatory results show that the code’s behavior in time-steady, infinite flow experiments is numerically robust and theoretically correct. This is an essential validation for our solver before moving on to unsteady and free-surface computations.

1.3.b. Unsteady Flow

Time-Harmonic heave and pitch motion

As an unsteady flow test, the airfoil geometry from the previous experiments is subjected to a time harmonic pitch and heave motion. Initially solution convergence with panel density is tested, and subsequently the time history of the lift coefficient is calculated with varying frequency of oscillation. The result is qualitatively confirmed with unsteady hydrofoil theory.

Panel density convergence

As in the steady flow case, a convergence test with the panel density as parameter is appropriate in order to validate the code’s behavior. As an example, in Figure 13 we can see a set of results for increasing panel density. A reduced frequency

$$k = \frac{C\omega}{2U}$$

of 0.10 is used. The dimensionless parameter of reduced frequency gives an idea of the ‘unsteadiness’ of the flow – it expresses the wave number of the vorticity shed in the wake (see Newman [1]). The same foil geometry as in the steady flow experiments is used. In Figure 13, an enlargement of the maximum lift phase during part of the oscillation cycle is displayed for clarity.

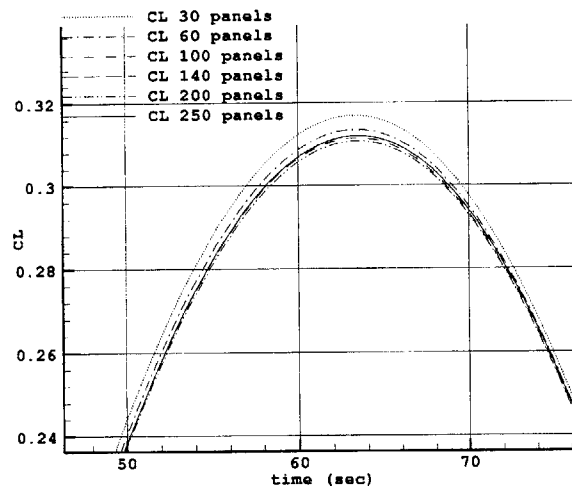


Figure 13: Panel size convergence for unsteady flow

In Figure 14 are the lift coefficient and heave displacement versus time, for the 100-panel solution, with reduced frequency of 0.10. As expected, a phase difference of around 90° results between the displacement and the force.

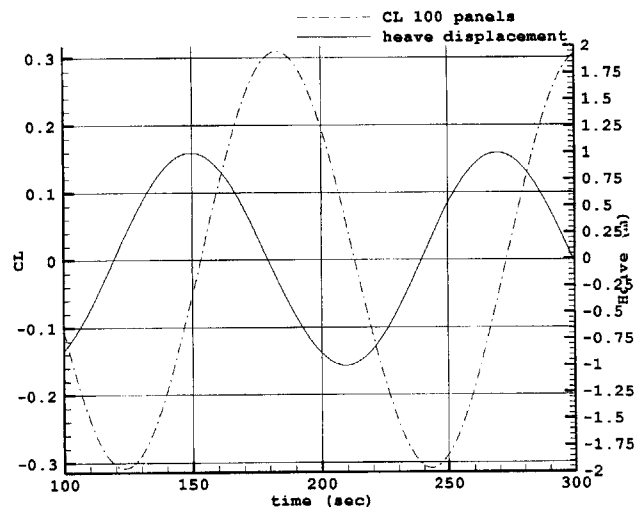


Figure 14: Lift coefficient and heave displacement in unsteady, infinite flow

Change of amplitude and phase of lift force due to variation in frequency

Unsteady hydrofoil theory predicts a change in the amplitude and phase of the lift force on a hydrofoil when the reduced frequency is varied. This change is not monotonic, and it is described by the Theodorsen function (for more details refer to [1]). In the next figure we can see the variation in lift coefficient as the reduced frequency is increased. The foil follows a harmonic oscillation in pitch with an amplitude of 8.0° .

1.3. CODE VALIDATION AND CONVERGENCE IN INFINITE FLUID FLOW

These results confirm the code's robustness in time-unsteady experiments, which will be necessary for time-domain motion control simulations.

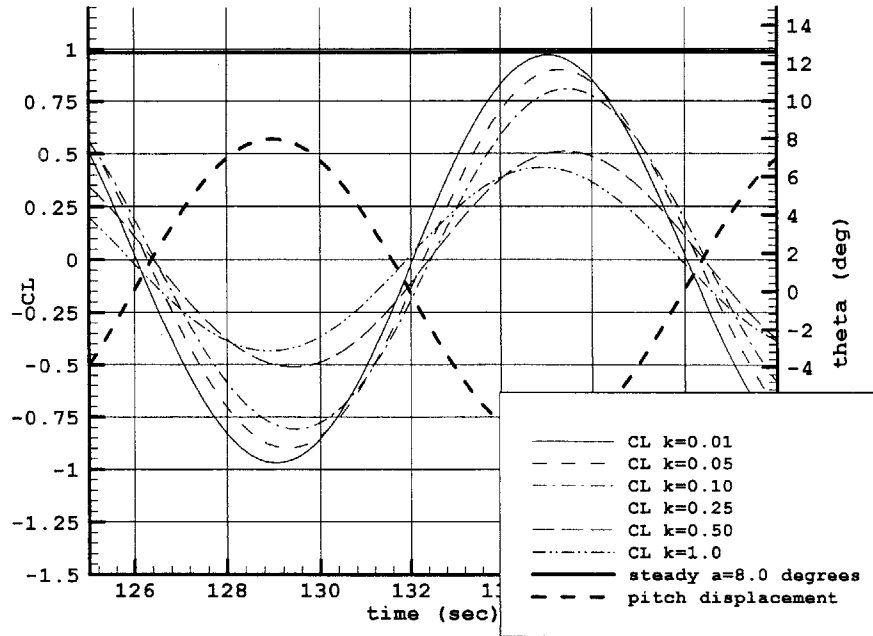


Figure 15: Lift coefficient with varying frequency

1.4. Code validation and convergence in free-surface flow

Convergence characteristics and solution accuracy of the code in free surface flows are tested in this section. Some important parameters that describe the physics of the free surface flow and affect numerical convergence are initially presented. Basic spatial and temporal convergence experiments follow. The final subsections include some experiments with known analytic solutions or clear physical aspects, that serve to validate the simulation performance of the code. Solution convergence checks are also presented for most of those experiments. Flow cases with calm water or incident waves and forced or free motion are included.

1.4.a. Basic Non-Dimensional Parameters

The following five non-dimensional parameters were found to have a profound effect on the solution. The first four have been defined as ‘Froude numbers’, since they have the same form as the dimensionless Froude number which expresses the ratio of inertial over gravitational forces. The first two (draft and chord Froude number) have a physical significance. The other three only have numerical importance, and have been found to affect the spatial and temporal stability of the solution.

Draft Froude number:

$$Fn_H = \frac{U}{\sqrt{gD}},$$

where D the mean draft.

Expresses the magnitude of the free surface’s effect on the flow around the hydrofoil – it is essentially a dimensionless draft.

Chord length Froude number:

$$Fn_H = \frac{U}{\sqrt{gC}},$$

where C is the chord length.

Has a similar significance to the length Froude number of a surface ship.

Aft domain length Froude number:

$$Fn_H = \frac{U}{\sqrt{gX_{AFT}}},$$

where X_{AFT} is the computational domain length aft of the foil.

Expresses the relative length of the wavelength of the waves radiated from the foil to the length of the truncated free surface domain downstream of the foil – essentially, how many waves the computational domain fits.

Free surface panel length Froude number:

$$Fr_h = \frac{U}{\sqrt{gh}},$$

where U is the foil speed and h the free surface panel length.

Expresses the panel density per wave length.

Non-dimensional timestep β (free surface panel number):

$$\beta = \frac{\sqrt{h/g}}{\Delta t},$$

where Δt the timestep size and h the free surface panel length.

This parameter controls the temporal stability of the Euler-Emplicit free surface solution scheme (for details see Kring [2]). We have to note here that since lifting flows are simulated with the use of wake panels, the timestep length is defined by the ratio of wake panel length and ambient velocity. This is because the circulation shed from the trailing edge is moved downstream one panel per timestep. In order for this treatment to have some physical accuracy, the timestep size has to be such that circulation would be convected for a distance of one panel length by the ambient velocity.

Hence the timestep cannot be adjusted directly using the value of β as shown in [2] in order to ensure temporal stability of the free surface solution. In practice, the timestep is adjusted by the wake length and ambient velocity, and then the value of β is checked, and the wake length and timestep re-adjusted if required.

1.4.b. Domain Length and Grid Size Convergence

The first step is to examine the code convergence relative to the aft domain and grid Froude numbers, which were found to be the most influential parameters in the steady-state free surface calculations.

The same foil geometry as in the infinite fluid runs that preceded is used. The angle of attack is kept constant at 8.0 degrees. The draft and chord Froude numbers are also kept constant at 1.634 for a chord/draft ratio of 1.0.

In Figure 16 we can see the numerical effect of the total domain length, in Figure 17 the effect of the domain length forward of the foil and in Figure 18 the effect of the grid Froude number. It is evident that the domain Froude numbers have a more profound effect, and a relatively long domain is required in order to achieve convergence. However,

convergence occurs in both cases, and these tests serve as tuning runs for the definition of the minimum domain length and the maximum grid size for the subsequent calculations.

Two numerical phenomena that were observed were a long-wavelength sloshing effect, as the forward domain size increased and a very small wavelength, high frequency numerical resonance which also occurred as the forward domain length increased. The long-wavelength resonance caused a periodic fluctuation in the forces magnitude and the free surface elevation. The high frequency resonance formed wavelets that were 3-4 panels long and did not affect the average values; it did cause the numerical scheme to diverge though, below a forward domain Froude number of about 0.15. Both kinds of waves radiate forward of the body and are eventually absorbed by the numerical beach.

The first phenomenon occurs mainly in the steady-state runs and can be averaged out in the force calculations. The second phenomenon can be treated by the correct application of numerical filtering at certain timesteps. Both are described by Kring [2].

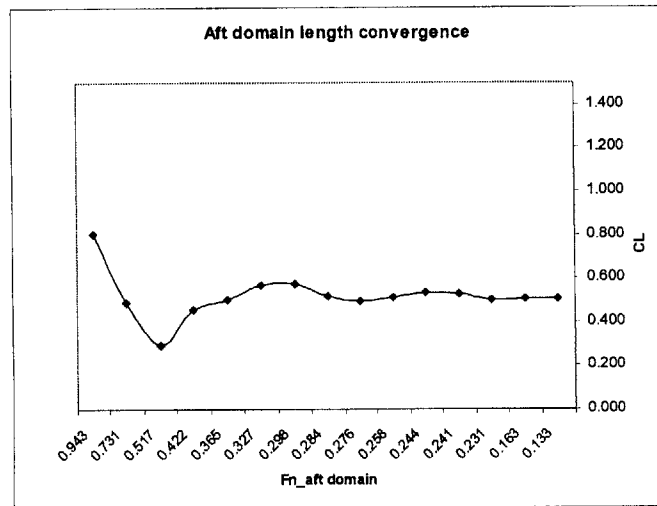


Figure 16: Aft Domain length convergence

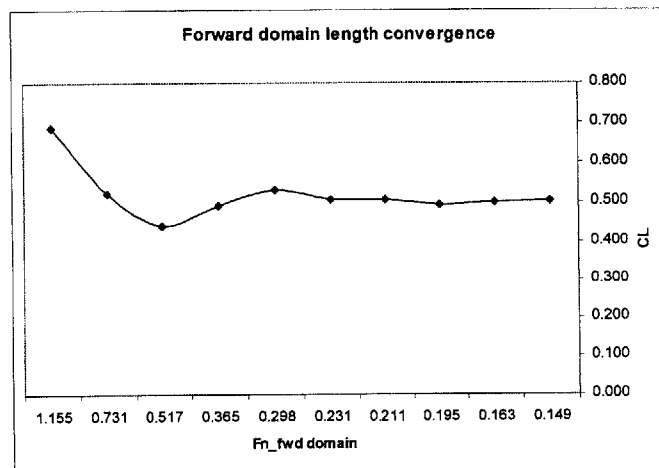


Figure 17: Forward Domain length convergence

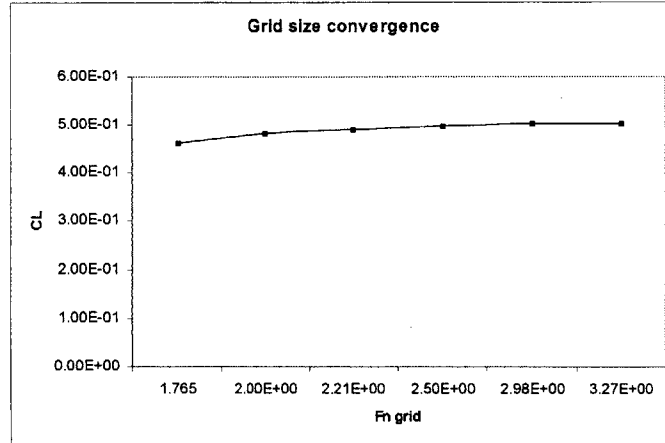


Figure 18: Free-surface grid size convergence

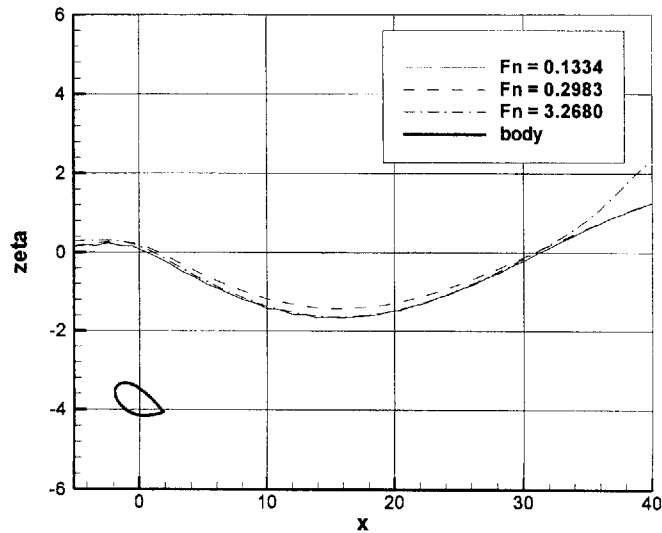


Figure 19: Free surface elevation with increasing aft domain length

1.4.c. Fixed motion in calm water

In this sub-section a number of free surface experiments for which analytical solutions exist are presented. These are a pressure distribution on the free surface moving with constant velocity (resembling an surface-effect ship), a submerged vortex and a submerged circular cylinder.

Moving pressure distribution on the free surface

The flow created by a pressure distribution applied on the free surface and moving with constant velocity has a known analytic solution [3]. In two-dimensional flow, the rate of energy transfer from a pressure distribution $p(x)$ moving with constant velocity U is

$$W = \frac{\rho}{\rho U} \int_{-\infty}^{+\infty} \int_{-\infty}^{+\infty} p(x)p(\xi) \cos v(x - \xi) dx d\xi, \text{ where } v = \frac{g}{U^2} \text{ and } \rho \text{ density}$$

The resulting wave resistance is

$$R_w = \frac{W}{U}$$

The code's behavior was tested with the application of the following pressure distribution

$$p(x) = p_0 \frac{1}{\sqrt{2\pi}} e^{-0.005x^2},$$

which proved to be adequately smooth, in order not to cause local numerical instabilities. The pressure distribution and the resulting wave elevation can be seen in Figure 20.

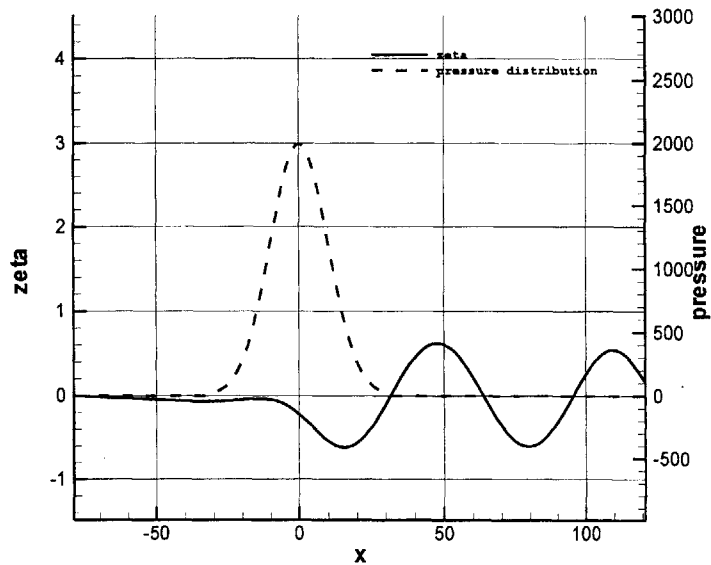


Figure 20: Pressure distribution moving on the free surface

Convergence

Convergence tests were run for the free surface grid size (Figure 21) and for the domain length (Figure 22), using wave resistance as the critical variable. Free surface grid size convergence tests showed satisfactory convergence above a grid Froude number of around 3.00, a value very close to the one found in the convergence tests of section *b*. For practical purposes, a grid Froude number between 2.90 and 3.00 was used in the subsequent runs. Domain length tests showed a satisfactory convergence below a domain Froude number of around 0.20.

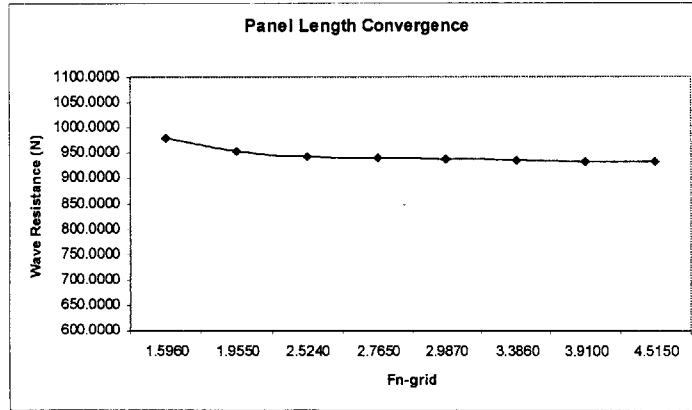


Figure 21: Panel length convergence

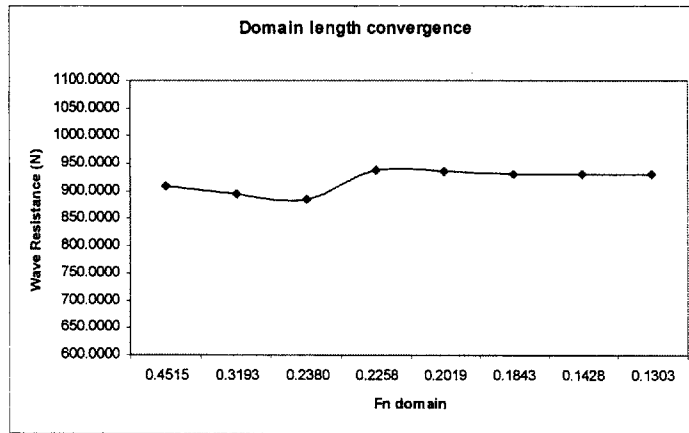


Figure 22: Domain length convergence

Comparison with analytical solution

The converged results for wave resistance were compared with the analytical solution for the pressure patch’s wave resistance. We must note here that the calculation of wave resistance was done through pressure integration on the free surface (accounting for the free surface slope in the x-direction). In order to validate our solution we also calculated the wave resistance through the wave momentum flux of the two-dimensional trailing wake:

$$R_w = \frac{1}{4} \rho g A^2, \text{ where } A \text{ the amplitude of the free surface elevation}$$

This formula has been derived for plane progressive waves of amplitude *A*, and therefore is used here as an approximation. However, a relative agreement between the pressure integration and the momentum integration values can help ensure the consistency of our solution. An accuracy in the order of 1% was achieved when calculating resistance with pressure integration, and in the order of 5% when calculating with momentum integration. The results can be seen in Table 3.

Wave Resistance of Pressure Patch			
Run parameters	Results	value (N)	error (%)
$F_{N \text{ GRID}} = 2.9150$ $F_{N \text{ DOMAIN}} = 0.1843$	Analytical	921.70	-
	Computational (pressure integration)	930.30	0.9%
	Computational (wave momentum) $A \approx 0.643 \text{ m}$	965.90	4.7%

Table 3

Submerged vortex

Circulation

Before we describe the next validation step, we can take a quick look at the accuracy of the numerical pressure integration around the body which is performed in order to calculate hydrodynamic forces. While lift and drag forces are calculated by integrating the hydrodynamic pressure on the body surface, the Kutta-Joukowski theorem in infinite fluid claims:

$$L = \rho U \Gamma$$

The circulation Γ in our case is equal to the potential jump at the foil's trailing edge:

$$\Gamma = \Delta\phi_{t.e.}$$

Hence the lift coefficient can be calculated, apart from pressure integration, by the formula:

$$C_L = \frac{2\Gamma}{U \cdot \text{Chord}}$$

If the numerical pressure integration scheme is sound, the values of the lift coefficient calculated by pressure integration and by the previous formula should be very close. A brief test of this claim follows, for an angle of attack of 8.0 degrees:

Method	C_L (calculated by pressure integration)	C_L (calculated from the value of circulation)	Difference (%)
Value	1.009	1.005	0.4

The previous will help calculate the total force on a submerged vortex and compare the result with the analytical solution.

Comparison with analytic solution for submerged vortex

The lift and drag forces on a submerged vortex of strength Γ are given analytically [3]:

$$L = \rho U \Gamma - \rho \frac{\Gamma^2}{4\pi D} + \rho \frac{\Gamma^2}{\pi} \text{ve}^{-2vD} \text{Ei}(2vD)$$

$$D = \rho U \Gamma^2 e^{-2vD},$$

where $v = \frac{g}{U^2}$, D draught

We expect an agreement between the theoretical and computational calculation of the lift and drag forces starting from deep water and ascending to a draft Froude number of about 1.50. Above this draft, the distance of the foil to the free surface starts becoming too small for it to be approximated by the flow field of a single point vortex. In Figure 23 we can see the comparison of the lift coefficient for analytic and computational solutions, and in Figure 24 the drag coefficient. Comparison is satisfactory up to a draft Froude number of around 1.60.

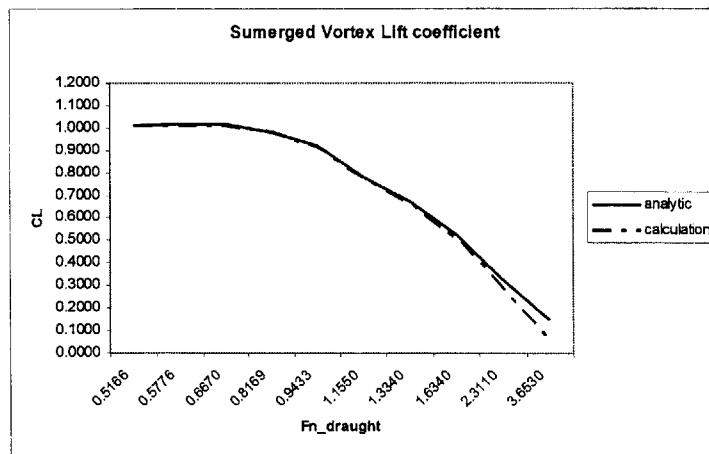


Figure 23: Submerged vortex lift coefficient (computational and analytic comparison)

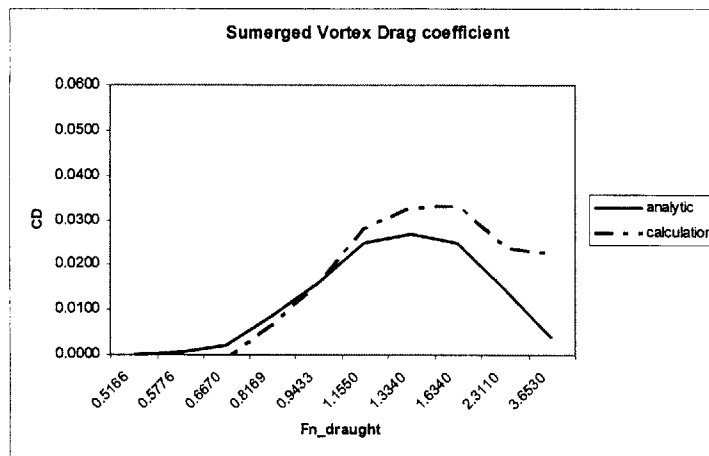


Figure 24: Submerged vortex drag coefficient (computational and analytic comparison)

Two-dimensional circular cylinder under a free surface

Convergence Tests

Since a circular cylinder produces a different flow case than that of a lifting body like the previous ones, some convergence experiments are initially conducted. The two main parameters investigated are, as before, domain length and free surface panel length. The non-dimensional timestep size was also found to greatly affect numerical stability, so the following convergence tests were conducted after a proper range for the non-dimensional timestep is established, where the free surface solution is stable.

In Figure 25 we can see the drag coefficient convergence with domain length (decreasing domain Froude number), and in Figure 26 the drag coefficient convergence with free surface panel size. Since this is a non-lifting flow, the drag force was the primary solution variable to be observed.

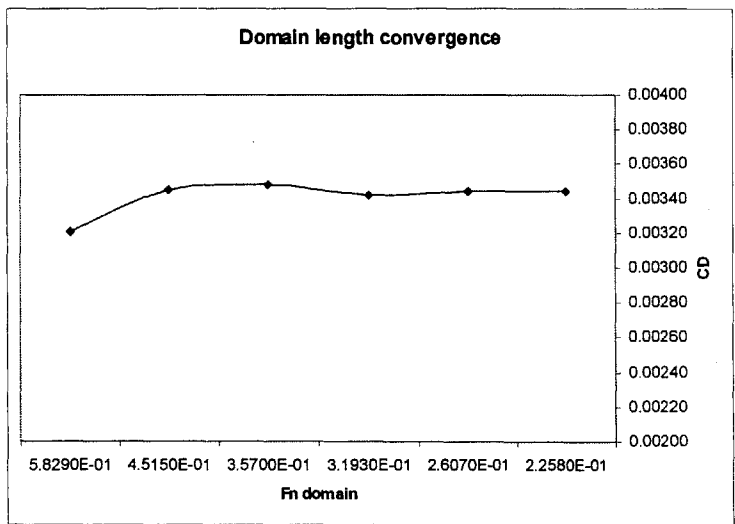


Figure 25: 2D cylinder domain length convergence

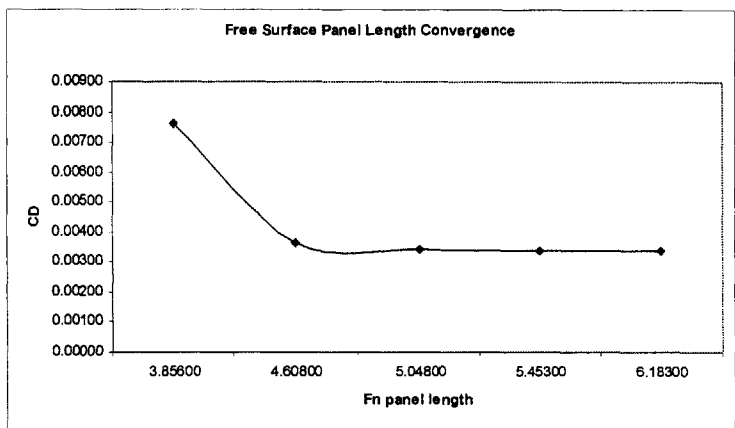


Figure 26: 2D cylinder free surface panel length convergence

Drag Force

Havelock's series solution for the wave drag force exerted on a circular 2D cylinder is given analytically by Wehausen and Laitone [3, pp 574-577]. A number of numerical experiments were conducted in order to validate this code's performance in comparison with the first term of the series solution's prediction [5]. Flow geometry was used as parameter for the runs, quantified through the ratio of cylinder radius over draft a/d . Four different ratios were tested, from $a/h=0.05$ to $a/h=0.167$. For each a/h ratio, draft Froude number was used as a varying parameter. In Figure 27 we can see the results, which show a satisfactory prediction of wave drag by the code.

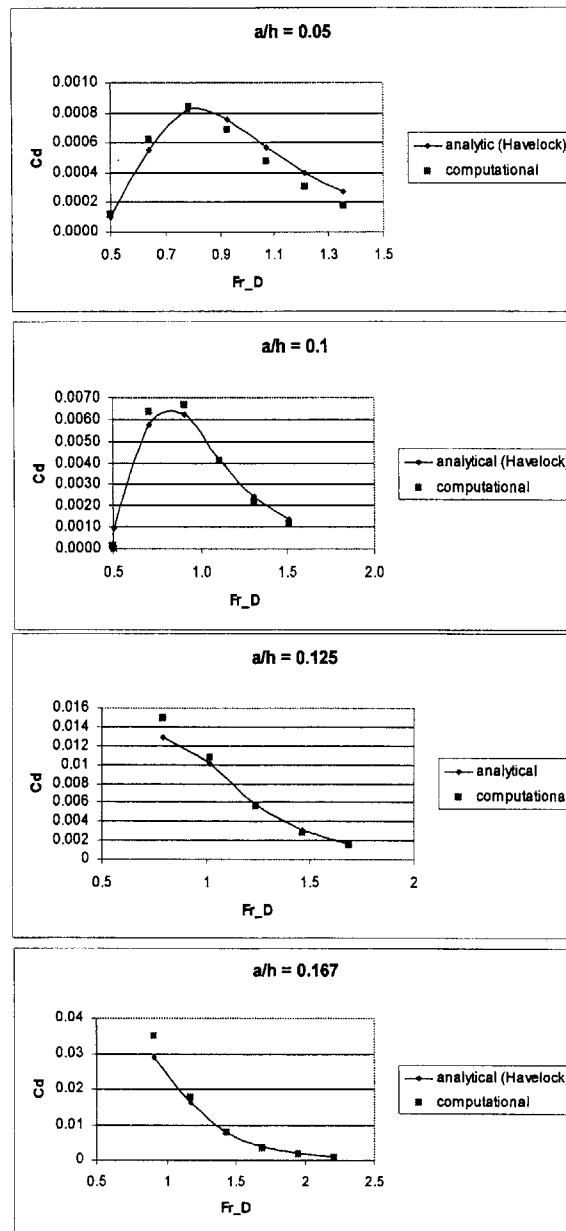


Figure 27: 2D cylinder drag coefficient (computational and analytic comparison)

Effect of draft on lift

It was apparent from the first experiments with lifting foils that while the lift force assumes its infinite-flow value at deep drafts (small draft Froude numbers), it generally becomes smaller when approaching the free surface (increasing draft Froude number).

In Figure 28 we can see a sample illustration of the calculated free-surface elevation at a draft Froude number of 1.634, for an angle of attack of 8.0 degrees.

Lift on a symmetrical hydrofoil at zero angle of attack

As mentioned in [3], a symmetrical foil can experience a lift force when operating near a free surface due to the free surface flow. The symmetrical foil geometry used in the previous experiments was used here as well. In Figure 29 we can see that the lift force is, as expected, zero in deep water and takes a negative non-zero value as the foil approaches the surface (increasing draft Froude number). The negative lift force is in agreement with the previous experiment in this section where it is apparent that the positive lift force experienced by the foil at 8.0 degrees angle of incidence is decreasing as the foil approaches the surface.

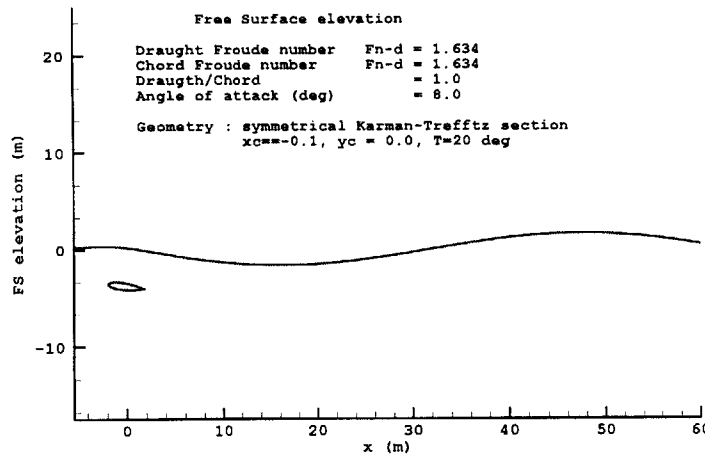


Figure 28: Free surface elevation at draft Froude No 1.634

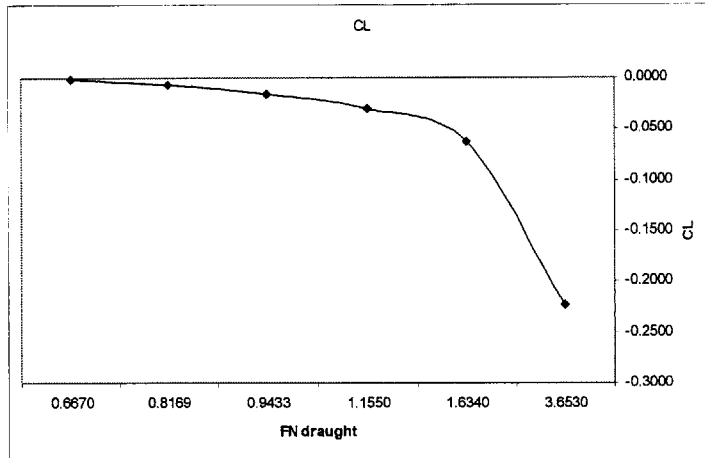


Figure 29: Lift coefficient for varying draft Froude number

1.4.d. Incident Waves

Flow simulation with incident waves is presented in this subsection. An incident wave system of plane progressive waves is implemented in the code. Up to 35 different waves can be superimposed, with the user specifying each wave's period and amplitude. Since the code is meant to be used as an investigation tool for the foil-borne craft's active control in stochastic seas, the phase of each wave can also be specified – a stochastic wave system built from a known spectrum will use a randomly distributed phase angle for each component of the spectrum as a random variable.

Wave Diffraction by a stationary circular cylinder

Theory (see Wehausen and Laitone [3]) states that a two-dimensional circular cylinder on which a plane monochromatic wave is incident will not reflect any energy and will only effect a phase shift on the diffracted ambient wave pattern.

This flow is simulated below. The diffraction wave elevation resulting from an incident monochromatic wave of unit amplitude from the left, on a circle lying at draft/diameter = 2.0, diameter/ λ = 0.01382 can be seen in Figure 30 (the incident wave is not shown in this figure). It is evident that a very small amount of energy is reflected in this simulation – this 'error' wave elevation however is of amplitude less than 0.5% of the incident wave amplitude. To the right of the body we can see the diffraction wave pattern which has as an effect the shift phase in the total wave elevation.

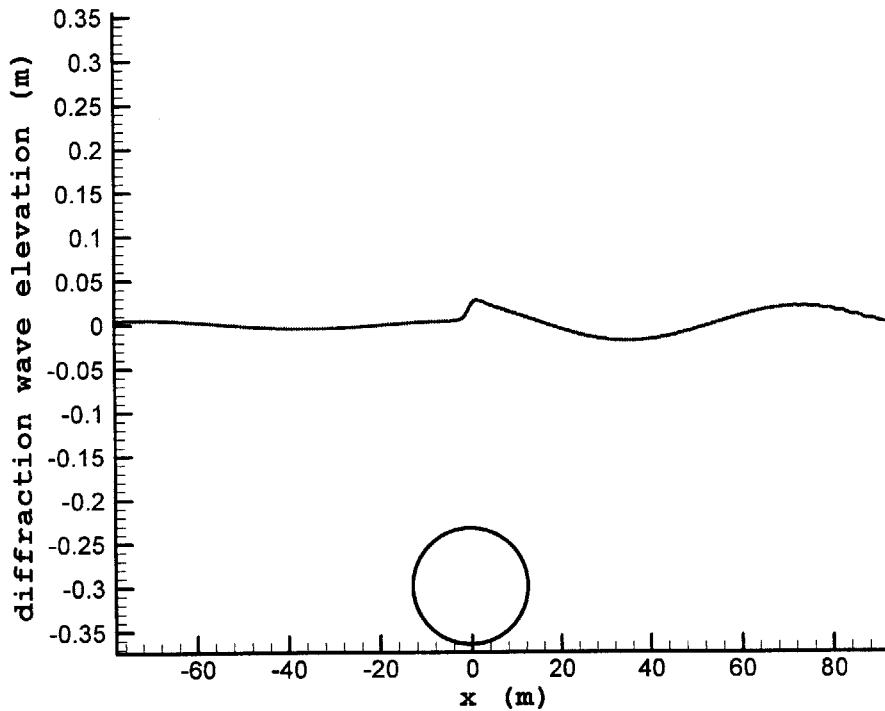


Figure 30: Diffraction component of free surface elevation by a 2D circular cylinder (Incident plane progressive wave of unit amplitude from the left – cylinder position and diameter not to scale)

1.4.e. Free Motions

In this subsection the code's convergence characteristics in free motion simulations are investigated. A motion control system is not yet included and some artificial restoring is used in order to provide stability of solution.

Spatial convergence

This experiment is a numerical check for body panel density convergence in heave mode free motion simulation. As in the physical validations that follow, an artificial restoring force is introduced since there is no natural restoring for a submerged hydrofoil in heave mode of motion. The foil is started from rest at a zero angle of attack. A plane monochromatic wave of unit amplitude is incident. No weight force is included in the simulation. Hence, the foil is expected to oscillate in heave forced by the sinusoidal lift force induced by the incident wave. The number of body panels was used as a convergence parameter, while the free surface panel Froude number was kept fixed to 2.83. Spatial convergence is displayed in Figure 31.

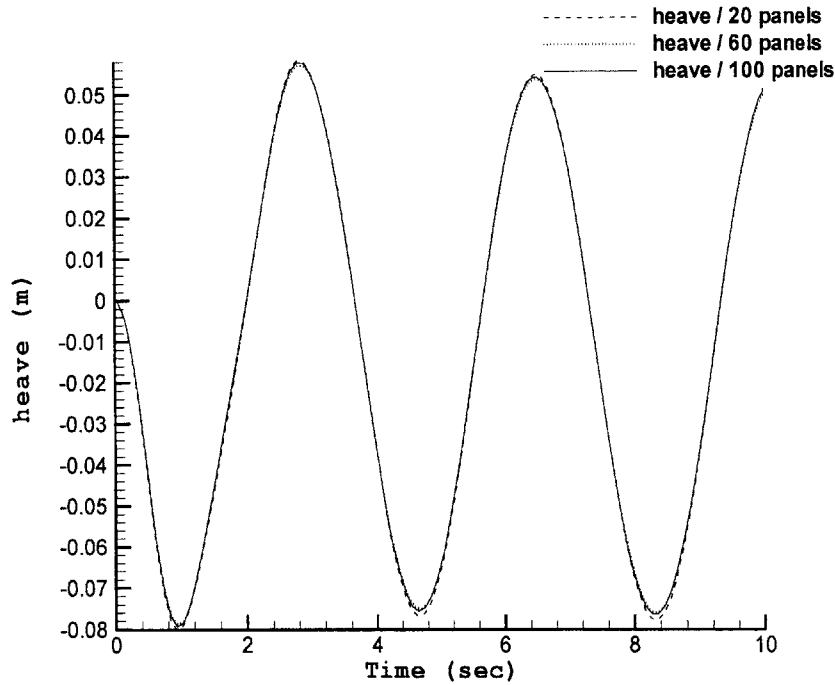


Figure 31: Panel Density convergence for heave mode free motion

Temporal Convergence

Temporal convergence (timestep size convergence) is tested for free motion in pitch mode. The parameter varied is the timestep length (and accordingly the length of the wake panel), expressed by the non-dimensional timestep β :

$$\beta = \frac{\sqrt{h/g}}{\Delta t},$$

where h is the free surface panel length and Δt the timestep length (larger β signifies a finer timestep).

If the timestep is set too coarse ($\beta < 2$) the solution does not converge. However when using finer timestep lengths, it is found that the solution is not very sensitive to the parameter β as can be seen in Figure 32

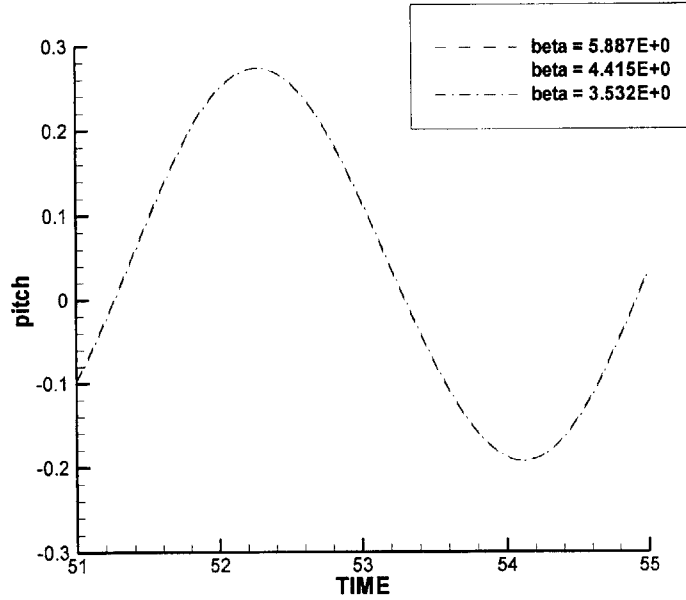


Figure 32: Temporal convergence for heave mode free motion

Heave response – resonance

The following experiment has a qualitative physical sense. The body is allowed to move only in heave mode, so we have a single degree of freedom dynamic system. **Artificial heave restoring** is included as in the previous experiments, in lieu of a motion control system which would be used in practice.

A plane progressive wave of unit amplitude is incident. The incident wave induces a time harmonic excitation force on the foil, which is operating at a zero mean angle of incidence. Using long-wavelength approximation, this harmonic excitation can be seen as the effect of the harmonic variation of the effective angle of attack on the foil:

$$\alpha_{\text{eff}} = \text{Arc tan} \left\{ \frac{\partial \phi_1 / \partial z}{U + \partial \phi_1 / \partial x} \right\}$$

where ϕ_1 the incident wave potential, whose spatial derivatives are calculated at the mean position of the foil midchord.

The physical problem now essentially reduces to a simple spring-and-mass dynamic system that is harmonically excited. The system's resonant frequency can be calculated (see for example Faltinsen [31]):

$$\omega_{\text{RES}} = \sqrt{\frac{C_{33}}{M + a_{33}}}$$

Here, C_{33} is the artificial heave restoring coefficient introduced in place of a motion control system. The weak point in this estimation is the added mass a_{33} approximation. In the following calculations the added mass value calculated by the local flow solution is used.

U (foil velocity)	10.00	m/sec
C_{33} restoring coefficient	1×10^6	N/m
Mass	5000.00	kg/m
a_{33} added mass	35949.30	kg/m
ω_{RES} theoretical encounter resonant frequency	4.94	rad/sec
$\omega_{0 RES}$ theoretical absolute resonant frequency	1.77	rad/sec
T theoretical absolute resonant period	3.56	sec

Table 4

Note in Table 4 that the body mass is not its displacement, but an arbitrarily introduced number that expresses the weight of an imaginary vessel supported by the foil and moving with it as a rigid body.

The heave response amplitude operator (RAO) was measured for various incident wave periods and a wave amplitude of one meter. The results can be seen in Figure 33. Indeed, the maximum response occurs near the theoretical resonance period of 3.56 seconds.

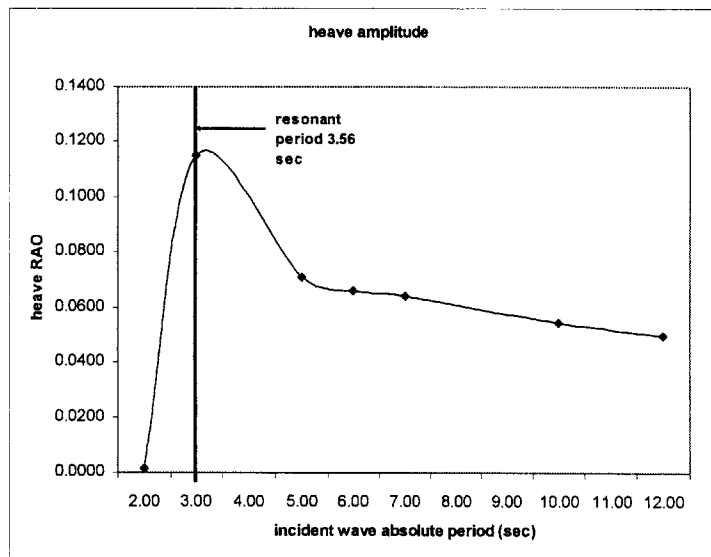


Figure 33: Heave response for varying frequency

A short look at the time histories of the lift force and heave displacement is also interesting. Near resonance, as we can see in Figure 34, the heave motion's phase is about 90 degrees behind the lift excitation force. In the larger period of 12 seconds (Figure 35), force and motion have nearly the same phase.

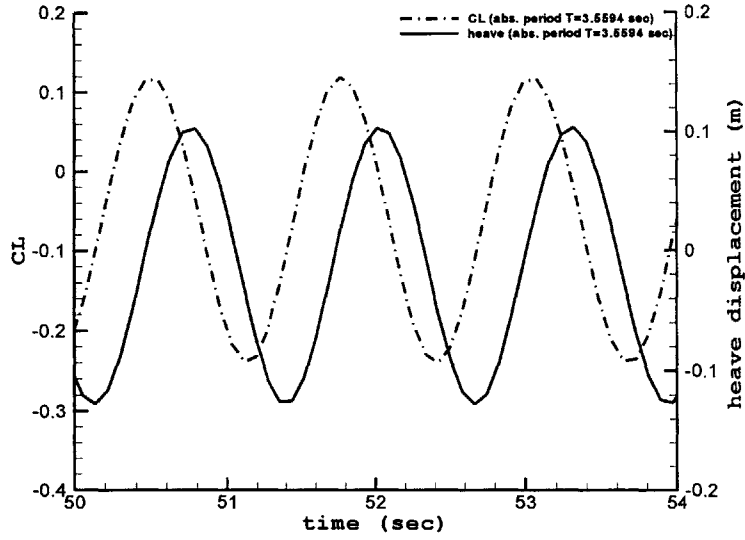


Figure 34: Lift coefficient and heave displacement time histories at $T=3.66$ sec

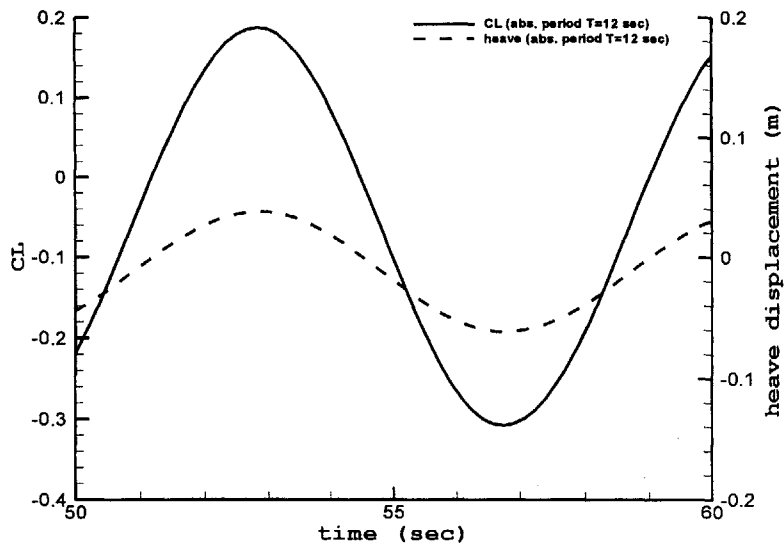


Figure 35: Lift coefficient and heave displacement time histories at $T=12.00$ sec

1.5. Motion-induced force coefficients and excitation forces on submerged hydrofoils

The hydrodynamics of submerged lifting hydrofoils form the main subject of this section. In the first part, the effect of draft and frequency on the heave motion-induced force coefficients of a submerged lifting hydrofoil is investigated through a set of numerical experiments. In the second part, the ambient wave excitation forces on the foil are approximated by a simple linear model.

1.5.a. Motion-induced force coefficients of a submerged hydrofoil

The rigid-body dynamics of a lifting foil operating near the free surface in free motion make a very interesting problem, since two kinds of hydrodynamic memory effects coexist: the ‘wake’ memory and the wave flow memory.

The wake memory is due to the fact that when the foil moves, in heave for example, while advancing with steady forward velocity, the circulation around and hence the lift force changes. As a result, the amount of vorticity shed in the trailing wake changes. Since the flow around the foil is affected by the distribution vorticity in its wake, the foil’s past history of motion affects the flow around it through the variable wake vorticity distribution.

The wave flow memory is due to the wave field radiated due to the foil’s motion, since waves radiated by the foil a finite length of time ago induce forces on it at the present time.

Theoretical lift force on heaving hydrofoil in infinite flow

Consider a thin, symmetric (flat) two-dimensional hydrofoil at zero steady angle of attack which performs an oscillatory heave motion with frequency ω and amplitude ξ_0 :

$$(1.6) \quad \xi_3(t) = \text{Re}\{\xi_0 e^{i\omega t}\}$$

while advancing with steady forward velocity U . The foil has a chord length of 2, and we can define the reduced frequency k of the heave motion:

$$(1.7) \quad k = \frac{\omega}{U}$$

which quantifies the time ‘unsteadiness’ of the motion. If we define the Theodorsen function:

$$(1.8) \quad C(k) = \frac{H_1^{(2)}(k)}{H_1^{(2)}(k) + iH_0^{(2)}(k)}$$

where $H_0^{(2)}$ and $H_1^{(2)}$ are Hankel functions of the second kind. A plot of the real and imaginary parts of $C(k)$ is shown on Figure 36. This function expresses the wake memory effect through the frequency-dependent force coefficients. Indeed, if we assume an infinitely

thin foil in ideal fluid flow, the time- and frequency-dependent lift force on the foil is (see Newman [1]):

$$(1.9) \quad L(t) = -2\pi\rho U^2 \operatorname{Re}\{C(k)ik\xi_0 e^{i\omega t}\} - \pi\rho\ddot{\xi}$$

We can note here that the second term on the right hand side clearly expresses the added-mass of a non-lifting flat plate in two-dimensional flow.

Since the heave acceleration is:

$$(1.10) \quad \ddot{\xi}_3(t) = \operatorname{Re}\{-\omega^2 \xi_0 e^{i\omega t}\}$$

equation (1.9) can be written:

$$(1.11) \quad L(t) = \operatorname{Re}\{(-2\pi\rho U^2 C(k)ik\xi_0 + \pi\rho\xi_0\omega^2)e^{i\omega t}\}$$

Since the foil has a flat camber line and a zero steady angle of attack, the time-steady lift force is zero, and the force in (1.11) is induced by the heave motion (indeed if we let $\xi_0=0$ then $L(t)=0$). Assuming relatively small heave amplitude ξ_0 , we linearize this motion-induced lift force L around the zero-heave position and write it in a form:

$$(1.12) \quad \begin{aligned} A_{33}\ddot{\xi}_3 + B_{33}\dot{\xi}_3 &= \operatorname{Re}\{(2\pi\rho U^2 C(k)ik\xi_0 - \pi\rho\xi_0\omega^2)e^{i\omega t}\} \Rightarrow \\ A_{33} \operatorname{Re}\{-\omega^2 \xi_0 e^{i\omega t}\} + B_{33} \operatorname{Re}\{i\omega \xi_0 e^{i\omega t}\} &= \operatorname{Re}\{(-2\pi\rho U^2 C(k)ik\xi_0 + \pi\rho\xi_0\omega^2)e^{i\omega t}\} \end{aligned}$$

where A_{33} and B_{33} are motion-induced force coefficients in infinite flow for small-amplitude oscillatory heave motion, analogous to the added-mass and damping coefficients. Separating real and imaginary parts on (1.12), we get the theoretical infinite-fluid force coefficients:

$$(1.13) \quad \begin{aligned} A_{33} &= \pi\rho\left(\frac{2}{k}\operatorname{Im}(C(k)) + 1\right) \\ B_{33} &= 2\pi\rho U \operatorname{Re}(C(k)) \end{aligned}$$

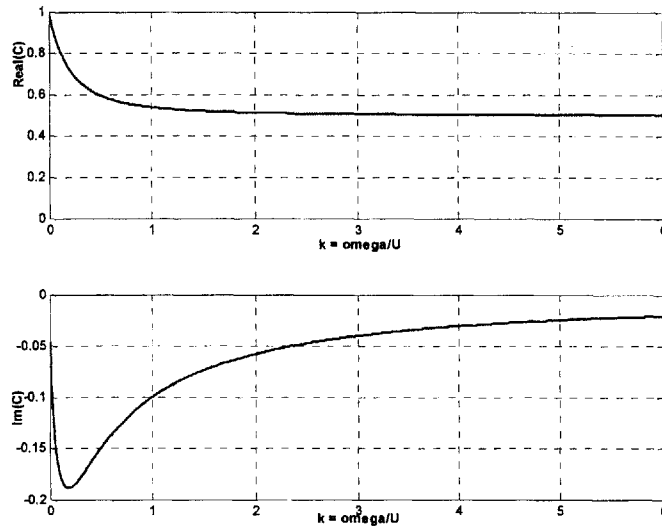


Figure 36: Real and Imaginary Parts of Theodorsen function $C(k)$

As we can see in Figure 36, the imaginary part of C is negative. Hence the first term in the parenthesis of the acceleration-dependent force formula (first formula of (1.13)) which expresses the ‘lifting’ component of the acceleration-dependent force is negative, while the second term which expresses the ‘flat-plate added mass’ component is positive. As we will see next the lifting component in certain cases outweighs the flat plate component resulting in a negative heave acceleration-dependent force coefficient, which means that the lift force is closer than 90° in phase with the heave motion.

On the contrary, the second coefficient B_{33} only has a ‘lifting’ component which assumes positive values (since $\text{Re}(C(k)) > 0$), and the resulting damping force can be seen as an expression of the energy shed in the wake by the heaving foil.

The force coefficients in equation (1.13) are plotted in Figure 37.

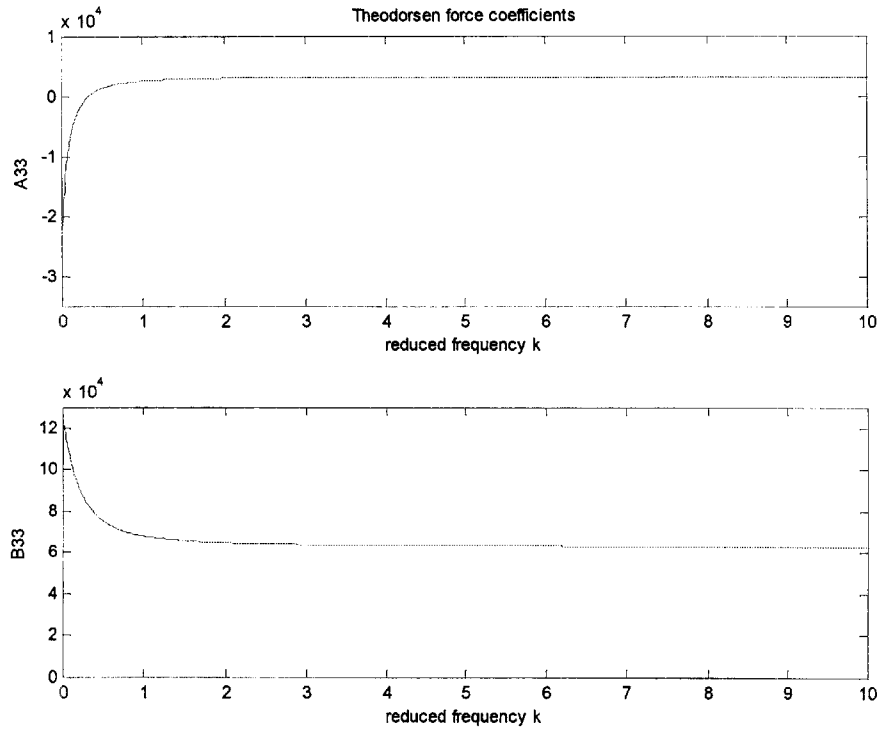


Figure 37: Theodorsen force coefficients

Variation of heaving hydrofoil motion-induced force coefficients with draft Froude number

Here the effect of the free surface wave flow on the motion-induced force coefficients of a heaving hydrofoil is investigated through a set of numerical experiments. The non-dimensional parameter describing each case is the draft Froude number reminded here to be

$$F_{nD} = \frac{U}{\sqrt{\text{Draft} \cdot g}}$$

The following experiments were carried out using the flat Karman-Trefftz foil from the preceding convergence tests at zero angle of attack in order to relate with the theoretical expectations from the previous paragraph. Simulations were run starting at a near-zero draft Froude number (very deep draft equivalent to an infinite flow) and subsequently draft Froude number was decreased until the foil was near the free surface. A chord length of 2.0 was used in order to conform with the definition (1.7) of the reduced frequency. Circular frequency was chosen at $\omega=0.80$ rad/sec and forward velocity at $U=20$ m/sec, resulting in $k=0.04$. The circular frequency was selected to be near the peak frequency of the Pierson-Moskowitz ocean wave spectrum for wind speeds around 20 -30 knots.

The motion-induced force coefficient values with varying draft Froude number are shown in Figure 36 and Figure 38 respectively. The magnitude of both coefficients decreases with decreasing draft. In this case this could mean that wake memory effects are being offset by wave memory effects as the foil approaches the free surface. The resulting free surface elevation created by the hydrofoil's wake is shown in Figure 40 for three draft Froude numbers – the increasing amplitude of the radiated wave as the foil approaches the free surface is apparent. Simulations were carried out up to a Froude number of 4.5 – above this Froude number draft becomes too shallow for accurate numerical calculation.

There is a difference in the order of 25% for the inertial and 11% for the damping coefficient, from the theoretical values predicted by formula (1.13) of the previous paragraph using Theodorsen theory. Part of this difference can be attributed to the fact that the theoretical prediction is for a foil with zero thickness while the simulations were run using a foil of finite thickness.

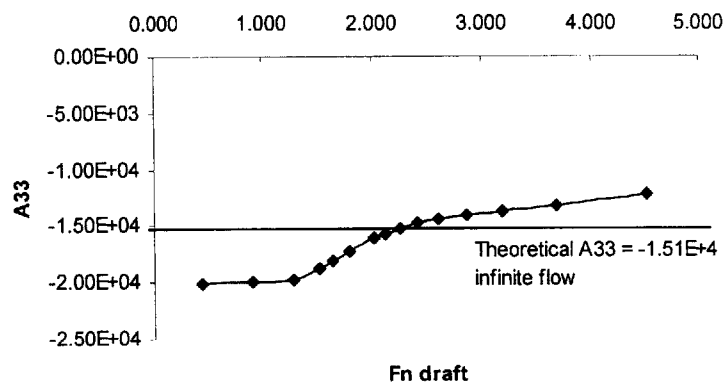


Figure 38: A₃₃ coefficient variation with draft Froude number at $k=0.04$ reduced frequency

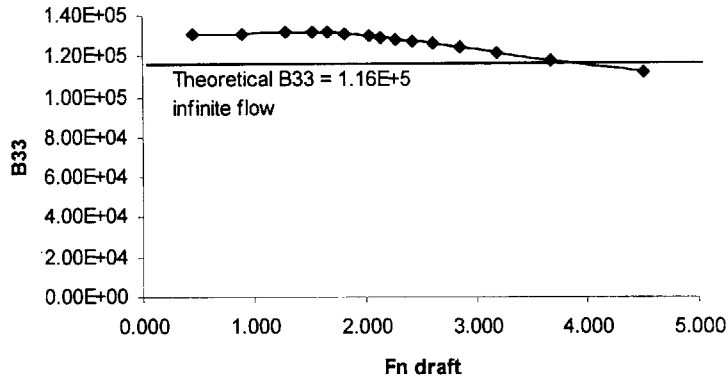


Figure 39: B_{33} coefficient variation with draft Froude number at $k=0.04$ reduced frequency

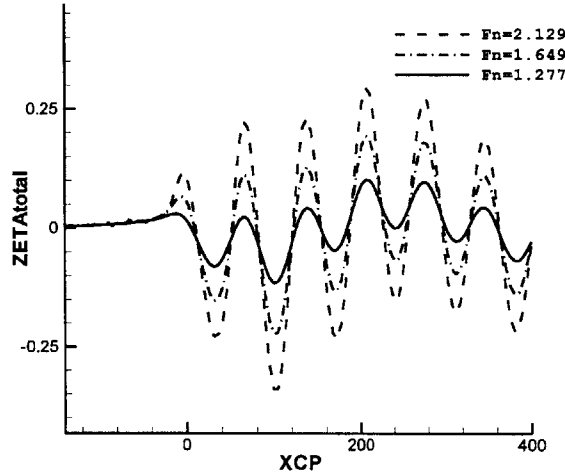


Figure 40: Free surface elevation with varying draft Froude number

Variation of heaving hydrofoil motion-induced force coefficients with frequency at a fixed draft

In this subsection the variation of motion-induced force coefficients in heave for the same hydrofoil geometry is investigated. Numerical experiments are carried out for a draft Froude number of 3.50.

Results for added the A_{33} and B_{33} coefficients are presented in Figure 41 and Figure 42 respectively. The coefficient A_{33} starts out at low frequencies with high negative values as was the case in the previous paragraph and gradually increases towards the positive infinite frequency limit of Theodorsen’s theoretical prediction for A_{33} coefficient which can be seen in Figure 37. Since Theodorsen’s prediction is for an infinite fluid flow, we can deduce here that at high frequencies the free surface effects on the motion induced force for a lifting foil

become negligible. A similar behavior is displayed by the B_{33} coefficient (Figure 42) which tends asymptotically to the infinite-frequency limit predicted by Theodorsen (Figure 37).

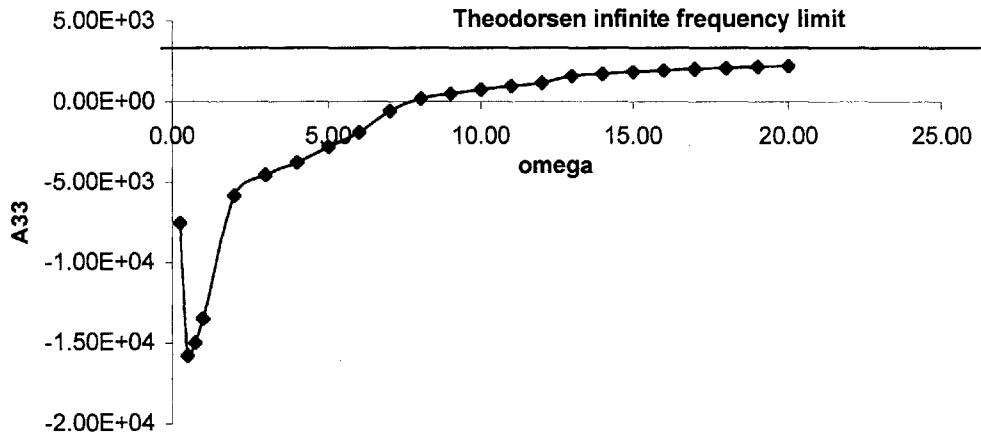


Figure 41: A_{33} coefficient variation with frequency for F_n draft=3.50

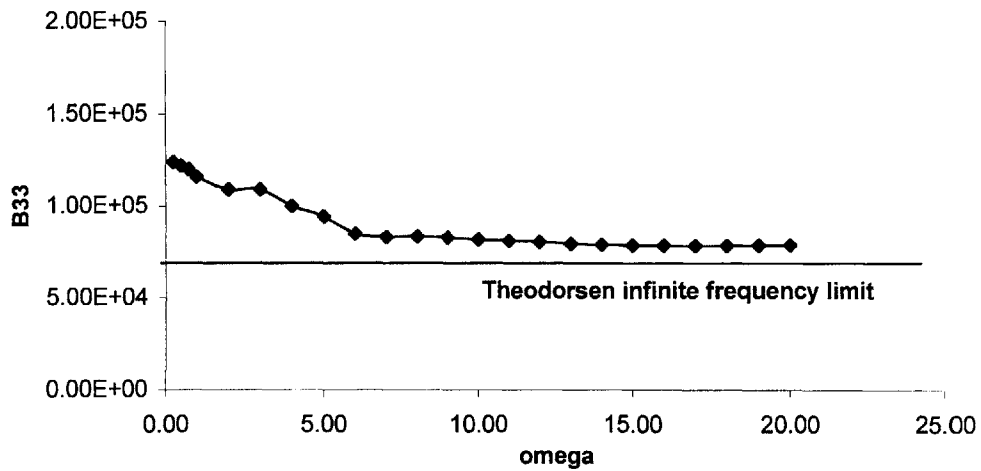


Figure 42: B_{33} coefficient variation with frequency for F_n draft=3.50

The Theodorsen infinite frequency limits are very close to the impulsive added mass and damping limits a_{033} and b_{033} calculated for the hydrofoil, which shows that the free surface does not have a very strong effect in this particular problem. The values of a_{033} and b_{033} are calculated from the solution of the ‘local flow’ boundary value problem with zero potential on the free surface ($\varphi=0$ plane). Following Kring [2], for the special case of two-dimensional heave motion, this problem for the local heave motion-induced potential N_3 can be stated:

$$(1.14) \quad \begin{cases} N_3 = 0, z = 0 \\ \nabla^2 N_3 = 0, \text{ everywhere} \\ \frac{\partial N_3}{\partial n} = n_z, \text{ on } S_B \text{ body surface} \\ N_3 = 0, \text{ on } S_{FAR} \quad |x| \rightarrow \infty \end{cases}$$

where n_z is the z-component of the unit vector normal to the body surface and,

$$(1.15) \quad \begin{aligned} a_{033} &= \rho \int_{S_B} N_3 n_z ds \\ b_{033} &= \rho \int_{S_B} -\vec{U} \cdot \nabla N_3 n_z ds \end{aligned}$$

Then a_{033} and b_{033} can be considered to be the infinite-frequency limits of the added mass and damping coefficients. Their values will also be used later for the creation of linear state-space models for hydrofoil craft.

15.b. A simple model for the ambient wave excitation force on a submerged hydrofoil

A submerged hydrofoil advancing in ambient waves is subject to a total excitation force made up by various components. The phenomenon itself is in truth very complicated with the total force determined by wave, friction, vortex and separation drag, large lift variations due to changing ambient flow field and lift breakdown due to cavitation or even ventilation.

In this paragraph, a simplified two-dimensional linear model for the estimation of the heave excitation force due to ambient waves is presented. If we disregard effects of viscosity, cavitation and ventilation, the main effect of an incident wave on the foil is a change in the ambient flow field due to the wave-induced velocity. The model proposed here uses the wave-induced velocity, with the aid of long-wavelength approximation and lift-coefficient linearity at small angles of attack, to estimate the wave heave excitation force.

It must be noted here that the potential-flow code developed in the present work provides a more accurate estimation of ambient wave excitation forces on the hydrofoil (through the solution of the linearized boundary value problem) than the model proposed in this section. However this model can provide useful insight and estimations without requiring the numerical solution of the BVP.

Effective angle of attack and wave-induced lift coefficient

Assume a hydrofoil is advancing with steady velocity U in an ambient wave which induces vertical and horizontal velocities w and u , as in the sketch of Figure 43. Most hydrofoil ships have chord lengths in the order of 2-5 meters, while ambient ocean wavelengths are in the order of 50 meters or more. Hence we can use a long wavelength

approximation and assume that the wave-induced velocity at the middle of the foil is roughly the same throughout the whole chord length.

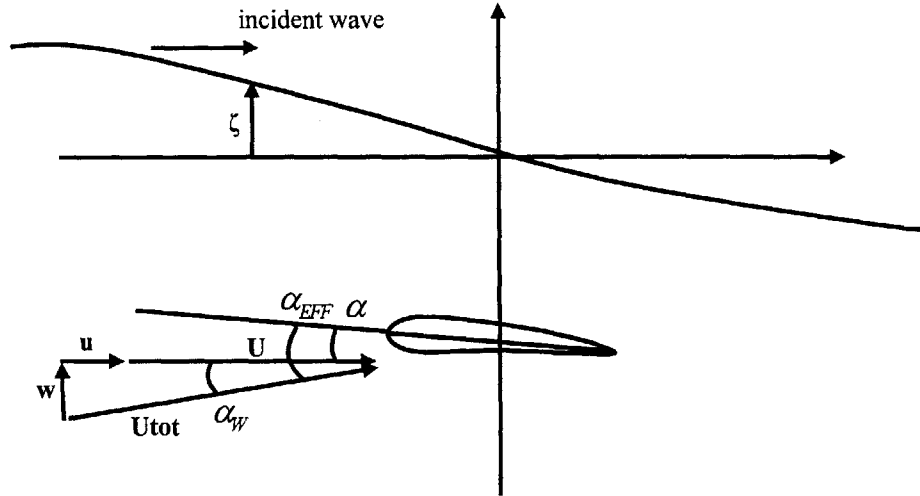


Figure 43: Effective angle of attack

We wish to estimate the unsteady heave exciting force F_3 . For small total angles of attack α_{tot} , F_3 can be assumed to be in the direction of the foil lift force. The total lift force L_{TOT} at time t is:

$$(1.16) \quad L_{TOT} = \frac{1}{2} C_{L_{TOT}} \rho C U_{TOT}^2$$

where C is the foil chord, U_{TOT} the total ambient velocity as in the sketch of Figure 43, $C_{L_{TOT}}$ is the total lift coefficient and ρ the water density.

The wave induced velocities u and w are usually small compared to the foil speed which is in the order of 40 knots. Hence, we can approximate the magnitude of the total velocity U_{TOT} by the magnitude of the foil velocity U :

$$(1.17) \quad U_{TOT}^2 = (U + u)^2 + w^2 \cong U^2$$

hence,

$$(1.18) \quad L_{TOT} \cong \frac{1}{2} C_{L_{TOT}} \rho C U^2$$

For relatively small total angles of attack (less than 12-15°), we can estimate the total lift coefficient assuming it varies linearly with the angle of attack.

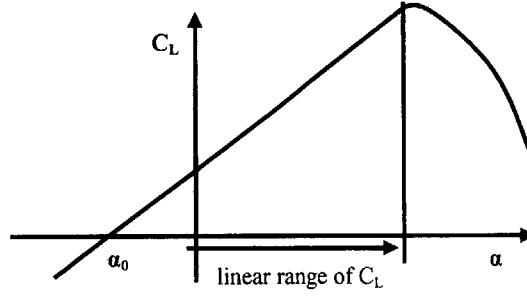


Figure 44: Lift coefficient at small angles of attack

Referring to the sketch of Figure 44, for small angles of attack we can write:

$$(1.19) \quad C_{L_{TOT}} \cong \frac{dC_L}{d\alpha} (a_{EFF} - a_0)$$

where α_0 is the angle of zero-lift. For example, if we have a flat plate where $\alpha_0=0$ and the slope of lift coefficient is 2π , the above relation gives a lift coefficient of $2\pi\alpha_{EFF}$.

The effective angle of attack, as in the sketch of Figure 43, is the sum of the steady angle α and the wave-induced angle α_w . Hence, we can write:

$$(1.20) \quad \begin{aligned} C_{L_{TOT}} &\cong \frac{dC_L}{d\alpha} (a_{EFF} - a_0) \\ &= \frac{dC_L}{d\alpha} ((a_w + \alpha) - a_0) = \frac{dC_L}{d\alpha} a_w + \frac{dC_L}{d\alpha} (\alpha - a_0) \\ &= C_{LW} + C_{LST} \end{aligned}$$

Hence the total lift coefficient is composed by a steady part C_{LST} and a wave-induced part C_{LW} . The steady part is time constant since it only depends on the foil geometry, while the second part is a function of time since the wave-induced velocity and angle of attack are varying in time. Hence:

$$(1.21) \quad C_{L_{TOT}}(t) = C_{LW}(t) + C_{LST}$$

At this point we can further approximate the wave-induced lift coefficient using the wave-induced velocity (refer to the sketch of Figure 43 as well):

$$(1.22) \quad C_{LW}(t) = \frac{dC_L}{d\alpha} a_w(t), \text{ and } \alpha_w(t) \cong \text{Arc tan}\left(\frac{w(t)}{U}\right) \cong \frac{w(t)}{U} \text{ for small } \frac{w(t)}{U}$$

hence,

$$(1.23) \quad C_{LW}(t) \cong \frac{dC_L}{d\alpha} \frac{w(t)}{U}$$

Heave excitation force

Using the previous analysis, we can break the total lift force into a steady and an unsteady wave-induced component:

$$\begin{aligned}
 L_{TOT}(t) &= \frac{1}{2} C_{LTOT} \rho C U^2 \\
 (1.24) \quad &= \frac{1}{2} C_{LW}(t) \rho C U^2 + \frac{1}{2} C_{LST} \rho C U^2 \\
 &= L_W(t) + L_{ST}(t)
 \end{aligned}$$

As noted before, the wave-induced unsteady heave excitation force can be approximated from the unsteady part of the total lift force:

$$(1.25) \quad F_{3W}(t) = L_W(t) = \frac{1}{2} C_{LW}(t) \rho C U^2$$

and using (1.23),

$$\begin{aligned}
 (1.26) \quad F_{3W}(t) &= \frac{1}{2} \frac{dC_L}{d\alpha} \frac{w(t)}{U} \rho C U^2 \\
 &= \frac{1}{2} \frac{dC_L}{d\alpha} \rho C U w(t)
 \end{aligned}$$

Equation (1.26) gives the estimation of the wave-induced heave exciting force on a submerged hydrofoil. The lift coefficient slope can be calculated using linear theory (in the case of simple forms) or experiments in the case of arbitrary-form foil sections. For example, if the foil is a flat plate with lift coefficient slope $2\pi\alpha$, equation (1.26) gives:

$$(1.27) \quad F_{3W}(t) = \pi \rho C U w(t) \text{ (flat plate)}$$

Phase Shift

It was seen in the unsteady flow tests that an oscillating lifting flow includes a phase shift which depends on frequency. This phase shift is described analytically by Theodorsen's theory (see previous subsection).

Initial experiments with the linear model (1.26) showed that while force amplitude prediction is satisfactory, there is a frequency-dependent phase shift in the oscillating wave-induced force which is not predicted by the model. This phase shift physically resembles the Theodorsen phase shift in for a harmonically oscillating lifting foil, with the difference that in our case the flow, not the foil, is oscillating. In lack of a better approximation, we will use the Theodorsen phase shift prediction in order to enhance the phase accuracy of this model.

From equation (1.9) we can deduce the phase ϕ of the lift force with respect to the negative $\pi/2$ zero-frequency phase:

$$(1.28) \quad \phi = -\frac{\pi}{2} + \text{Arc tan}\left(\frac{-\text{Re}(C(k))}{\text{Im}(C(k))}\right)$$

It must be noted here that the reduced frequency k is defined through the hydrofoil encounter frequency with the ambient waves:

$$(1.29) \quad \omega_e = \omega - U \frac{\omega^2}{g}$$

$$k = \frac{\omega_e}{U}$$

Then, the predicted lift force will have a time lag t_0 due to this phase shift, and we have:

$$(1.30) \quad F_{3w}(t) = \frac{1}{2} \frac{dC_L}{d\alpha} \rho C U w(t-t_0), \quad t_0 = \phi / \omega_e$$

The linear model (1.30) can be used for the estimation of the heave excitation force in ambient wave of relatively small amplitude, so that the assumptions of (1.17) and (1.23) hold. Hence, from (1.30) it is obvious that a real-time estimate of the wave induced vertical velocity is needed for the estimation of the instantaneous heave excitation force. In numerical simulations with plane progressive wave this estimate is available from linear theory. In physical applications however the only available measurement will most probably be a free-surface elevation measurement using a probe or forward-looking radar. In that case an estimate of the wave-induced vertical velocity needs to be derived from the knowledge of free surface elevation.

Model Tests

In order to validate this linear model a set of simulations was run using the same symmetrical foil as in the added mass tests of the previous subsection, at a draft Froude number of 3.5. During each simulation a sinusoidal monochromatic wave of unit amplitude was incident on the fixed hydrofoil. The heave exciting force calculated by the code was stored and plotted against the linear model (1.30) prediction. Here results are presented for three incident wave frequencies of 0.5, 0.8 and 1.0 rad/sec, in Figure 45, Figure 46 and Figure 47 respectively.

The force amplitude prediction is quite satisfactory (error smaller than 9% in general) in all cases. In high frequency the model seems to fare better in terms of amplitude prediction. Phase has a slight error growing with frequency but phase prediction is much better than without the adjustment (1.30) where errors in the order of 30° appeared at high frequencies.

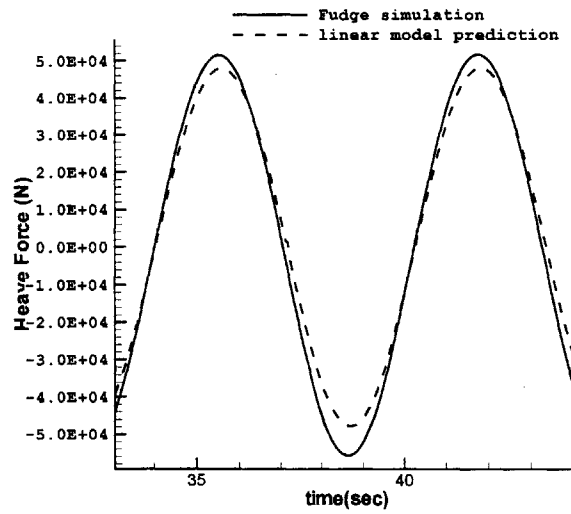


Figure 45: Heave excitation force in absolute wave period $T=12.56$ sec ($\omega=0.5$ rad/sec)

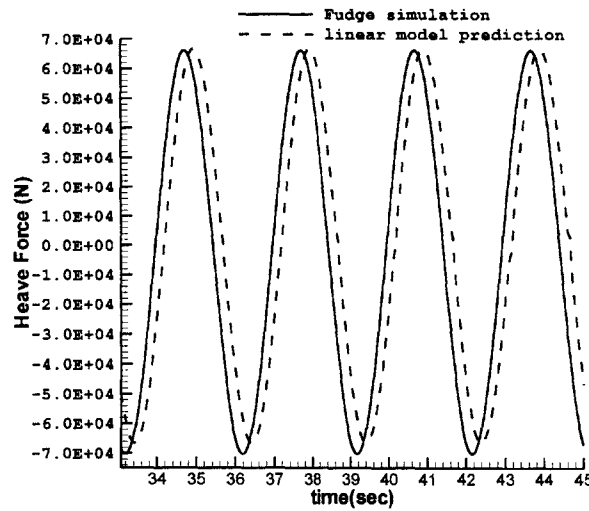


Figure 46: Heave excitation force in absolute wave period $T=7.85$ sec ($\omega=0.8$ rad/sec)

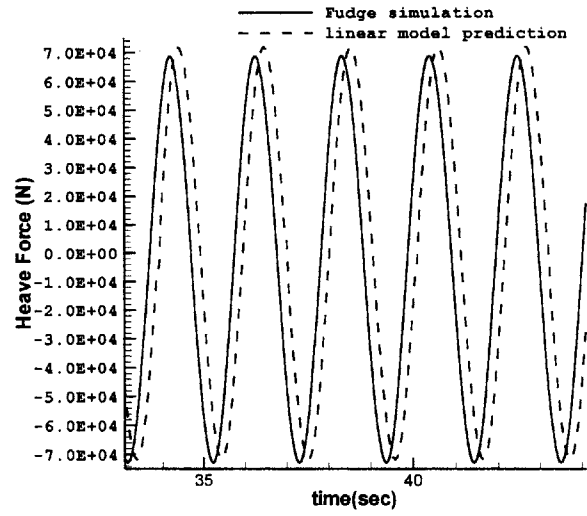


Figure 47: Heave excitation force in absolute wave period $T=6.28$ sec ($\omega=1.0$ rad/sec)

2. Motion Control

2.0 Introduction

In this section the motion control of marine vehicles and specifically hydrofoil ships is studied. The main objective is the reduction of the ship's motions due to ambient waves. The hydrodynamic force and motion solver developed in the first part of this work provides a useful and relatively accurate simulation tool which is used for the investigation of motion control methods.

Initially, a presentation of contemporary control methods is given. The similarity between the dynamics of hydrofoil ships and aircraft encourages the application of aircraft control methods to the current problem. Hence, a large part of the theory outlined is applied today to the design of control laws for aircraft. A basic presentation of classical control theory is given, and a more detailed discussion on state-space modern design and optimal control follows. The widely accepted technique of the Linear-Quadratic Regulator is presented along with its mathematical justification, since it will be used later on the problem of hydrofoil motion control treated in this work.

One of the most challenging aspects in the motion control of marine vehicles is modeling the seakeeping equations of motion, which express the free-surface dynamics of bodies operating on or near the free surface, in a linear time-invariant form that can be used for the design of control laws. The reason is that time-domain seakeeping equations of motion include memory effects which at first inspection cannot be explicitly included in a linear time-invariant model. In the second part of this section, an initial approach is investigated. A linear, time-invariant state-space model based on the vessel's impulsive dynamics is created, where memory effects are treated as external disturbances and hence disregarded in the design of control laws. Using this model, a motion controller is designed and tested based on the theory of the Linear-Quadratic Regulator, with very encouraging results. This approach follows the methodology applied in aircraft control.

2.1. Control Theory

This section includes a short outline of control methods and their application to aircraft and marine vehicles. Aircraft control is a very wide subject, ranging from optimal control theory, rigid body dynamics and aerodynamics on the theoretical side, to practical actuator and feedback control systems design. Here we will only attempt to review the basic tools from control theory that are used in aircraft and marine vehicle control today, starting from a brief presentation of classical design and continuing with modern state-space techniques, optimal control and the special but widely accepted method of the Linear-Quadratic Regulator.

Most high performance commercial and military aircraft today are aerodynamically unstable. This means that, for example, a small deviation from an equilibrium position by a roll angle ϕ will result in an augmentation of this deviation, if the body is left to respond uncontrolled. A simplified case is shown in Figure 48 where an aircraft with a negative dihedral angle d is inherently unstable in roll mode. A good example of such an aircraft is the 1950's fighter F-104.

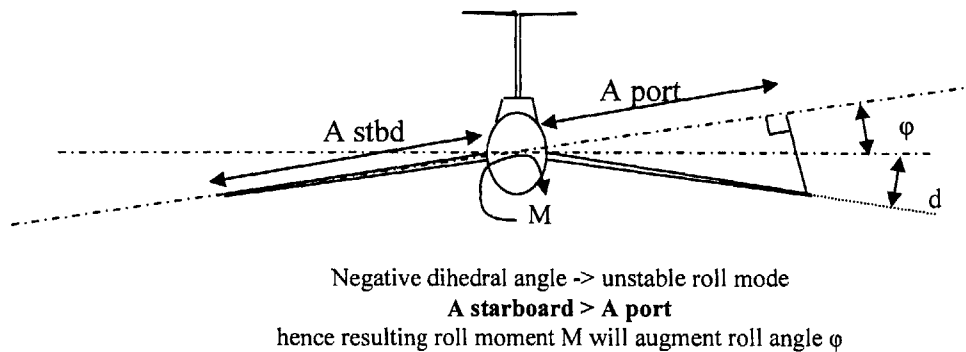


Figure 48: Airplane sketch – negative dihedral angle

A hydrofoil ship is hydrodynamically unstable in certain cases as well – an example can be seen in Figure 49, where instability arises from the coupling between the heave and pitch modes of motion. A bow-down pitch displacement by an angle ξ_5 results in a negative heave force F_3 on the foils due to negative angle of attack.

Hence, most modern aircraft would be impossible to fly without an automatic control system [7]. The same is true for most modern hydrofoil ships that utilize fully submerged foils, such as the one in the simplified sketch of Figure 49 (reproduced from the first part).

Instabilities such as these are treated in modern aircraft with the use of automatic control systems. Stability Augmentation Systems (SAS) and Control Augmentation Systems (CAS) are two examples; autopilots are another case of automatic control systems applied to aircraft.

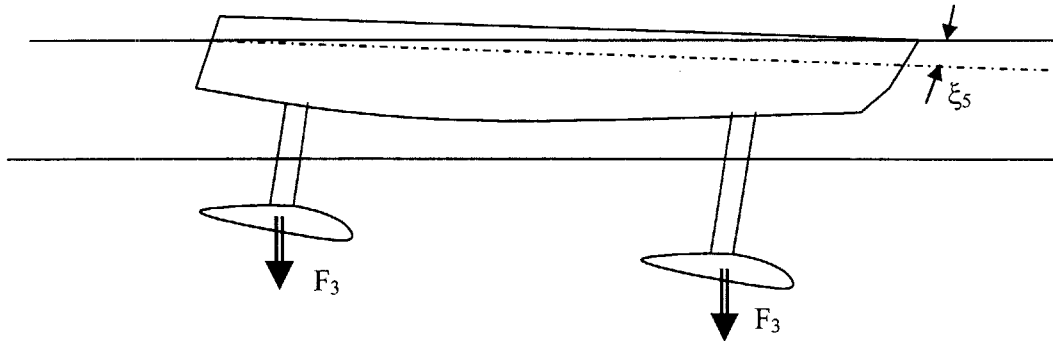


Figure 49: Hydrofoil ship unstable coupled heave and pitch mode

2.1.a. Classical Control System Design

The term *classical design* refers to a number of methods that have been used during the past century for the design of control systems. Classical design is applicable to single-input single-output systems and is based essentially on frequency-domain methods for shaping the system's loop gain (see below). The immediate objective of classical design is to ensure overall system stability, together with desirable response characteristics. In this subsection the basic structure and terminology used in classical design is presented.

A simplified feedback controlled system representation can be seen in Figure 50 [8]. The output is the controlled variable C . The output is measured by a feedback element H to produce the primary feedback signal B , which is then compared to the reference (command) input R . The difference E between the reference input R and the feedback signal B is the input to the controlled system G and is referred to as the actuating signal. The transfer functions of the forward and feedback components of the system are G and H , respectively.

In order to study such systems easily, it is very convenient to take the Laplace transform of the transfer functions. This is in part owed to the fact that most system transfer functions are solutions of differential equations in the time domain. Hence, in the following description we shall refer to variables and functions in terms of the transform variable s .

The equations describing this simplified system in terms of the transform variable are

$$\begin{aligned}
 (2.1) \quad & C(s) = G(s)E(s) \\
 & B(s) = H(s)C(s) \\
 & E(s) = R(s) - B(s)
 \end{aligned}$$

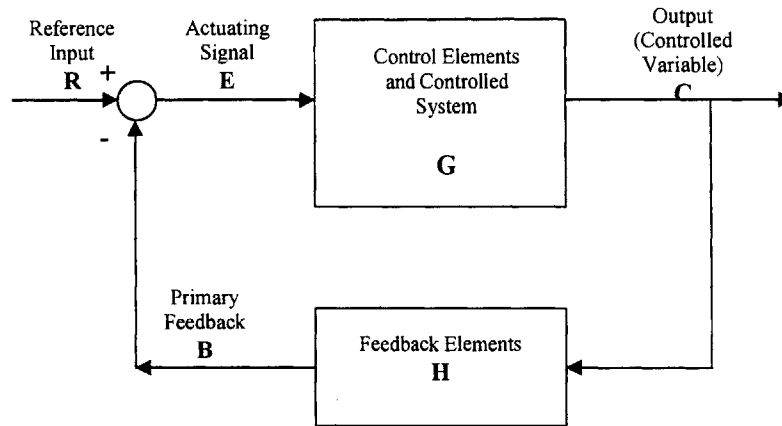


Figure 50: Feedback system (1)

Combining these equations gives the *overall transfer function* (also referred to as the *control ratio*)

$$(2.2) \quad \frac{C(s)}{R(s)} = \frac{G(s)}{1 + G(s)H(s)}$$

The characteristic equation of the system is obtained from the denominator of the overall transfer function

$$(2.3) \quad 1 + G(s)H(s) = 0$$

The characteristic equation has a very important role in the stability and response of the closed-loop system, since its roots give the poles of the overall system.

The *open-loop transfer function* or *loop gain* is defined as the ratio of the output of the feedback path $B(s)$ to the actuating signal $E(s)$

$$(2.4) \quad \frac{B(s)}{E(s)} = G(s)H(s)$$

A slightly more detailed description of a typical feedback system can be seen in Figure 51 [8]. This description can be directly referenced to a practical application. If we take, for example, an altitude-control regulator, then the controlled variable c would be the aircraft altitude. The disturbance d to the system could be the magnitude of a vertical wind gust. The control elements would then be the aircraft's elevators, and the manipulated variable M the elevator angle of attack. The controlled system transfer function G_2 is a black-box

representation of the aircraft dynamics – the aircraft equation of motion in the longitudinal plane, including the control surface dynamics, is hidden in the G_2 function.

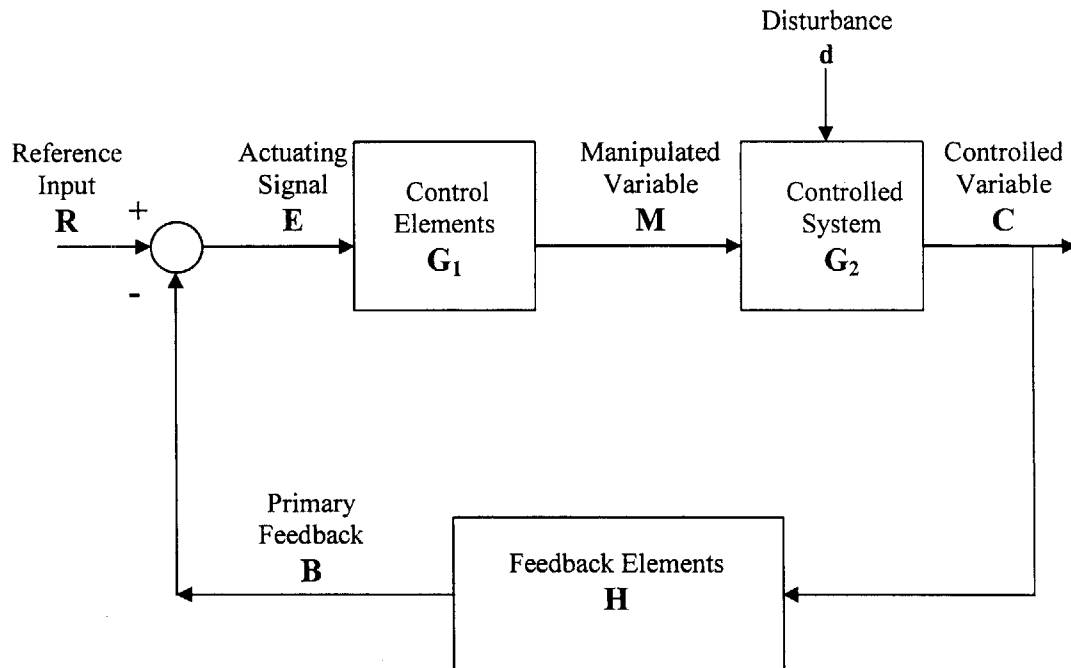


Figure 51: Feedback system (2)

The poles of the overall transfer function largely determine the behavior of the controlled system. Each pole describes a natural mode for the system. The sign of the real part of each pole determines whether the corresponding mode is stable or unstable. In order for the mode to be stable, its pole must have a negative real part (for a detailed analysis refer to [8]).

A particular method which is widely used in classical design is the root-locus. This method has been used since the 1940's in the design of most aircraft control systems. Although it is gradually ceasing to be directly applied, it is a basic design technique that still provides the controls system designer insight about the stability and behavior of the dynamical system.

The root-locus is a plot of the roots of the system's characteristic equation as a function of the gain of the open-loop transfer function. The effect of the open-loop gain becomes evident this way. The root-locus method, briefly, consists on adjusting the open-loop gain so that the system has the desirable stability characteristics. A root-locus plot for the pitch-rate Control Augmentation System of the F-16 combat aircraft is shown in Figure 52 [7].

The root locus can be carried out graphically – graphical design of control system characteristics has been carried out systematically until as late as the 1970's. It is, as most classical design techniques, a Single Input – Single Output (SISO) design method. In order to

design a control system for a complex, multivariable system (Multiple Input – Multiple Output, MIMO) using the root-locus method one would have to use an iterative procedure, closing one loop at a time [9]. A root locus must be plotted for each gain element (i.e. for each of the SISO transfer functions that consist the MIMO system), taking in account the gains previously selected. Due to factors such as the complexity of MIMO systems and the strong coupling between system elements, stability is not guaranteed.

It must be noted here that classical design, and control systems design in general, does not consist on the use of one particular method only. Problems are solved with a combination of numerous useful tools and techniques, and each technique provides information on different aspects of the plant and control dynamics. Classical design requires significant experience and intuition from the designer's part [9]. For a comprehensive presentation of classical (and modern) design methods used in practice today the reader is referred to Belanger [22].

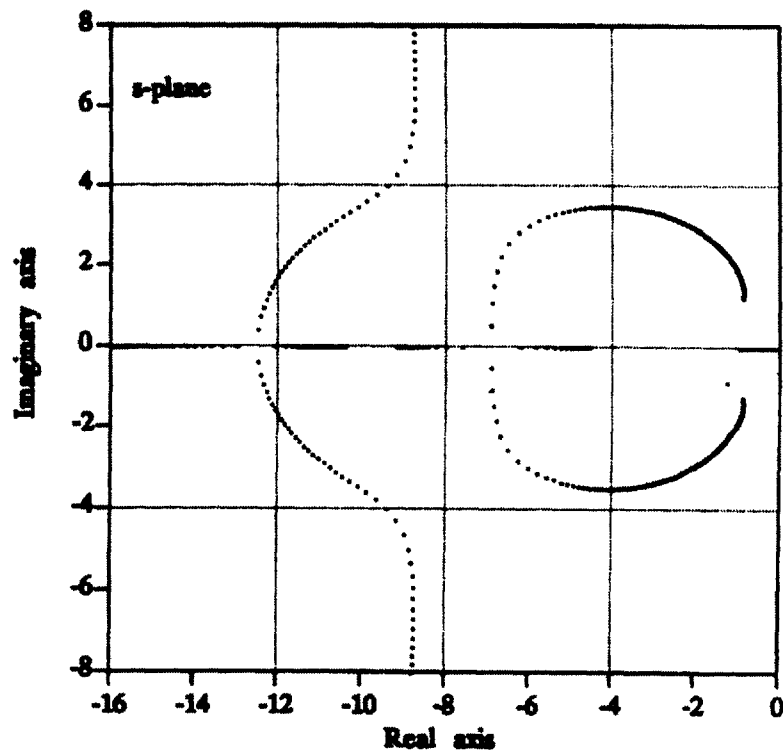


Figure 52: F16 aircraft root locus

2.1.b. Modern Control Systems Design - State Space Approach and Optimal Control

Modern control methods are fundamentally time-domain techniques. The heart of modern design methods is a time domain *state-space model* of the system to be controlled. The state-space model description of a system was initially introduced by Robert Kalman in

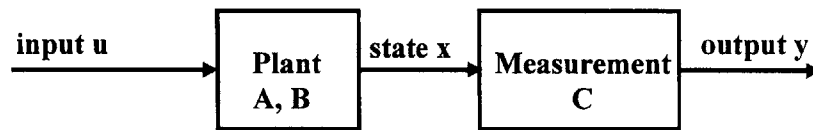
the late 1950's (see, for example, Stevens and Lewis [7]). It requires detailed knowledge of the system dynamics. A *linear, time-invariant state space model* has the form:

$$(2.5) \quad \begin{cases} \frac{dx}{dt} = Ax + Bu & \text{(state equation)} \\ y = Cx & \text{(measurement equation)} \end{cases}$$

In (2.5), $\mathbf{x}(t)$ is a vector of system variables, $\mathbf{u}(t)$ is a vector of control inputs and $\mathbf{y}(t)$ is a vector of measured outputs, from $t=0$ to a final time $t=T$.

Matrix A is called the system or plant matrix. This matrix models the dynamical behavior of the system – for example, in the case of a mechanical system it can contain inertial, damping and restoring terms. Matrix B is called the input matrix, and models the effect of the applied control vector \mathbf{u} to the time rate of change of the state vector. The \mathbf{x} state vector can contain any number of system variables - it selected so as to accurately describe the system's behavior. Here lies a significant advantage of modern control: it can handle multiple-input, multiple output systems as well as single-input, single-output ones, through the state-space description.

Equation (2.5) describes an *open-loop* system, essentially a linear time-invariant system (LTI system) for which the external control input u is not yet explicitly defined. A generic block diagram for equation (2.5) can be:



A *feedback control* can be defined by the control law form:

$$(2.6) \quad \mathbf{u} = -\mathbf{K}\mathbf{x}$$

where in this simple time-invariant case K is the feedback gain matrix. This form of control is called *state-variable feedback* since all system states (vector \mathbf{x}) are used to determine the control. The control input applied at each time instant is thus dictated by the current state of the system \mathbf{x} . Another form is the *output feedback control*

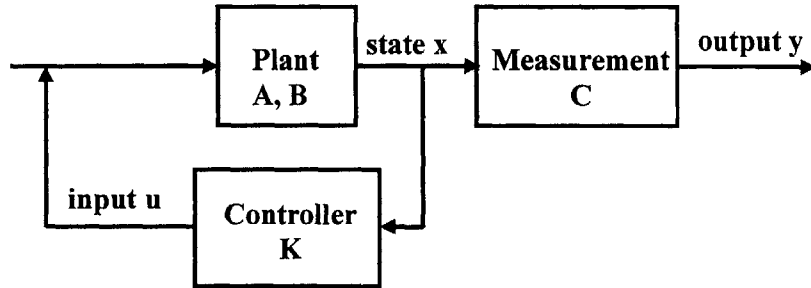
$$(2.7) \quad \mathbf{u} = -\mathbf{K}\mathbf{y}$$

where the output vector \mathbf{y} determines the control vector – this form of control can be used when real time information on the system state is unavailable. For example, if \mathbf{x} consists of the aircraft's pitch angle and pitch rate, it is possible that only pitch rate can be measured with adequate accuracy. A feedback control system can then be designed only on pitch rate information. This would consist a case of output-feedback design.

When the state-feedback control law (2.6) is used, the state space description of the system becomes:

$$(2.8) \quad \begin{aligned} \dot{x} &= Ax + Bu, \text{ with } u = -Kx \\ \text{hence } \dot{x} &= (A - BK)x \end{aligned}$$

Equation (2.8) describes the *closed-loop* system. The dynamical behavior of the system is now modeled by the closed-loop plant matrix $A - BK$. A simple block diagram for this system can be:



Relation between frequency domain and state-space descriptions of a system

An analogy exists between the state-space and classical frequency domain representations of a system through the definition of a matrix transfer function, which will be given here.

Starting from the state equation (2.5), we can take the Laplace transform (with zero initial state $x_0 = x(0) = 0$):

$$(2.9) \quad \begin{cases} sx(s) = Ax(s) + Bu(s) \\ y(s) = Cx(s) \end{cases} \Rightarrow \begin{cases} x(s) = (sI - A)^{-1}Bu(s) \\ y(s) = C(sI - A)^{-1}Bu(s) \end{cases}$$

where I is a unit n by n matrix. Let now

$$(2.10) \quad H(s) = C(sI - A)^{-1}B$$

Equations (2.9) and (2.10) give

$$(2.11) \quad \begin{aligned} y(s) &= H(s)u(s) \Rightarrow \\ \frac{y(s)}{u(s)} &= H(s) \end{aligned}$$

The analogy with the relation (2.2) is apparent (taking in account that here the input and output of the system are denoted u and y respectively). Matrix $H(s)$ is referred to as the matrix transfer function of a (possibly) multiple-input, multiple-output system (2.5). Moreover, from equation (2.10) we have

$$(2.12) \quad H(s) = \frac{C \cdot \text{adj}(sI - A) \cdot B}{\det(sI - A)}$$

and similarly, if a linear feedback control law such as the one in (2.6) is defined and the system has the closed-loop form (2.8), the matrix transfer function can be written

$$(2.13) \quad H(s) = \frac{C \cdot \text{adj}(sI - (A - BK))}{\det(sI - (A - BK))}$$

Following the discussion in the previous subsection on classical design, the roots of the denominator of the transfer function give the system's poles, and hence in this case the equation

$$(2.14) \quad \det(sI - (A - BK)) = 0$$

is the characteristic equation of the closed-loop system, in analogy with equation (2.3).

The goal of feedback control is to select a feedback gain matrix K such that the system exhibits the desired behavior (stability, tracking performance etc.). This can be achieved in a number of ways. One way, for example, would be to define the desired characteristics of the closed-loop system in terms of stability, damping ratios and natural frequencies. These characteristics are expressed by the system's pole locations, which are essentially determined from the eigenvalues of the closed-loop plant matrix $A-BK$. By selecting the desired locations of the system's poles and hence the eigenvalues of $A-BK$ we can assign values to the gains matrix K using the characteristic equation (2.14) by solving the linear system:

$$(2.15) \quad \det(s_n I - (A - BK)) = 0$$

where s_n are the desired complex poles of the system. This technique is called *pole-placement* and a detailed description can be found in Belanger [23].

Another group of methods for the determination of the control feedback gain K falls in the category of *optimal control methods*, which will be discussed below.

Optimal Control

In general the problem of *optimal control* is to find a time-history of the control vector $\mathbf{u}(t)$ which drives the system state from its initial to its final value while minimizing a *cost function* or *performance index* J (see Stengel [27]). The performance index can have the general form:

$$(2.16) \quad J(t_0) = \phi(\mathbf{x}(T), T) + \int_{t_0}^T L(\mathbf{x}(t), \mathbf{u}(t), t) dt$$

Here, ϕ is the *final state weighting function* (terminal cost), and L the weighting function that depends on the desired performance objectives. The engineering judgment in state-space optimal control often enters in the selection of the performance criterion, which is expressed by the weight function L . Different criteria will result in different control

trajectories, and in the case of feedback control, different closed-loop time responses and robustness properties.

One obvious advantage of this approach, is that an *optimal* control law is sought, instead of one that only ensures stability or a desired behavior. Furthermore, the control effort itself can be taken into account in the derivation of the control law since it can be included in the cost function. Multivariable optimal control methods began to be applied in the aerospace industry in the early 1980's, for example in the Boeing 767 and the General Dynamics F-16 (see Stevens and Lewis [7]).

A special case of optimal control is the Linear-Quadratic Regulator (LQR) which minimizes a quadratic cost function of the form

$$(2.17) \quad J = \frac{1}{2} \int_0^T (x^T Qx + u^T Ru) dt$$

for a linear state-space system of the form (2.5). The Q and R matrices are referred to as the state and control costs respectively. The LQR problem of finding an optimal control u that minimizes the cost (2.17) can be analytically solved yielding a linear feedback control law of the form (2.6). The resulting closed loop system possesses good stability and robustness properties (stability and robustness of LQR is discussed by Stengel [27] and Anderson and Moore [24]). Since LQR has an analytic solution and provides a simple and stable feedback control law, it has become the most widely applied optimal control method today, in aerospace applications as much as in other disciplines.

In general, calculating a control trajectory through the solution of the optimal control problem is not a trivial task. Several mathematical approaches have been tried depending on the specific characteristics of each problem. In the next subsection, two methods of approaching the optimal control problem are presented, the first drawing from the principles of variational calculus and the second from dynamic programming. Using these two approaches and starting from the general statement of the optimal control problem we arrive to the special case of the solution of the Linear-Quadratic Regulator for time-invariant systems. This solution will be used in the next section (2.2) for the design of control laws for hydrofoil vessels.

Variational calculus approach

Let us state the optimal control problem in its general form, without confining ourselves to a linear system yet:

Assume a dynamic system whose condition at each instant in time can be described by a state vector $x(t)$. The evolution of the state from the initial time $t = 0$ to the final time $t = T$ is given by the relation:

$$(2.18) \quad \frac{dx}{dt} = f(x(t), u(t))$$

where $\mathbf{u}(t)$ vector is an arbitrarily selected control input that belongs to the set of allowable controls U . We can impose an initial condition on the state

$$(2.19) \quad x(0) = x_0$$

A performance index (or cost) can be related to the state and control vectors

$$(2.20) \quad J = \psi(x(T)) + \int_0^T g(x(t), u(t)) dt$$

Here, g is referred to as the cost function and ψ as the terminal cost function. The optimal control problem, as stated before, is to define an allowable input function $\mathbf{u}^*(t)$ that minimizes the total cost J while forcing the state from its initial value x_0 to its final value $x(T)$. Then, $\mathbf{u}^*(t)$ is called the **optimal control** or **optimal policy**.

It is somewhat difficult to attempt a direct minimization of J with respect to $u(t)$, treated as a constrained optimization problem since apart from the explicit dependence of g on u , the state vector x is also affected by the choice of u in a manner that is not modeled in the total cost equation (2.20).

However, we can 'insert' the dynamics of the system to the problem by adding to the cost an additional term that is identically zero by virtue of equation (2.18), and obtaining the modified cost:

$$(2.21) \quad \bar{J} = J - \int_0^T \lambda(t)^T \left(\frac{dx}{dt} - f(x, u) \right) dt$$

The vector λ is for the moment arbitrary since the term in parentheses is always zero, for any trajectory of the system.

Following D. Luenberger's derivation [25], we can define, for convenience, the Hamiltonian function:

$$(2.22) \quad H(\lambda, x, u) = \lambda^T f(x, u) + g(x, u)$$

The modified cost is then:

$$(2.23) \quad \bar{J} = \psi(x(T)) + \int_0^T [H(\lambda, x, u) - \lambda^T \frac{dx}{dt}] dt$$

Assume a certain nominal control input $u(t)$. We will now try to find conditions under which the control input $u(t)$ is optimal, i.e. minimizes the cost. Take a small change δu (a variation) in $u(t)$ that defines a new control input $v(t)$:

$$(2.24) \quad v(t) = u(t) + \delta u(t)$$

A new state trajectory results, which can be called $x(t)+\delta x(t)$. The term δx is small, since the state trajectory depends on the time integral of $u(t)$. Hence, the modified cost undergoes a variation:

$$(2.25) \delta \bar{J} = \psi(x(T) + \delta x(T)) - \psi(x(T)) + \int_0^T [H(\lambda, x + \delta x, v) - H(\lambda, x, u) - \lambda^T \frac{d\delta x}{dt}] dt$$

Integrating by parts, and approximating to first order using Taylor's theorem the expression for the modified cost becomes:

$$(2.26) \quad \begin{aligned} \delta \bar{J} = & [\psi_x(x(T)) - \lambda^T(T)] \delta x(T) + \lambda(0) \delta x(0) \\ & + \int_0^T [H_x(\lambda, x, u) + \frac{d\lambda^T}{dt}] \delta x dt \\ & + \int_0^T [H(\lambda, x, v) - H(\lambda, x, u)] dt + H.O.T. \end{aligned}$$

In order to simplify the above expression, at this point we can specify a trajectory for $\lambda(t)$. Our final aim is to be left with an explicit requirement for the Hamiltonian H which will provide a criterion for the optimal control function. We can thus select λ in a way that will make the first integral in (2.26) vanish:

$$(2.27) \quad \frac{d\lambda^T}{dt} = -H_x(\lambda, x, u)$$

satisfying final condition:

$$(2.28) \quad \lambda^T(T) = \psi_x(x(T))$$

Equation (2.27) is referred to as the **adjoint equation**, and λ can be referred to as the **adjoint state**. As will be seen in the Dynamic Programming approach to the optimal control problem, vector λ defined this way has a certain physical property.

The problem stated by equations (2.27) and (2.28) can be solved for λ backwards in time if the state and control trajectories are known.

Under (2.27), the variation in the modified cost becomes (note that $\delta x(0) = 0$ since a variation in the control input cannot affect the initial state of the system):

$$(2.29) \quad \delta \bar{J} = \int_0^T [H(\lambda, x, v) - H(\lambda, x, u)] dt + H.O.T.$$

Assume now that the original control function $u(t)$ is **optimal**. This requires that $\delta \bar{J} > 0$ for any varied control $v(t)$. Otherwise, we would be able to select a new control $v(t)$ that reduces the modified cost (and hence the cost J), and $u(t)$ would not be optimal i.e. it would not minimize J .

The essence of the previous analysis is that **if the adjoint state satisfies (2.27), then any variation $\delta\bar{J}$ in the modified cost due to a variation δu in the control can be expressed by equation (2.29). Moreover, if u is the optimal control, then $\delta\bar{J}$ must be positive (increase in cost) for any control variation δu .** Hence from (2.29) we deduce that the **optimal control u that minimizes (2.23), also minimizes the Hamiltonian H .** If this was not true, the variation in the Hamiltonian

$$(2.30) \quad \delta H = H(\lambda, x, v) - H(\lambda, x, u)$$

due to the variation in control δu could become negative since the new control $v(t)=u(t)+\delta u$ could possibly give a smaller value to H (for clarity it should be repeated here that the above is true if the adjoint state λ satisfies the adjoint problem (2.27) and (2.28)). This would also make the cost variation $\delta\bar{J}$ negative, meaning that the original control $u(t)$ is not optimal.

The previous argument is stated formally in Pontryagin's Minimum Principle, which in words states that the optimal control $u(t)$ minimizes the Hamiltonian function as defined in (2.22):

Minimum Principle. If u and x are the optimal control and respective trajectory for the optimal control problem, then **there is an adjoint trajectory λ such that the following set of relations is satisfied:**

$$(2.31) \quad \left\{ \begin{array}{ll} \frac{dx}{dt} = f(x(t), u(t)) & \text{(state equation)} \\ x(0) = x_0 & \text{(initial state)} \\ \frac{d\lambda^T}{dt} = -H_x(\lambda, x, u) & \text{(adjoint equation)} \\ \lambda(T)^T = \psi_x(x(T)) & \text{(adjoint final condition)} \\ H(\lambda, x, u) = \lambda^T f(x, u) + g(x, u) & \text{(Hamiltonian)} \\ \text{for all } t \in (0, T) \text{ and all } v \in U \text{ allowable controls,} \\ u = \operatorname{argmin}_{v \in U} (H(\lambda, x, v)) & \text{(minimum condition)} \end{array} \right.$$

In theory, the above is a problem for λ , x and u which, if solved, yields the optimal trajectory and control. For a few examples of solutions for the optimal control problem, see for example Bertsekas [26] or Luenberger [25].

Linear system with quadratic cost

The LQR problem is a special case of the optimal control problem. As stated before, it has the attractive property that its solution yields a **linear feedback** form of optimal control.

If the state equation has a linear form and the cost is quadratic in x and u , working out the algebra from the general problem (2.31) yields:

$$(2.32) \quad \left\{ \begin{array}{l} \frac{dx}{dt} = A(t)x(t) + B(t)u(t) \quad (\text{state equation}) \\ x(0) = x_0 \quad (\text{initial state}) \\ J = \frac{1}{2} \int_0^T (x^T Qx + u^T Ru) dt \quad (\text{cost}) \\ \frac{d\lambda^T}{dt} = -\lambda(t)^T A(t) + x(t)^T Q(t) \quad (\text{adjoint equation}) \\ \lambda(T)^T = 0 \quad (\text{adjoint final condition}) \\ H(\lambda, x, u) = \lambda(t)^T A(t) + \lambda(t)^T B(t)u(t) - \\ \quad - \frac{1}{2} x(t)^T Q(t)x(t) - \frac{1}{2} u(t)^T R(t)u(t) \quad (\text{Hamiltonian}) \end{array} \right.$$

for all $t \in (0, T)$ and all $v \in U$ allowable controls,
 $u = \operatorname{argmin}_{v \in U} (H(\lambda, x, v))$ (minimum condition)

Note that matrix Q is a positive semidefinite matrix expressing the state cost, and R is a positive definite matrix (and hence invertible) expressing the control cost. Following the Minimum Principle, we wish to minimize the Hamiltonian with respect to $u(t)$ in order to find the optimal control. Demanding a zero derivative $H_u = 0$, we have:

$$(2.33) \quad u(t) = R^{-1}(t)B(t)\lambda(t)$$

And, substituting in the original system and adjoint equations we have:

$$(2.34) \quad \left\{ \begin{array}{l} \frac{dx}{dt} = A(t)x(t) + B(t)R^{-1}(t)B(t)^T \lambda(t) \\ \frac{d\lambda}{dt} = Q(t)x(t) - A(t)^T \lambda(t) \\ \text{with} \\ x(0) = x_0, \lambda(T) = 0 \end{array} \right.$$

The problem now is to find a solution for (2.34). We can try a solution in which λ is expressed as a linear function of x :

$$(2.35) \quad \lambda(t) = -P(t)x(t)$$

Here, P is an unknown n by n matrix. If we substitute in (2.34):

$$(2.36) \quad \begin{cases} \frac{dx}{dt} = (A(t) - B(t)R(t)^{-1}B(t)^T P(t))x(t) \\ -\frac{d}{dt}(P(t)x(t)) = (Q(t) + A(t)^T P(t))x(t) \end{cases}$$

Expanding the second time derivative, left - multiplying by P the first relation and adding we get:

$$(2.37) \quad 0 = \left(\frac{dP}{dt} + P(t)A(t) + A(t)^T P(t) - P(t)B(t)R(t)^{-1}B(t)^T P(t) + Q(t) \right) x(t)$$

Equation (2.37) must hold for all values of the optimal trajectory x since it is derived from the system (2.34). Hence, a differential equation results for the unknown matrix P:

$$(2.38) \quad -\frac{dP}{dt} = P(t)A(t) + A(t)^T P(t) - P(t)B(t)R(t)^{-1}B(t)^T P(t) + Q(t)$$

with $P(T) = 0$ (since $\lambda(T) = 0$)

Equation (2.38) is referred to as the *Riccati equation*.

We are now in a position to outline the solution for the general, time-variant LQR problem: The Riccati equation is first solved backwards for P(t). Then, from (2.33) the optimal control u is:

$$(2.39) \quad \begin{aligned} u(t) &= -R^{-1}(t)B(t)P(t)x(t) \\ \text{or,} \\ u(t) &= -K(t)x(t), \quad K(t) = R^{-1}(t)B(t)P(t) \end{aligned}$$

The optimal control has a linear feedback form, with a time-varying gain K(t). K(t) can be calculated off-line, then applied to compute the control at each instant of the system's operation.

In the case where the system's dynamics are linearized around a time-invariant linear set of equations,

$$(2.40) \quad \frac{dx}{dt} = Ax(t) + Bu(t)$$

and the cost matrices Q and R are also time invariant, a simpler form of the control law can be derived. Assuming a very far terminal time $T \rightarrow \infty$, the solution of the Riccati equation (2.38)

is expected to approach $\frac{dP}{dt} = 0$ as t has advanced enough towards zero. Then an algebraic

Riccati equation can be solved for P:

$$(2.41) \quad 0 = PA + A^T P - PBR^{-1}B^T P + Q$$

and the control law is

$$(2.42) \quad \begin{aligned} u(t) &= -R^{-1}BPx(t) \\ \text{or,} \\ u(t) &= -Kx(t), \quad K = R^{-1}BP \end{aligned}$$

The Dynamic Programming approach

The Dynamic Programming (DP) approach to the optimal control problem of a continuous time system is based on the Hamilton-Jacobi-Bellman (HJB) equation which will be presented shortly. The HJB equation is essentially a continuous-time version of the dynamic programming algorithm.

We will very briefly introduce the dynamic programming algorithm. Given a discrete-time dynamic system, with state vector x , control vector u and random disturbance w :

$$(2.43) \quad x_{k+1} = f_k(x_k, u_k, w_k), \quad k = 0, 1, \dots, N$$

and an expected cost (starting at state x_0):

$$(2.44) \quad J(x_0) = E \left\{ g_N(x_N) + \sum_{k=0}^{N-1} g_k(x_k, u_k, w_k) \right\}$$

we seek the **optimal policy**, i.e. the sequence of control inputs u_k that minimize J . Here, g_k essentially , plays the same role as cost function g in (2.20) and denotes the added cost at each timestep k due to current state x_k , applied control u_k and disturbance w_k .

The dynamic programming algorithm, based on the principle of optimality (see Bertsekas [26]), states that for every initial state x_0 the optimal cost $J^*(x_0)$ is equal to $J_0(x_0)$ given by the last step of the following algorithm (which proceeds backward in time starting from period $N-1$):

$$(2.45) \quad \begin{aligned} J_N(x_N) &= g_N(x_N) \\ J_k(x_k) &= \min_{u_k} E \{ g_k(x_k, u_k, w_k) + J_{k+1}(f_k(x_k, u_k, w_k)) \}, \quad k = 0, 1, \dots, N-1 \end{aligned}$$

The dynamic programming algorithm can be applied to continuous-time deterministic and stochastic optimal control. We can begin by recalling the deterministic optimal control problem where we wish to minimize the total cost J :

$$(2.46) \quad \left\{ \begin{aligned} \frac{dx}{dt} &= f(x(t), u(t)) \quad (\text{state equation}) \\ x(0) &= x_0 \quad (\text{initial condition}) \\ J &= \psi(x(T)) + \int_0^T g(x(t), u(t)) dt \quad (\text{cost}) \end{aligned} \right.$$

In order to apply the DP algorithm, we can discretize the total time period T into N timesteps of length δt :

$$(2.47) \quad \delta t = \frac{T}{N}, \text{ and hence} \\ t = k \cdot \delta t, \quad k=0, 1, \dots, N$$

Then the continuous time system and the cost function can be approximated:

$$(2.48) \quad x_{k+1} = x_k + f(x_k, u_k)\delta t, \text{ where } x_k = x(k\delta t) \text{ and } u_k = u(k\delta t) \\ J = \psi(x_N) + \sum_{k=0}^{N-1} g(x_k, u_k)\delta t$$

Applying the DP algorithm for the discretized system,

$$(2.49) \quad J^*(N\delta t, x) = \psi(x), \\ J^*(k\delta t, x) = \min_u \{g(x, u)\delta t + J^*((k+1)\delta t, x + f(x, u)\delta t)\}$$

If we expand the cost at $k+1$ instant in the RHS of the second equation by Taylor, we have:

$$(2.50) \quad J^*(k\delta t, x) = \min_u \{g(x, u)\delta t + J^*(k\delta t, x) + \nabla_x J^*(k\delta t, x)\delta t \\ + \nabla_x J^*(k\delta t, x)^T f(x, u)\delta t + H.O.T.\}$$

Canceling equal terms, dividing by δ and taking the limit as δ converges to zero yields the **Hamilton-Jacobi-Bellman** equation:

$$(2.51) \quad 0 = \min_u \{g(x, u) + \nabla_x J^*(t, x) + \nabla_x J^*(t, x)^T f(x, u)\}$$

The HJB equation is essentially a differential equation for the optimal cost J^* . It can be used in the study of optimal control problems – indeed, if the HJB equation is solved for a specific problem and its right hand side minimized with respect to u , then the optimal control is obtained. This can be justified mathematically through the Sufficiency Theorem (see Bertsekas [26]).

We can use the HJB equation to derive the linear feedback solution of the Linear-Quadratic Regulator. Indeed, writing the HJB equation for problem (2.32) (in the time-invariant form for simplicity):

$$(2.52) \quad 0 = \min_u \{x^T Qx + u^T Ru + \nabla_x J(t, x) + \nabla_x J(t, x)^T (Ax + Bu)\}$$

we can **try** a solution of the HJB equation of the form:

$$(2.53) \quad J^*(t, x) = x^T P(t)x, \text{ hence} \\ \nabla_x J^*(t, x) = 2P(t)x$$

Substituting in (2.52) and minimizing with respect to u (demanding a zero derivative) we have:

$$(2.54) \quad u = -R^{-1}B^T P(t)x$$

Substituting this optimal value of u in (2.52) we end up with the Riccati equation for P :

$$(2.55) \quad -\frac{dP}{dt} = P(t)A + A^T P(t) - P(t)BR^{-1}B^T P(t) + Q$$

Summarizing, the solution of the Riccati equation for P yields the optimal linear feedback control (2.54).

The previous two approaches to the LQR problem arrive at the same solution. The difference between them is that in the first approach, one introduces an initially arbitrary Hamiltonian function, uses calculus of variations to derive the Minimum Principle and finds the linear feedback solution by application of the Minimum Principle. In the DP approach, the DP algorithm which is based on the principle of optimality is applied in a continuous time problem, the HJB equation is derived and then is used to derive the LQR solution.

The two approaches come together if one notices that the Minimum Principle can be proved to be a consequence of the HJB equation (see Bertsekas [26]). Indeed, from equation (2.51) we have:

$$(2.56) \quad u^*(t) = \arg \min \{g(x, u) + \nabla_x J^*(t, x)^T f(x, u)\}$$

If we compare this expression with the Minimum Principle (2.31) we will see that they are essentially the same. Equation (2.56) states that the optimal control u^* minimizes the bracketed expression. In order to find u^* , one needs to calculate the trajectory of $\nabla_x J^*(t, x)$ along the optimal state trajectory x^* . This is often simpler than solving the full HJB equation for the optimal cost J^* .

The equation for the trajectory of $\nabla_x J^*(t, x)$ can be derived by setting to zero the gradient of the bracketed expression in (2.56). We get:

$$(2.57) \quad \frac{d}{dt}(\nabla_x J^*(t, x^*)) = -\nabla_x f(x^*, u^*)(\nabla_x J^*(t, x)) - \nabla_x g(x^*, u^*)$$

Equation (2.57) is true for all t but only along the optimal state trajectory x^* . Hence it becomes apparent that $\nabla_x J^*(t, x^*)$ is a function of time only and is actually the adjoint state trajectory $\lambda(t)$ from the previous analysis, and the bracketed expression in (2.56) is the Hamiltonian as defined in (2.31). In the general case of the optimal control problem one needs

to solve for the adjoint trajectory using (2.57) and then minimize with respect to u in order to obtain the optimal control u^* , instead of solving for the full HJB equation.

We can argue that the second approach to the optimal control problem is more powerful since it takes into account stochastic disturbances to the system. It could also be described as more elegant since it does not require the explicit definition of the adjoint state variable. Indeed, by applying the HJB equation one arrives at the adjoint equation in a straightforward manner. In contrast, through the variational approach one defines an arbitrary adjoint state λ initially and then demands that it satisfies the adjoint equation in order to simplify the expression for the variation in the cost functional.

Significance of the Q and R weight matrices

The Q and R weight matrices appear in the cost functional J of the Linear Quadratic Regulator as stated in problem (2.32). They are selected when the control law is designed, and their significance as tuning parameters is discussed here.

Q and R matrices are referred to as state weight (or cost) matrix and control weight (or cost) matrix respectively. State weight matrix Q expresses how much a deviation from the desired state is penalized. In analogy, control weight matrix R expresses the penalty assigned to control usage. The Q and R weight matrices provide the way of defining the controlled system's desired behavior. Roughly speaking, the selection of the numerical values of Q and R is the qualitative equivalent to the selection of system pole positions. Performance and stability requirements of the system regulate the choice of these numerical values.

Let's take a simplified example to demonstrate the agility of such a formulation. Assuming we need to design a course keeping autopilot for a combat aircraft, it is initially evident that keeping the correct course with a minimum amount of error is desirable, in order for the aircraft to reach the target with accuracy. Hence an LQR design for the autopilot would employ a relatively large state cost Q and small control cost R. If for some reason power availability becomes limited for the aircraft, it is damaged for example, then large control surface motion start becoming expensive since they require power usage for the hydraulic system and also increase aerodynamic drag. Then the autopilot's control system can switch to a 'power save' mode with a larger R matrix in order to reduce control usage.

The initial selection of Q and R can be based on a rule-of-thumb for the selection of state and control costs in multiple-input, multiple-output problems often referred to as 'Bryson's rule' (see for example Anderson and Moore [8]). Assume that maximum allowable values x_{iMAX} and u_{jMAX} are set for the state and control vector. Then according to a simple form of Bryson's rule, we initially select $q_i=1/(x_{iMAX})^2$ and $r_j=1/(u_{jMAX})^2$ for the elements of the state and control cost matrices.

This provides a starting point for the control gain calculation. It is a useful method in the sense that it provides a straightforward intuitive understanding of the effect that Q and R matrices have on the control gain K and the closed-loop system's behavior. If it is considered important that a certain state variable x_i deviates very little from its nominal 'zero' position, it is translated to a small allowable value $x_{i \text{ MAX}}$ for this variable and subsequently to a large respective cost $q_i=1/x_i^2$. The end result is that the control gain will be such that it will not allow the system variable x_i to deviate too much from its zero position. After the initial selection of the cost matrices and calculation of the gains, simulations are run and the system's performance is examined. Subsequently, Q and R are iteratively modified until the closed-loop system has the required behavior.

Notes on stochastic disturbances

In real-life applications most systems are subject to random disturbances that cannot be specified ahead of time. A linear, continuous time system of the form (2.5) subject to random disturbances can be written:

$$(2.58) \quad \begin{aligned} \dot{x} &= Ax + Bu + Gw \\ y &= Cx + Fv \end{aligned}$$

where w is the disturbance to the state and v is the measurement disturbance.

It becomes apparent from equations (2.58) that two sources of uncertainty enter the system: one affecting the state trajectory (since the disturbance time history w(t) is not known a priori), and the other affecting our knowledge of the system's state (since measurement y is affected by the uncertain disturbance v(t)).

The second source of uncertainty is treated by the wide subject of *optimal state estimation*. Achieving an accurate estimate of the current state of the system is obviously crucial in the application of a feedback control law where the control force is defined by the current state of the system. A widely applied method when measurement uncertainty exists is the Linear-Quadratic Gaussian (LQG) regulator, where an optimal state estimator designed using the Kalman filter is combined with a Linear-Quadratic feedback controller. LQG design and the Kalman filter is discussed in many references, for example Lewis [9] and Stengel [27]. Throughout this work, however, it is assumed that perfect state information exists.

In the case where a random state disturbance exists, a stochastic optimal control law minimizing the expected value of the cost functional can be designed. In general, the solution of stochastic optimal control problems is very complex and closed-form solutions are very rare. The problem can be somewhat simplified if the stochastic disturbances to the state are small and have a zero mean value around a deterministic nominal trajectory. Then, an optimal control law can be designed to force the mean value of the state along the nominal trajectory. What remains is perturbations of the state vector around the nominal trajectory due to the

effect of the random state disturbance $w(t)$ as in the sketch of Figure 53. Assuming that these perturbations are small, the system's dynamics can be linearized around the nominal trajectory. Then a linear feedback control law can be designed in order to minimize the state perturbations. If we denote the deterministic nominal state trajectory x^* and the corresponding optimal control u^* , then the total state and control vectors are:

$$(2.59) \quad \begin{aligned} x(t) &= x^*(t) + \Delta x(t) \\ u(t) &= u^*(t) + \Delta u(t) \end{aligned}$$

where $\Delta x(t)$ is the state perturbation around x^* and $\Delta u(t)$ is the feedback control component that aims to minimize $\Delta x(t)$.

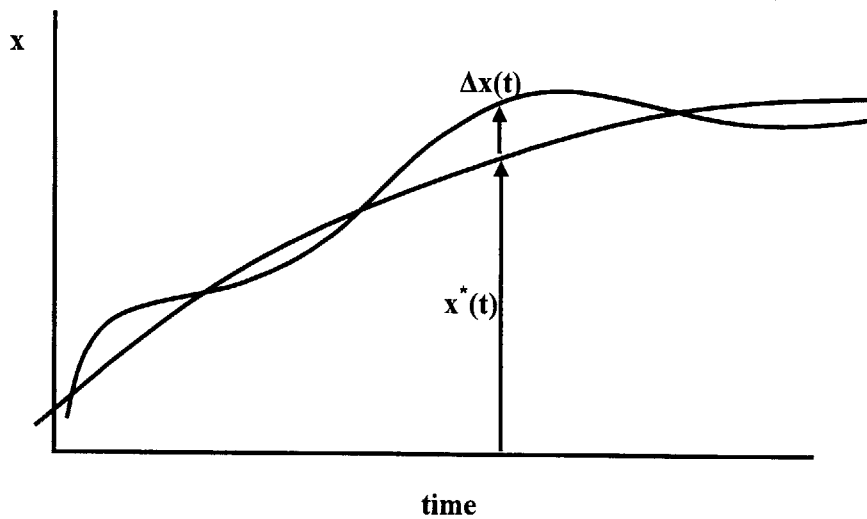


Figure 53: Perturbation around nominal trajectory

The linearized state dynamics around x^* and the corresponding feedback control law can be written:

$$(2.60) \quad \begin{aligned} \Delta \dot{x} &= A\Delta x + B\Delta u \\ \Delta u &= -K\Delta x \end{aligned}$$

The feedback gain K can be selected using an optimal control method such as the Linear-Quadratic Regulator, based on the linearized perturbation dynamics (2.60). This technique of treating stochastic control problem is often referred to as *neighboring optimal control* and is discussed in detail by Stengel [27] and Belanger [23].

Motion control of hydrofoil vessels and ocean wave disturbance

The problem of motion control of hydrofoil vessels examined in the present work is a problem subject to random disturbances. The vessel is subject to external disturbances from the ambient waves which in real life are random entities that are not known a priori.

The essentially deterministic approach previously described is followed in this work. In this case, the nominal trajectory is defined by the zero mean value of the free surface elevation and consequently the zero mean value of the vessel's heave and pitch motion, as in the sketch of Figure 54 where the heave motion of a vessel advancing in incident waves is shown as a perturbation around a $\xi_3=0$ mean trajectory. The seakeeping equations of motion are linear equations describing the ship's motion as a linear system around these zero mean values. As mentioned before, in section 2.2 control laws are designed using the Linear-Quadratic Regulator in order to minimize vessel motions around the zero state trajectory in the presence of wave disturbances.

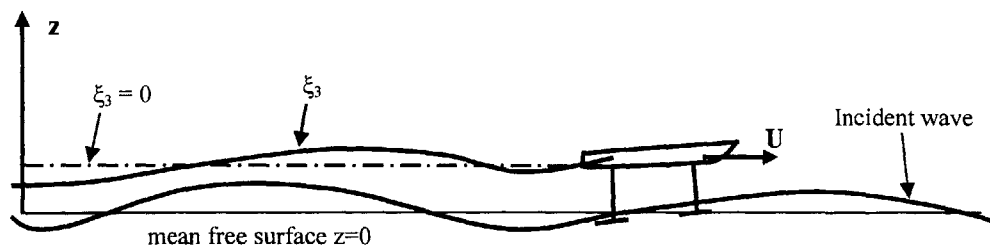


Figure 54: Hydrofoil motion around nominal trajectory

2.1.c. Contemporary Research on the Control of Marine Vehicles

In this subsection, we state some examples of modern research on the control of marine vehicles. In the frequency domain, Rhee and Lee [16], propose the use of a representative or design frequency selected by minimizing the uncertainty in the nominal plant (as compared to the real plant). In the time domain, Kenevissi et al [17] use a neural optimal controller employing on-line switching of different controllers according to the sea state (which is translated into an encounter frequency). Various LQR gains are used, each one optimized for a specific design sea state. This control is sub-optimal between the design frequencies, and employment of an Artificial Neural Networks (ANN) neural optimal controller (NOC) is used in order to make the control near-optimal away from the design points. Rostgaard [18] compares an Linear-Quadratic Gaussian (LQG) adaptive autopilot with a classical PID autopilot. An overview of Adaptive Control Systems is given by Fossen [19].

Jia [20] demonstrates a multiple algorithms approach in the design of an autopilot. A GMV (generalized minimum variance) main controller is used, with integral and LQG gains superposed to strengthen disturbance rejection, and a Proportional-Integral-Derivative (PID) controller takes over in the case when heading errors exceed a certain threshold. The total control law comes from the superposition of the various gains. Finally, Proportional – Derivative (PD) controllers utilizing fuzzy logic for the determination of the PD gains have been applied, mainly on the steering control of Autonomous Underwater Vehicles, see for example Akkizidis [21].

2.2. Motion control of hydrofoil craft

In this section, the seakeeping equations of motion are used to create a linear-time invariant state-space model which is then applied to the design of an optimal control law using the Linear-Quadratic Regulator. The section begins with the derivation of a general state-space model for vessels operating on or near the free surface and moving in the heave and pitch modes. The section then continues with a brief description of the control law, the general vessel model used and the control system architecture, and a short discussion on the specific significance of the state and control cost matrices Q and R . In the numerical results presented, two vessel models are investigated: a hydrofoil ship under the influence of hydrostatic restoring effects, and the same vessel in the condition it would normally cruise without any restoring. State-space models are derived from the seakeeping equations of motion, control laws are designed using the LQR algorithm, and simulations are run in order to evaluate the performance of these control laws. Trailing-edge flaps are used as control surfaces. Numerical results are presented from efforts to minimize motions with the vessel advancing in ambient waves. The first set of experiments (with hydrostatic restoring in heave and pitch modes) serves to show that the controllers designed can improve the seakeeping behavior of a vessel already stable in heave and pitch. The second set of experiments (without any restoring) provides feedback on the controller's performance in providing a stable and smooth ride for a vessel that would otherwise be potentially unstable in the coupled heave and pitch modes, due to the negative c_{35} restoring coefficient as will be discussed later. The second model aims to simulate the realistic case of a hydrofoil ship with fully submerged inverted-T wings.

It must be noted here that the linear, time-invariant state-space model of the hydrofoil ship used for the design of LQR control laws in the numerical experiments of this section is based on a state vector defined by the vessel's position and velocity. Hence the linear feedback control law that results (of the general form (2.6) or (2.42) as shown in the derivation of the LQR algorithm in the previous section) dictates the control vector (flap angles) at each timestep as a linear function of the vessel's position and velocity. Essentially, and following on the previous section's discussion on the LQR algorithm, the control law design consists of the calculation of the optimal gain matrix K from the solution of the Riccati equation (refer to section 2.1.b for more details). As seen in the previous section, the state-space model and hence the vessel and flap dynamics (matrices A and B) are used for the calculation of the optimal gain matrix. The incident wave is treated as an external disturbance in the state-space model and hence it is not taken into account during the design of the control law. After the control law has been designed, during the actual simulation, incident waves

(sinusoidal or stochastic) hit the vessel and cause deviations from its desired zero mean position in heave or heave and pitch. The state vector hence becomes non-zero, and the state feedback control law applies optimal flap angles in order to bring the ship back to its zero-mean as quickly and smoothly as possible. The ability of the LQR control law to accomplish this (keep the vessel as close to its zero-mean position as possible in a smooth manner with low vertical accelerations) is the main question investigated in this section, with encouraging results.

We must also note that the approach followed for the state-space model derivation in this section results in a linear time-invariant model which does not account for hydrodynamic memory effects. However free surface memory effects are taken into account during the actual numerical simulations used to verify the performance of the motion control mechanism. These results are encouraging for the use of such a model in the design of control laws for hydrofoil vessels.

2.2.a Vessel heave and pitch equations of motion – derivation of a state-space model

The linearized equations of motion of a submerged hydrofoil around its zero-mean cruising position in the heave and pitch modes can be written:

$$(2.61) \quad \begin{pmatrix} \alpha_{033} + m_{33} & \alpha_{035} + m_{35} \\ \alpha_{053} + m_{53} & \alpha_{055} + m_{55} \end{pmatrix} \begin{pmatrix} \ddot{\xi}_3 \\ \ddot{\xi}_5 \end{pmatrix} + \begin{pmatrix} b_{033} & b_{035} \\ b_{053} & b_{055} \end{pmatrix} \begin{pmatrix} \dot{\xi}_3 \\ \dot{\xi}_5 \end{pmatrix} + \begin{pmatrix} C_{33} & C_{35} \\ C_{53} & C_{55} \end{pmatrix} \begin{pmatrix} \xi_3 \\ \xi_5 \end{pmatrix} = \\ = \begin{pmatrix} F_{3m}(\ddot{\xi}_3, \dot{\xi}_3, \xi_3, t) + F_{3EX}(t) \\ F_{5m}(\ddot{\xi}_3, \dot{\xi}_3, \xi_3, t) + F_{5EX}(t) \end{pmatrix}$$

In (2.61), a_{0ij} and b_{0ij} are the impulsive added mass and damping coefficients which remain constant in time. Terms c_{ij} are the restoring coefficients and m_{ij} are the vessel inertial quantities (in heave and pitch modes). F_{iEX} are the external exciting forces in the two modes. The term F_{im} on the right hand side denote the hydrodynamic memory force due to the vessel's motion history. It must be noted here that for conventional ships, the zero-mean position is defined by the balance between weight and hull buoyancy. In the hydrofoil's case, this position is defined by the balance between weight, steady lift force and foil buoyancy (for an analysis of the equations of motion of hydrofoil ships also see Asseo [2]).

The values of a_{033} and b_{033} are calculated from the solution of the impulsive boundary value problem with zero potential on the free surface ($z=0$ plane) as described in the first part of this work. They can be considered to be the infinite-frequency limits of the added mass and damping coefficients.

Hydrofoil craft restoring coefficients

In general the restoring coefficients c_{ij} are near-zero in the case of a fully submerged hydrofoil, apart from the c_{35} coefficient. In some of the experiments presented in this work, no parts of the vessel protruding through the free surface have been taken into account (struts, rudders etc.) and hence no hydrostatic restoring exists. The c_{35} coefficient however expresses the fact that a pitch angle induces a change on the hydrofoil's angle of attack, and hence a resulting lift force. This can be seen as a realistic physical description of a hydrofoil ship with fully submerged, inverted-T type wings.

The c_{35} coefficient is calculated for small pitch angles assuming a linear variation of lift with the angle of attack. The total lift force on one foil can be written, assuming that the lift coefficient varies linearly with angle of attack:

$$(2.62) \quad L_{TOT} = \frac{1}{2} \rho \frac{dC_L}{d\alpha} (\alpha_{TOT} - \alpha_0) Chord U^2$$

where ρ is the water density, α_{TOT} is the total angle of attack and α_0 is the angle of zero lift, U is the vessel's speed, and C_L is the lift coefficient. From (2.62) the lift component due to the pitch angle ξ_5 can be extracted in order to calculate the c_{35} restoring coefficient (see Sclavounos et al. [32]):

$$(2.63) \quad c_{35} = -\frac{1}{2} \rho \frac{dC_L}{d\alpha} Chord U^2$$

The lift coefficient slope $\frac{dC_L}{d\alpha}$ is 2π for a flat plate in potential flow. In this work it is estimated through numerical experiments with increasing lift angle. As a result the motion-induced lift effects, specifically the vertical force resulting from non-zero pitch angles, are treated as quasi-static discarding the wake and free-surface memory effects.

A similar procedure will be followed later for the calculation of the coefficients of the trailing edge flap induced force in order to create an input matrix for the state-space model of the vessel.

For the motion control simulations that follow, integration of the equations of motion (2.61) is required. In order to estimate the ambient wave exciting force and the motion induced memory force F_{im} , the two-dimensional numerical solver described in the first part of this work is used.

The memory part of the motion induced force is estimated through the free surface pressure-relief problem (see Kring [3]). Furthermore, the time-varying vorticity shed into the wake due to the variation of the flow field from the action of the incident wave is also taken

in account. In order to clear out the force calculation effected for the integration of the equations of motion, let us write the total force that appears on the right hand side of the equations of motion (2.61):

$$(2.64) \quad \begin{pmatrix} F_{3TOT} \\ F_{5TOT} \end{pmatrix} = \begin{pmatrix} F_{3m} + F_{3EX} \\ F_{5m} + F_{5EX} \end{pmatrix}$$

The numerical code, through the solution of the linearized BVP and pressure integration around the body surface, calculates the total forces F_{TOT} which include ambient wave excitation F_{iEX} (diffraction and Froude-Krylov components) and the hydrodynamic wave memory vessel motion induced force F_{im} . As a result, during the actual motion simulation, memory effects are taken in account, except for the motion-induced time varying lift force which is treated as quasi-static through the restoring coefficient c_{35} as noted before.

However a state-space model is required for the design of the LQR optimal control law. This model has the form of a linear, time invariant dynamic system as seen in the previous section. For the creation of state-space models for hydrofoil vessels in this work, only the left hand side of the equations of motion (2.61) is used, with the forces appearing on the right-hand side treated as disturbances. Hence all memory effects (due to the free surface and the wake) will be neglected for the design of control laws.

State-Space Model

In this paragraph state equations are derived for the general case of a vessel operating on or near the free surface and moving in the heave and pitch modes. No assumptions on the nature of the restoring coefficients are made at this point. Hence the model derived is not confined to the case of dynamically supported hydrofoil ships but can be used for other sorts of vessels using hydrofoils with trailing-edge flaps as active control surfaces. The derivation is done for the case of a vessel supported by two wings, but extension to a larger number of wings is trivial.

As said in the previous section a state-model for a dynamical system modeled as a linear, time invariant system can be written as:

$$(2.65) \quad \dot{x} = Ax + Bu + D$$

where x is the state vector, u is the control vector and D is the external disturbance to the system. We repeat here that matrix A is referred to as the plant matrix, and in the case of a mechanical system it can include inertial, damping and restoring coefficients, and matrix B is the input matrix which models the effect of the control vector on the state x .

Taking the equation of motion (2.61), we can separate the exciting force into an ambient wave and control induced components:

$$(2.66) \quad \begin{pmatrix} \alpha_{033} + m_{33} & \alpha_{035} + m_{35} \\ \alpha_{053} + m_{53} & \alpha_{055} + m_{55} \end{pmatrix} \begin{pmatrix} \ddot{\xi}_3 \\ \ddot{\xi}_5 \end{pmatrix} + \begin{pmatrix} b_{033} & b_{035} \\ b_{053} & b_{055} \end{pmatrix} \begin{pmatrix} \dot{\xi}_3 \\ \dot{\xi}_5 \end{pmatrix} + \begin{pmatrix} C_{33} & C_{35} \\ C_{53} & C_{55} \end{pmatrix} \begin{pmatrix} \xi_3 \\ \xi_5 \end{pmatrix} = \begin{pmatrix} F_{3m} + F_{3CONTROL} + F_{3W} \\ F_{5m} + F_{5CONTROL} + F_{5W} \end{pmatrix}$$

where $F_{iCONTROL}$ is the control induced force (in this case the force due to flap deflection) and F_{iW} is the ambient wave induced excitation force and F_{im} represents the wake and free-surface memory effects induced by the vessel motions.

Control Force

In order to arrive at a state-space model where the control effect has a linear form, we can linearize the control force in a quasi-static manner to first order:

$$(2.67) \quad \begin{aligned} F_{3CONTROL} &= \frac{\partial F_{3CONTROL}}{\partial \delta_{Fore}} \cdot \delta_{Fore} + \frac{\partial F_{3CONTROL}}{\partial \delta_{Aft}} \cdot \delta_{Aft} + O(\delta_{Fore}^2, \delta_{Aft}^2) \\ &\cong \frac{\partial F_{3CONTROL}}{\partial \delta_{Fore}} \cdot \delta_{Fore} + \frac{\partial F_{3CONTROL}}{\partial \delta_{Aft}} \cdot \delta_{Aft} \\ &= L_{\delta 3Fore} \cdot \delta_{Fore} + L_{\delta 3Aft} \cdot \delta_{Aft} \\ F_{5CONTROL} &= \frac{\partial F_{5CONTROL}}{\partial \delta_{Fore}} \cdot \delta_{Fore} + \frac{\partial F_{5CONTROL}}{\partial \delta_{Aft}} \cdot \delta_{Aft} + O(\delta_{Fore}^2, \delta_{Aft}^2) \\ &\cong \frac{\partial F_{5CONTROL}}{\partial \delta_{Fore}} \cdot \delta_{Fore} + \frac{\partial F_{5CONTROL}}{\partial \delta_{Aft}} \cdot \delta_{Aft} \\ &= L_{\delta 5Fore} \cdot \delta_{Fore} + L_{\delta 5Aft} \cdot \delta_{Aft} \end{aligned}$$

where δ_{Fore} and δ_{Aft} are the flap angles on the forward and aft foil respectively, and $L_{\delta ij}$ is the first derivative of the control force in the i -mode due to flap angle δ_j . In this work the derivatives $L_{\delta 3Fore}$, $L_{\delta 3Aft}$, $L_{\delta 5Fore}$, $L_{\delta 5Aft}$ are estimated by a series of calm water experiments executed with gradual increase in the flap angles, and finite differencing is used. The maximum allowable flap angle in the numerical experiments in this work is set to 15° and in most cases values are below 10° , justifying the linearization in (2.67).

Before we continue, we must clear out the following: the quasi-static modeling of the control force in (2.67), which disregards wake memory effects, is used for the creation of an input matrix for the linear state-space model in order to design LQR control laws. During the actual simulation using the numerical solver however, when the flap is deflected, the resulting change in the body shape S_B is taken in account in the solution of the BVP as described in the

first part of this work. The time varying vorticity is shed into the wake, and hence wake memory effects are not disregarded in the simulations that follow – only in the design of the control law.

State-Space Form

Having defined the control effect, the coupled equations of motion can be manipulated into state equations in suitable formulation for the application of optimal control theory. Equation (2.66) gives:

$$(2.68) \quad \begin{pmatrix} \ddot{\xi}_3 \\ \ddot{\xi}_5 \end{pmatrix} = - \begin{pmatrix} \alpha_{033} + m_{33} & \alpha_{035} + m_{35} \\ \alpha_{053} + m_{53} & \alpha_{055} + m_{55} \end{pmatrix}^{-1} \begin{pmatrix} b_{033} & b_{035} \\ b_{053} & b_{055} \end{pmatrix} \begin{pmatrix} \dot{\xi}_3 \\ \dot{\xi}_5 \end{pmatrix} - \\ - \begin{pmatrix} \alpha_{033} + m_{33} & \alpha_{035} + m_{35} \\ \alpha_{053} + m_{53} & \alpha_{055} + m_{55} \end{pmatrix}^{-1} \begin{pmatrix} C_{33} & C_{35} \\ C_{53} & C_{55} \end{pmatrix} \begin{pmatrix} \xi_3 \\ \xi_5 \end{pmatrix} \\ + \begin{pmatrix} \alpha_{033} + m_{33} & \alpha_{035} + m_{35} \\ \alpha_{053} + m_{53} & \alpha_{055} + m_{55} \end{pmatrix}^{-1} \begin{pmatrix} F_{3m} + F_{3CONTROL} + F_{3W} \\ F_{5m} + F_{5CONTROL} + F_{5W} \end{pmatrix}$$

Let $[m_{ij}] = \begin{pmatrix} \alpha_{033} + m_{33} & \alpha_{035} + m_{35} \\ \alpha_{053} + m_{53} & \alpha_{055} + m_{55} \end{pmatrix}$, $[b_{ij}] = \begin{pmatrix} b_{033} & b_{035} \\ b_{053} & b_{055} \end{pmatrix}$, $[c_{ij}] = \begin{pmatrix} C_{33} & C_{35} \\ C_{53} & C_{55} \end{pmatrix}$. Then,

if we define:

$$(2.69) \quad \mathbf{x} = \begin{pmatrix} \dot{\xi}_3 \\ \dot{\xi}_5 \\ \xi_3 \\ \xi_5 \end{pmatrix} \text{ state vector, and } \mathbf{u} = \begin{pmatrix} \delta_{Fore} \\ \delta_{Aft} \end{pmatrix} \text{ control vector}$$

equation (2.68) becomes:

$$(2.70) \quad \begin{pmatrix} \ddot{\xi}_3 \\ \ddot{\xi}_5 \\ \dot{\xi}_3 \\ \dot{\xi}_5 \end{pmatrix} = \begin{pmatrix} -[m_{ij}]^{-1} \cdot [b_{ij}] & -[m_{ij}]^{-1} \cdot [c_{ij}] \\ 1 & 0 & 0 & 0 \\ 0 & 1 & 0 & 0 \end{pmatrix} \begin{pmatrix} \dot{\xi}_3 \\ \dot{\xi}_5 \\ \xi_3 \\ \xi_5 \end{pmatrix} + \begin{pmatrix} [m_{ij}]^{-1} \cdot \begin{pmatrix} L_{\delta 3Fore} & L_{\delta 3Aft} \\ L_{\delta 5Fore} & L_{\delta 5Aft} \end{pmatrix} \\ 0 & 0 \\ 0 & 0 \end{pmatrix} \begin{pmatrix} \delta_{Fore} \\ \delta_{Aft} \end{pmatrix} \\ + \begin{pmatrix} [m_{ij}]^{-1} \cdot \begin{pmatrix} F_{3m} + F_{3W} \\ F_{5m} + F_{5W} \end{pmatrix} \\ 0 \\ 0 \end{pmatrix}$$

We can then define, as before:

$$(2.71) \quad A = \begin{pmatrix} -[m_{ij}]^{-1} \cdot [b_{ij}] & -[m_{ij}]^{-1} \cdot [c_{ij}] \\ 1 & 0 & 0 & 0 \\ 0 & 1 & 0 & 0 \end{pmatrix}, \quad B = \begin{pmatrix} [m_{ij}]^{-1} \cdot \begin{pmatrix} L_{\delta 3Fore} & L_{\delta 3Aft} \\ L_{\delta 5Fore} & L_{\delta 5Aft} \end{pmatrix} \\ 0 & 0 \\ 0 & 0 \end{pmatrix}$$

$$\text{and } D = \begin{pmatrix} [m_{ij}]^{-1} \cdot \begin{pmatrix} F_{3m} + F_{3w} \\ F_{5m} + F_{5w} \end{pmatrix} \\ 0 \\ 0 \end{pmatrix}$$

and hence equation (2.70) assumes a state-space form (2.65).

2.2.b LQR control law in two degrees of freedom

The general two degree of freedom model derived in (2.70) is used. The state vector in heave and pitch modes is defined as follows:

$$(2.72) \quad x(t) = \begin{pmatrix} \dot{\zeta}_3(t) \\ \dot{\zeta}_5(t) \\ \zeta_3(t) \\ \zeta_5(t) \end{pmatrix}$$

In this case, the feedback control law is:

$$(2.73) \quad u = -K \cdot x, \text{ or}$$

$$\begin{pmatrix} \delta_{Fore} \\ \delta_{Aft} \end{pmatrix} = - \begin{pmatrix} K_{11} & K_{12} & K_{13} & K_{14} \\ K_{21} & K_{22} & K_{23} & K_{24} \end{pmatrix} \cdot \begin{pmatrix} \dot{\zeta}_3 \\ \dot{\zeta}_5 \\ \zeta_3 \\ \zeta_5 \end{pmatrix}$$

Hence, the applied flap angle at each timestep is dictated by the current state of heave and pitch motion of the vessel through the gain matrix K, as we can see in the sketch of Figure 55. The gain matrix K is calculated using the LQR solution through the algebraic Riccati equation.

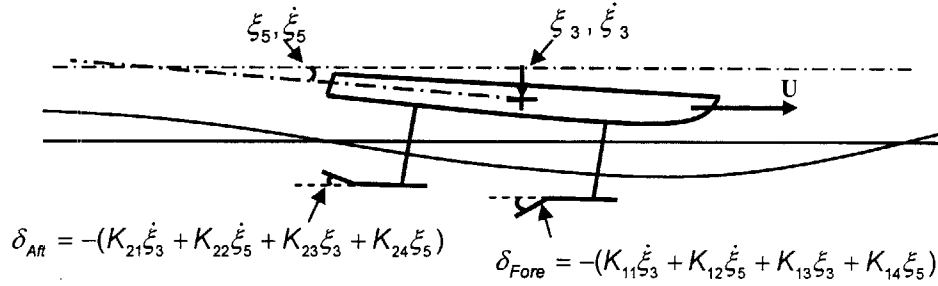


Figure 55: Flap angles determined by state feedback control law

2.2.c Control System Architecture

We briefly describe here the general computational architecture of the combined vessel-controller system. A sketch can be seen in Figure 56. We must note here that the force analysis into wave induced, memory motion induced and flap control force is for descriptive reasons. In reality, the flow solver calculates the total exciting force on the foils through the solution of the Boundary Value Problem as described in the first part of this work.

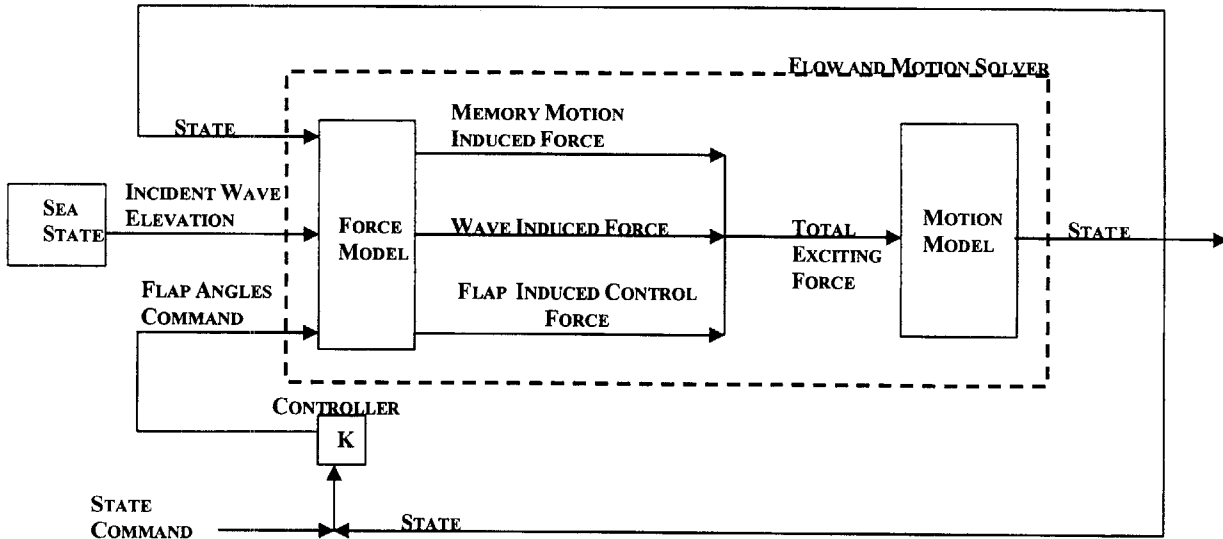


Figure 56: Control system architecture

2.2.d Physical Significance of the Q and R Cost Matrices

It is worth it if we pause to discuss the physical significance of the Q and R cost matrices that appear in the quadratic cost functional of (2.32), for the specific case of a hydrofoil vessel in heave and pitch motion. If we denote as $Q = \text{diag}(q_i)$, $i=1, \dots, 4$ and $R = \text{diag}(r_j)$, $j=1, 2$, then the state and control terms in the cost functional become

$$(2.74) \quad \begin{aligned} X^T Q X &= q_1 \xi_3^2 + q_2 \xi_5^2 + q_3 \xi_3^2 + q_4 \xi_5^2 \\ u^T R u &= r_1 \delta_{FORE}^2 + r_2 \delta_{AFT}^2 \end{aligned}$$

The state weight Q in this case has the physical meaning of penalizing displacement from the zero-state position, which essentially means penalizing non-zero values of heave and pitch displacement and velocity. Roughly speaking, in order to achieve smaller vessel motions one needs to increase the magnitude of the elements of the Q weight matrix. In an analogous manner the control weight R penalizes the use of control – in this case, the use of flap angle. If we assume that control energy expenditure does not concern us in this application (hydrofoil ship), the basic role of the control weight R is to ensure that ‘realistic’ flap angles are used, i.e. not more than the maximum allowable value of 15 degrees.

In one of the following sets of experiments the cost matrices Q and R will be the basic means of adjusting the controller gains and hence the vessel’s behavior. They are initially selected using Bryson’s rule (see section 2.1), and subsequently the state cost Q will be varied in order to achieve the desired result.

2.2.e General Vessel Model

The general model used for both sets of experiments (with and without restoring) is described here. The ship modeled is USS TAURUS (Pegasus class) that served in the US Navy during the 1980s. Information on the actual vessel was derived from the publicly available commissioning brochure of USS TAURUS. An illustration of the vessel in foilborne mode can be seen in Figure 57. The vessel’s principal particulars can be seen in Table 5. The model created is subsequently used in numerical experiments for motion control in coupled heave and pitch motion.

The ship is dynamically supported by two sets of foils that span outside the ship’s beam. The foils can be retracted when the ship is in hull borne mode. The ship is stated to be capable of sustaining speeds in excess of 40 knots in 8-13 ft seas.

USS TAURUS Principal Particulars

L_{OA} (m)	40.00
Beam (m)	8.60
Draft (foils retracted) (m)	1.90
Draft (foils extended) (m)	7.10
Draft (foilborne) (m)	1.00 – 3.00
Displacement (metric tons)	241.00

Table 5



Figure 57: USS Taurus

The geometric and operational information available was used in creating the two-dimensional computational model. The main characteristics of the model can be seen in Table 6. A sketch of the model geometry can be seen in Figure 58.

The lift force generated by the foils is assumed to be equally divided between the fore and aft wings. This is probably not true in reality, since the forward foil appears to have a smaller span than the aft one. However, this assumption was made for simplicity's sake and in lack of more detailed information.

The two foils have identical geometrical characteristics. Chord was initially selected at 2.00m, and foil span assumed to be 8.00m. Subsequently an asymmetrical Karman-Trefftz section was designed that would provide the required lift force per unit span at zero angle of attack. This way, the model roughly represents a vessel that flies in calm water with a steady-state flap angle of zero.

Control is effected via trailing edge flaps which 20% of the chord in length, on both foils. In order to avoid unrealistically large flap angles, the maximum flap angle is set to 15.0 degrees.

**USS TAURUS Model Geometry
(Identical Forward and Aft Hydrofoils)**

Foil longitudinal separation (m)	24.00
Mean Foil Span (used to calculate weight force per m span for 2D model)	8.00
Chord (m)	2.00
Draft (m)	2.50
Mass (metric tons per m span)	30.00

2.2. MOTION CONTROL OF HYDROFOIL CRAFT

VCG (m above foilborne waterline)	6.00
LCG (m from midship)	0.00
Pitch Gyradius (m)	10.00
Foil steady state angle of attack	0.00°
C_L Lift coefficient at steady state	0.33
Trailing Edge Flap Length (% chord)	20.00
Maximum flap angle (deg)	15.00
Foil Section	Karman-Trefftz asymmetrical section $X_c = -0.04, Y_c = 0.05, \tau = 15^\circ$

Table 6

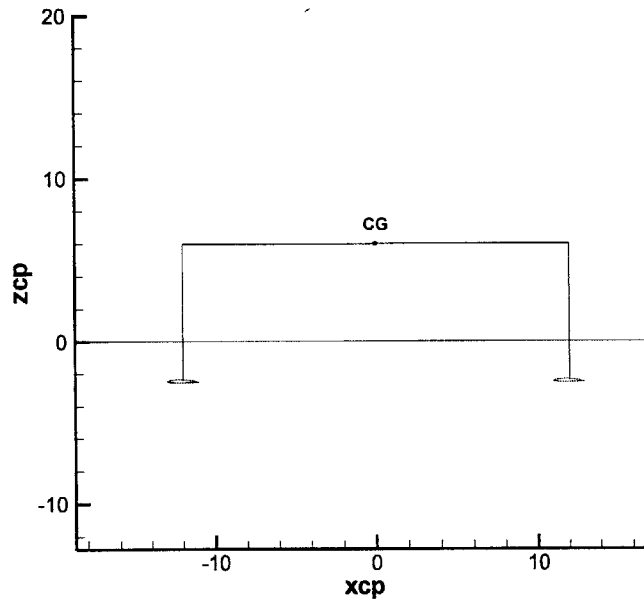


Figure 58: Model geometry based on USS Taurus

2.2.f Motion Control of a Hydrofoil Vessel with Hydrostatic Restoring

In this set of experiments the vessel is assumed to be under the influence of a large hydrostatic restoring force. This vessel is stable without requiring active motion control, as shown in the following experiments. This condition could be a model of the hydrofoil vessel during take-off with its hull still immersed, or a displacement hull aided by hydrofoils (a foil-catamaran for example). The restoring effect for pitch and heave is simulated through the hydrostatic coefficients C_{33} and C_{55} based on the waterplane area and moment of inertia. These coefficients were estimated in the present case from the waterplane properties of USS TAURUS.

The objective here is to demonstrate that the LQR controller can improve the seakeeping performance of an already stable vessel in the coupled heave and pitch mode. This is effected through numerical experiments in incident waves both monochromatic and random. In all experiments the simulations are initially carried with the vessel uncontrolled, subsequently they are re-run with active motion control and comparisons are made.

Sinusoidal Incident Wave

In this set of experiments a monochromatic plane progressive wave of amplitude 1.0 m is incident on the vessel. The vessel’s response to a sinusoidal disturbance is compared for the uncontrolled and the controlled case, for a range of incident wave periods.

The root mean square (RMS) values of the heave displacement and acceleration in the two simulations are used as a means of assessing the controller’s performance. These values are plotted on Figure 59 and Figure 60 respectively. It is apparent that the use of active control reduces both the heave displacement and acceleration for the whole range of periods, making for a smoother ride.

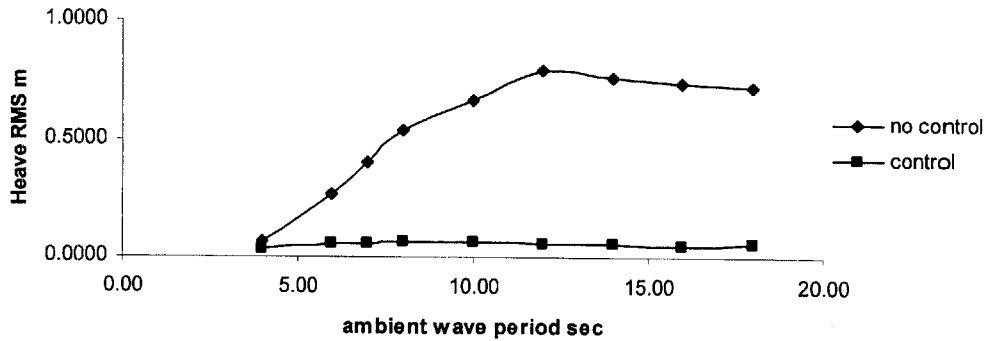


Figure 59: Heave RMS for controlled and uncontrolled ride in plane progressive wave

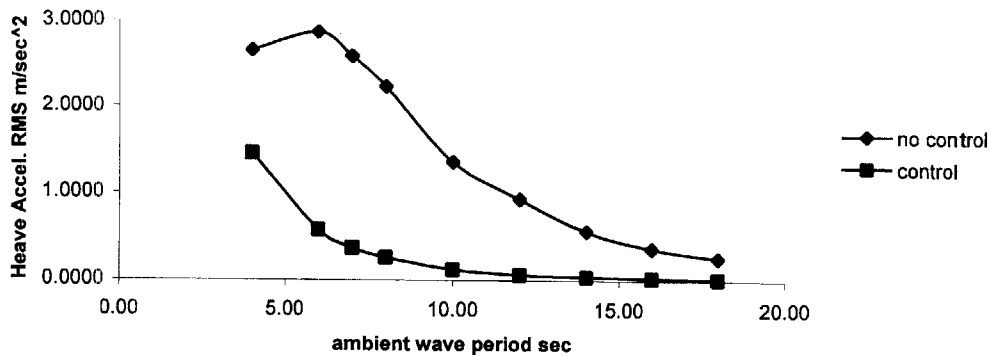


Figure 60: Heave acceleration RMS for controlled and uncontrolled ride in plane progressive wave

Random Incident Wave

A simulated random ocean wave is incident upon the vessel in these experiments. The incident wave is created based on a Pierson-Moskowitz power spectrum of two significant wave heights, 3.0m and 5.0m. The vessel is sailing in the same conditions as in the previous monochromatic wave experiments. The incident wave is simulated by the superposition of 100 sinusoidal components with amplitudes defined by the spectral density as a function of frequency, and random phase following a uniform distribution from 0 to π . Apart from comparing the controller's performance versus the case of an uncontrolled ship, the purpose of these experiments is to show that this deterministic controller can successfully handle the vessel under the effect of random disturbances.

In Figure 61 and Figure 62 we can see a comparison of the heave displacement history for significant wave heights of 3.00m and 5.00m. The controller appears to have a motion reducing effect in both cases. This is also apparent from the RMS values of heave displacement and acceleration on the following table. The heave displacement RMS is greatly reduced to about one fifth or less of its uncontrolled value, while the acceleration RMS is reduced to about 80% of its uncontrolled value.

	control		no control	
	heave rms (m)	heave acceleration rms (m/sec ²)	heave rms (m)	heave acceleration rms (m/sec ²)
H=3.00m	6.43E-02	1.54E+00	3.66E-01	1.78E+00
H=5.00m	1.26E-01	1.78E+00	7.83E-01	2.30E+00

Table 7

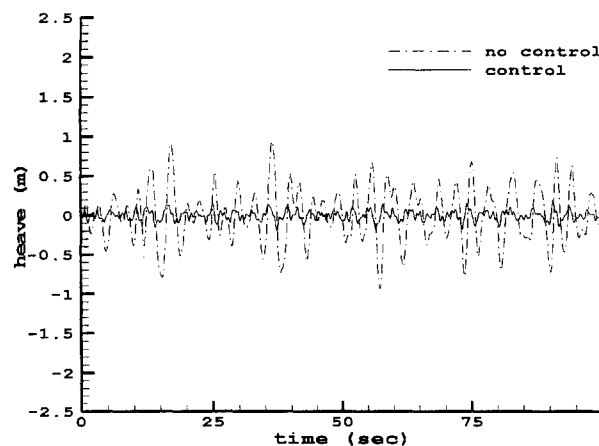


Figure 61: Heave displacement time history comparison for $H_{1/3} = 3.00\text{m}$ ocean wave

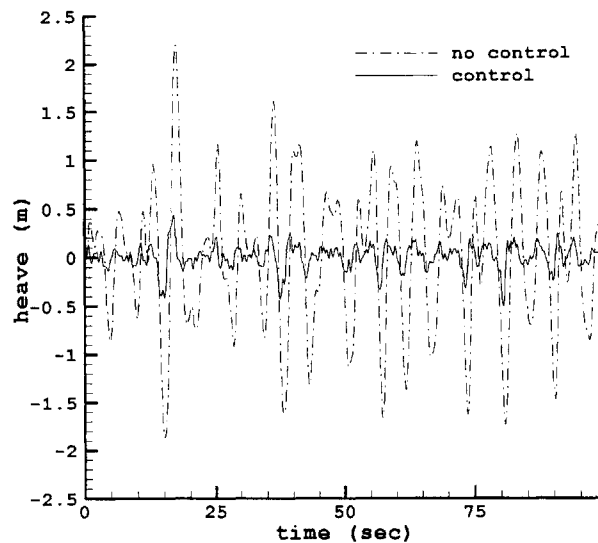


Figure 62: Heave displacement time history comparison for $H_{1/3} = 5.00\text{m}$ ocean wave

2.2.g Motion Control of a Hydrofoil Vessel without Hydrostatic Restoring

In this set of experiments the vessel model possesses no hydrostatic restoring. The only restoring force comes from the dynamic c_{35} coefficient as discussed in the second part of this work. Hence the model attempts to emulate a realistic hydrofoil vessel in fully foil borne condition, with no waterplane area protruding through the free surface (the usually negligible area of foil-supporting struts or propeller shafts is not taken in account). This vessel is potentially unstable in coupled heave and pitch modes hence the ability of the controller to provide a stable ride as well as minimize vessel response to incident waves is examined.

Initially, the use of integral feedback in order to minimize steady-state error in the vessel attitude is investigated and the state-space model is re-designed in order to be used with an augmented state vector including integral terms. This way steady state error in the ship attitude is minimized - this technique which can potentially be used in order to have the vessel follow any commended flight attitude. Subsequently the state cost matrix, whose physical significance was discussed earlier, is used in numerical experiments as a tuning parameter in order to minimize motions in incident waves.

Steady-state Error and Integral Feedback

As stated before, the vessel model is designed so that it will fly at a draft of 2.5 m in calm water without any flap angle applied, i.e. with the steady lift force and foil buoyancy exactly balancing the vessel weight. However, it was seen in initial numerical experiments that small errors in the required lift coefficient calculation resulted in slightly more or slightly

2.2. MOTION CONTROL OF HYDROFOIL CRAFT

less lift force than required. The control system as initially designed (described in the previous sections) did not respond satisfactorily and the vessel, without the influence of hydrostatic restoring, flew with a steady state error in attitude (non-zero heave and pitch displacements). This error was augmented when the vessel weight was deliberately changed - the control system did not manage to drive heave and pitch displacements to zero. Since the vessel weight is something that does constantly change in practice (due to fuel consumption, for example), and since the control system is, before all, expected to function effectively in the simple case of calm water flight, integral feedback was used as a solution. The state vector is augmented by including time integrals of the state variables that display a steady state error (see for example Stengel [1]), namely heave and pitch displacements:

$$(2.75) \quad \begin{aligned} \xi_{3I}(t) &= \int_0^t \xi_3(\tau) d\tau \\ \xi_{5I}(t) &= \int_0^t \xi_5(\tau) d\tau \end{aligned}$$

The two extra state equations that result are, obviously,

$$(2.76) \quad \begin{aligned} \dot{\xi}_{3I}(t) &= \xi_3(t) \\ \dot{\xi}_{5I}(t) &= \xi_5(t) \end{aligned}$$

and the complete state equation is given by the combination of equations (2.70) and (2.76):

$$(2.77) \quad \begin{pmatrix} \dot{\xi}_3 \\ \dot{\xi}_5 \\ \dot{\xi}_3 \\ \dot{\xi}_5 \\ \dot{\xi}_{3I} \\ \dot{\xi}_{5I} \end{pmatrix} = \begin{pmatrix} [m_{ij}]^{-1} \cdot [b_{ij}] & [m_{ij}]^{-1} \cdot [c_{ij}] \\ 1 & 0 & 0 & 0 \\ 0 & 1 & 0 & 0 \\ 0 & 0 & 1 & 0 \\ 0 & 0 & 0 & 1 \end{pmatrix} \cdot \begin{pmatrix} \xi_3 \\ \xi_5 \\ \xi_3 \\ \xi_5 \\ \xi_{3I} \\ \xi_{5I} \end{pmatrix} + \begin{pmatrix} [m_{ij}]^{-1} \cdot \begin{pmatrix} L_{\delta 3Fore} & L_{\delta 3Aft} \\ L_{\delta 5Fore} & L_{\delta 5Aft} \end{pmatrix} \\ 0 & 0 \\ 0 & 0 \\ 0 & 0 \\ 0 & 0 \end{pmatrix} \cdot \begin{pmatrix} \delta_{Fore} \\ \delta_{Aft} \end{pmatrix} \\ + \begin{pmatrix} [m_{ij}]^{-1} \cdot \begin{pmatrix} F_{3m} + F_{3w} \\ F_{5m} + F_{5w} \end{pmatrix} \\ 0 \\ 0 \\ 0 \\ 0 \end{pmatrix}$$

Integral feedback eliminates steady state error. In order to demonstrate its effectiveness, a large weight increase is input (from a nominal weight of 30 tons/m span the weight was increased to 40 tons/m span). The original control system let the vessel ‘fly’ with a constant non-zero heave displacement of 0.30 m. The modified control system with integral feedback completely eliminated this steady-state error, as can be seen in Figure 63. Integral feedback could also be used in order to have the vessel follow a non-zero commanded flight level.

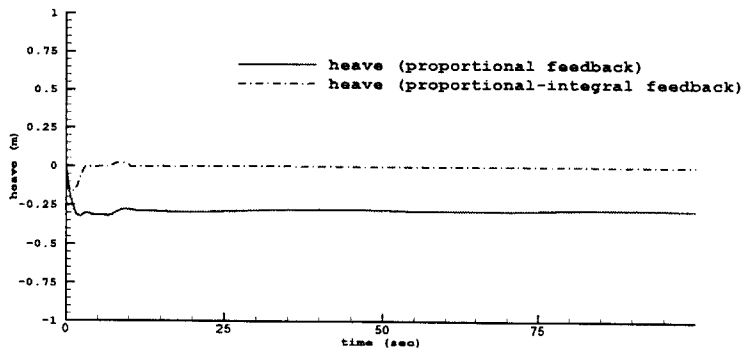


Figure 63: Elimination of heave steady-state error by integral feedback

Sinusoidal Incident wave

In this set of numerical experiments the vessel is advancing in an ambient monochromatic plane progressive wave. The ability of the LQ regulator to control the vessel’s motion in heave and pitch is examined, and its performance is tuned through the state cost Q. The parameters can be seen on Table 8.

Vessel speed	20 m /sec
Incident wave	Sinusoidal, direction 180 degrees (head seas)
Incident wave amplitude	2.0 m
Incident wave absolute period	8 sec

Table 8

The heave displacement cost weight q_3 is used as the varying parameter, in an attempt to minimize heave motion. The Q and R matrices are initially selected using Bryson’s rule. Hence we initially assumed the following ‘maximum allowable’ values for each element of the state and control vector:

2.2. MOTION CONTROL OF HYDROFOIL CRAFT

$$(2.78) \quad x_{MAX} = \begin{pmatrix} \dot{\xi}_{3 MAX} = 1.0 \text{ m/sec} \\ \dot{\xi}_{5 MAX} = 10.0 \text{ deg/sec} \\ \xi_{3 MAX} = 1.0 \text{ m} \\ \xi_{5 MAX} = 3.5 \text{ deg} \\ \xi_{31 MAX} = 1.0 \text{ m sec} \\ \xi_{51 MAX} = 10.0 \text{ deg sec} \end{pmatrix}, \text{ and } u_{MAX} = \begin{pmatrix} \delta_{FORE MAX} = 9.50 \text{ deg} \\ \delta_{AFT MAX} = 9.50 \text{ deg} \end{pmatrix}$$

From Bryson’s rule we calculate the initial Q and R matrices. The cost matrices together with the resulting LQR gains can be seen on Table 9.

Q_cost =	R_cost =	K_gain =
1 0 0 0 0 0	35 0	0.0973 0.6641 0.2898 3.3160 0.1435 0.5129
0 33 0 0 0 0	0 35	0.0702 -0.4429 0.1780 -2.2170 0.0893 -0.8245
0 0 1 0 0 0		
0 0 0 300 0 0		
0 0 0 0 1 0		
0 0 0 0 0 33		

Table 9

This controller results in a vessel motion with heave Response Amplitude Operator (RAO) of 0.185.

Subsequently, the heave weight cost element q_3 is increased, in an attempt to decrease the heave motion. Four characteristic cases are displayed in Figure 64, together with the incident wave elevation amidships. With a q_3 of 200.0 the smallest heave RAO of around 0.025 was achieved. Maximum flap angles were in the order of 12-15 degrees (the RMS values of the applied flap angles can be seen in Figure 65). As expected, higher state cost results in greater control usage as can be seen in Figure 65. The varying cost’s effect on the control gains is demonstrated if we look at the gain matrix for $q_3 = 200.0$ on Table 10.

K_gain =
0.2332 0.7449 1.8890 3.7040 0.1319 0.6073
0.1803 -0.3852 1.5140 -1.9480 0.1057 -0.7577

Table 10

Obviously the K_{13} and K_{23} heave state gains are much larger than originally. When q_3 was increased further, the resulting gains were so large that flap angles attempted to exceed 15.0 degrees and the vessel motion became unstable.

It is interesting to note here that although heave acceleration is not directly penalized through this formulation, minimizing heave motion results in lower accelerations as well. This can be seen in Figure 66 where the acceleration RMS is plotted against the q_3 weight.

Random Incident Wave

In this set of experiments a simulated random ocean wave is incident upon the vessel. As in the previous random wave experiment the ocean wave is simulated by the superposition of 100 sinusoidal components with amplitudes defined by the spectral density, and random phase following a uniform distribution from 0 to π . Results for two significant wave height values, 1.00 and 3.00 meters, are presented.

For the larger wave height an increasing state cost results in smaller motion amplitudes as can be seen in the heave RMS plot of Figure 67. This is not the case for the smaller wave height where the state cost appears not to influence the resulting RMS very much. It is evident for both wave heights that a higher heave state penalty results in higher acceleration RMS value (as can be seen in the acceleration RMS plot of Figure 68), the opposite of what happened with an incident monochromatic wave. In this case it appears that the displacement reduction is traded in for an increase in accelerations, at least in the case of the larger wave height. A time history of heave motion for the two wave heights of 1.00 and 3.00 meters, and heave state cost q_3 value of 1.00 can be seen in Figure 69, and for q_3 value of 50.00 in Figure 70.

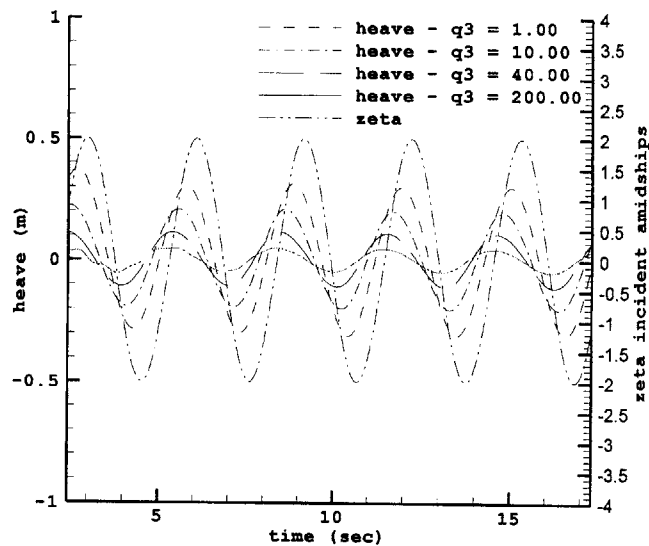


Figure 64: Heave displacement with varying q_3 heave state cost (plane progressive wave)

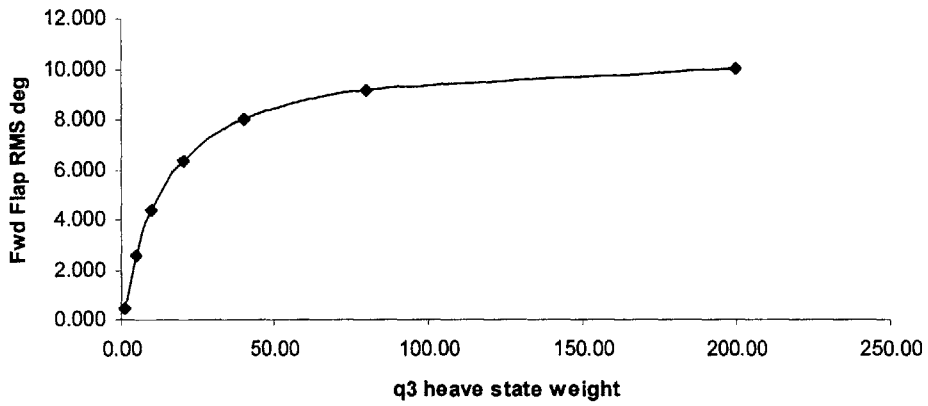


Figure 65: Flap angle RMS with varying q3 heave state cost (plane progressive wave)

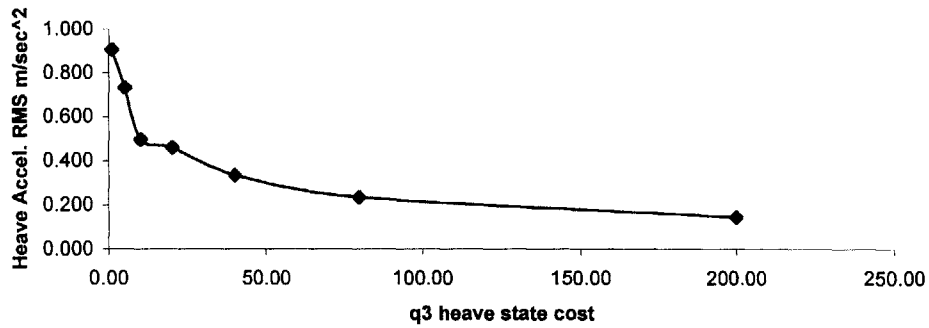


Figure 66: Heave acceleration RMS with varying q3 heave state cost (plane progressive wave)

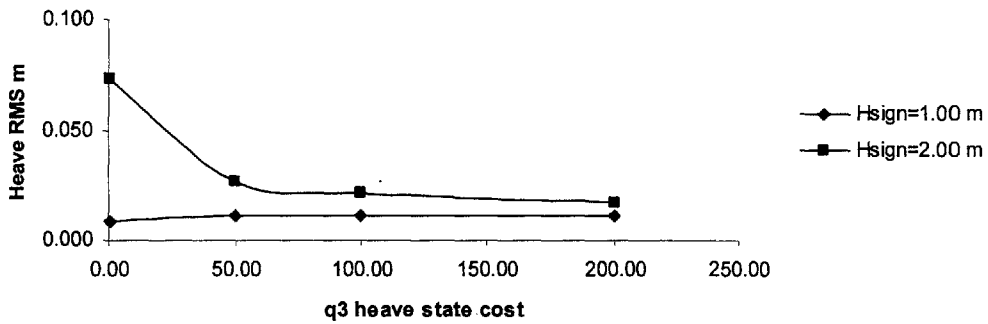


Figure 67: Heave RMS with varying q3 heave state cost (ocean wave)

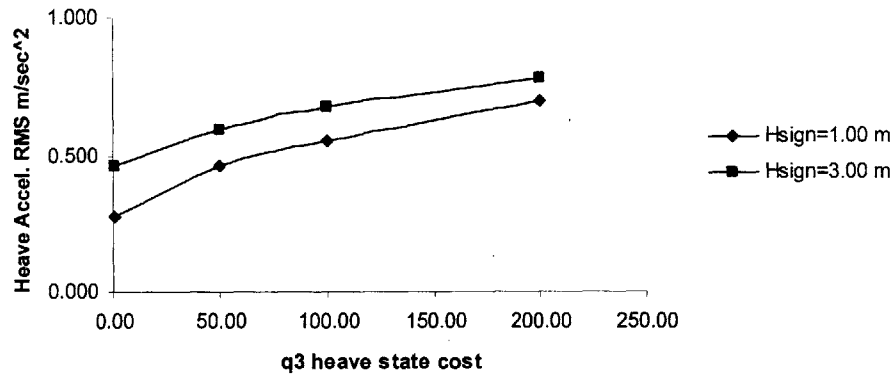


Figure 68: Heave acceleration RMS with varying q3 heave state cost (ocean wave)

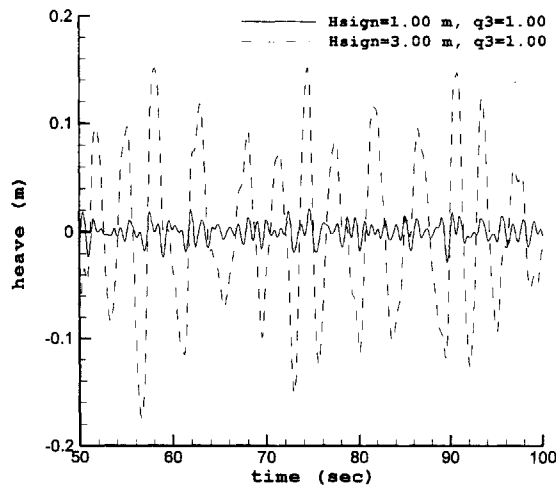


Figure 69: Heave displacement time history for q3 = 1.00 (ocean wave)

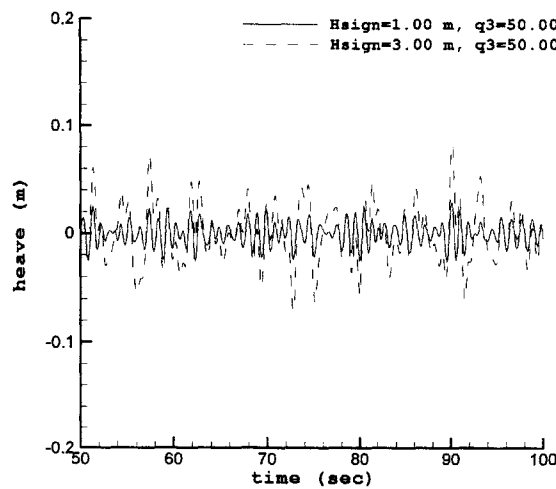


Figure 70: Heave displacement time history for q3 = 50.00 (ocean wave)

Conclusions and future work

The development and validation of the hydrodynamic force and motion solver in the first part has provided a simulation tool with sufficient accuracy for the study of motion control methods, which follow in the second part. The main point is that a deterministic optimal control law designed with state-space methods around the zero-mean trajectory of a hydrofoil craft can potentially reduce vessel motions in a sea state. Design of the control law has been effected through the seakeeping equations of motion, ignoring hydrodynamic memory effects. Initial results from numerical experiments in sinusoidal and simulated ocean waves are encouraging.

This thesis opens a number of new subjects for possible future work. The numerical hydrodynamic solver could accept a number of improvements while still remaining simple and fast – examples are a more accurate wake treatment and wake-foil interaction for multiple foil ships. On the other hand a lot of work remains to be done in motion control. This thesis proposed the use of the deterministic Linear-Quadratic Regulator for the control of hydrofoil craft sailing in ambient waves, with encouraging initial results. More experiments covering a large number of possible geometries and flow conditions are needed in order to study the merits and shortcomings of such a control system. The motion of hydrofoil craft also remains to be studied as a stochastic optimal control problem, which it essentially is. It is the author's opinion that this problem could also be well-suited to the application of robust design methods such as H-infinity since from one side, there is often a large amount of uncertainty about the amplitude of external disturbances (incident ocean waves), and from the other side, the available information on the vessel dynamics is not always sufficiently accurate for the design of state-space models. Finally, a means of including hydrodynamic memory effects into a linear state-space model of hydrofoil vessels would provide a more accurate way of designing control laws. This could be accomplished with an autoregressive-type model, using the time history of the vessel's motion.

Bibliography

- 1 J N Newman, 'Marine Hydrodynamics', MIT Press, 1977
- 2 D Kring, 'Time Domain Ship Motions by a Three-Dimensional Rankine Panel Method, PhD thesis, MIT 1994
- 3 Wehausen & Laitone, 'Encyclopedia of Physics: Surface Waves', Online edition 2002
- 4 P D Sclavounos, '13.022 Surface Waves and their Interaction with Floating Bodies', MIT Lecture Notes, Fall 2002
- 5 G Tozzi, MIT Master of Science Thesis, to be submitted
- 6 D E Nakos, 'Ship Wave Patterns and Motion by a Three Dimensional Rankine Panel Method', PhD thesis, MIT 1990
- 7 B L Stevens, F L Lewis, 'Aircraft Control and Simulation', Wiley & Sons 1992
- 8 J J D'Azzo, C H Houpis, 'Linear Control System Analysis and Design – Conventional and Modern', McGraw-Hill 1995
- 9 F L Lewis, 'Applied Optimal Control and Estimation', Prentice Hall 1992
- 10 A Bukley, C D Johnson, M Balas, 'Complexity Mitigation by Active Control applied to Linear Dynamic Systems', IFAC 2001 Automatic Control in Aerospace proceedings
- 11 H Tokutake, 'Robust Flight Control with Eigenstructure Assignment', IFAC 2001 Automatic Control in Aerospace proceedings
- 12 R Adams, J Buffington, A Sparks, S Banda, 'Robust Multivariable Flight Control', Springer-Verlag 1994
- 13 F Amato, R Iervolino, 'Robust Control Law Design for a Small Commercial Aircraft', IFAC 2001 Automatic Control in Aerospace proceedings
- 14 G Zames, 'Feedback and Optimal Sensitivity: model reference transformations, multiplicative semi norms, and approximate inverses', IEEE Trans. Aut. Control, vol. 26 (1981)
- 15 J Doyle, K Glover, P Khargonekar, B Francis, 'State Space Solutions to Standard H_2 and H_∞ Control Problems', IEEE Trans. Aut. Control, vol. 34 (1989)
- 16 K P Rhee and S Y Lee, 'On the robust design of a Motion Regulator for Foil-Catamaran in Irregular Waves',
- 17 F. Kenevissi et al, 'A New-Generation Motion-Control System for Twin-Hull Vessels Using a Neural Optimal Controller', Marine Technology and SNAME News, July 2003
- 18 M Rostgaard et al, 'Stochastic Modeling and Adaptive LQG control of a Ship', 12th IFAC 1993
- 19 Thor Fossen, O E Fjellstad, 'Cascaded Adaptive Control of Marine Vehicles with Significant Actuator Dynamics', 12th IFAC 1993

BIBLIOGRAPHY

- 20 X Jia et al, 'Ship Motion Control Using Multiple Algorithms', 12th IFAC 1993
- 21 I S Akkizidis et al, 'Steering and Depth Control of an Underwater Robot using Fuzzy-Like PD Controller', IFAC 2000
- 22 Thor Fossen, 'A Survey of Nonlinear Ship Control: From Theory to Practice', IFAC 2000 on Maneuvering and Control of Marine Craft
- 23 Pierre Belanger, 'Control Engineering: A Modern Approach', Saunders 1995
- 24 B D O Anderson, J B Moore, 'Optimal Control: Linear Quadratic Methods'. Prentice Hall 1990
- 25 D Luenberger, 'Introduction to Dynamic Systems: Theory, Models and Applications', Wiley 1979
- 26 D Bertsekas, 'Dynamic Programming and Optimal Control', Athena Scientific 2000
- 27 R E Stengel, 'Optimal Control and Estimation', Dover 1994
- 28 H Akaike and T Nakagawa, 'Statistical Analysis and Control of Dynamic Systems', KTK Scientific Publishers 1972
- 29 K Ohtsu, 'The Statistical Optimum Control of Ship Motion and a Marine Main Engine'
- 30 F Ogilvie, 'Recent progress in the understanding and prediction of ship motions', 1964
- 31 O M Faltinsen, 'Sea Loads on Ships and Offshore Structures', Cambridge Univ. Press 1990
- 32 P. D. Sclavounos, S Purvin, T Ulusoy, S Kim, 'Simulation Based Resistance And Seakeeping Performance Of High-Speed Monohull And Multihull Vessels Equipped With Motion Control Lifting Appendages', FAST 2003 proceedings.